Evaluation of Mechanical Properties in Pipeline Girth Welds Using Instrumented Indentation

by

Abdelbaset Midawi

A thesis
presented to the University of Waterloo
in fulfilment of the
thesis requirement for the degree of
Doctor of Philosophy
in
Mechanical and Mechatronics Engineering

Waterloo, Ontario, Canada, 2018

© Abdelbaset Midawi 2018

Examination Committee Membership

The following served on the Examining Committee for this thesis. The decision of the Examining Committee is by majority vote.

External Examiner	Professor. Leijun Li
	Department of Chemical & Materials Engineering University of Alberta
Supervisor	Professor. Adrian P. Gerlich
	Department of Mechanical & Mechatronic Engineering University of Waterloo
Internal Member	Professor. Norman Y. Zhou
	Department of Mechanical & Mechatronic Engineering University of Waterloo
Internal Member	Professor. Duane Cronin
	Department of Mechanical & Mechatronic Engineering University of Waterloo
Internal-external Member	Professor. Scott Walbridge
	Department of Civil and Environmental Engineering University of Waterloo

This thesis consists of material all of which I authored or co-authored: see Statement of Contributions included in the thesis. This is a true copy of the thesis, including any required final revisions, as accepted by my examiners.

I understand that my thesis may be made electronically available to the public.

Statement of Contributions

This thesis includes Nine chapters. Each chapter starting from chapter 4 up to 8 represents a publications I authored or co-authored, it should be noted that the main work in the lab including sample preparation, welding of the samples, mechanical testing, writing, and characterization was done by my own. The following co-authors have contributed to the current work as outlined below:

Professor Adrian Gerlich supervised this PhD thesis.

Dr. C.H. Simha acted as my co-supervisor at Canmet Materials and he set the inverse approach procedure and help me to analysis the finite element model results and he also assisted the authors with editing chapter five and chapter six.

Mr. M. Gesing helped me to build the finite element model for the indentation process.

Mr. Y. Kisaka and Mr. E.B.F. Santos help me to prepare the welded samples and perform the welding process and collect the welding data. They also assisted with editing chapter four.

The balance of this work is my own.

Abstract

This study aims to develop a new method to characterize mechanical properties using instrumented indentation. The indentation results were correlated with observed microstructure in weld metal of gas metal arc welding (GMAW) pipeline joints with their mechanical properties such as: hardness and yield strength. The focus of this work was on a representative API-X80 grade weldment using different commercial welding consumables. Microstructure analysis was conducted on the as-deposited and reheated regions of the weld in each pass. The microhardness distribution was mapped for the whole weld cross section and correlated with the observed microstructure. A nearly flat tip indenter was used to measure the load versus displacement response during micro-scale instrumented indentation test, in order to determine the yield strength for different areas in the weld region. This technique had previously been used as provided by the inventor to determine the apparent yield strength for a wide range of engineering materials. However, the detailed physics of the method were not described. In the second phase of this work, a finite element model was built to understand the mechanics of contact using this indenter geometry and to derive the full stress-strain relationship from the indentation test data (based on load-displacement response) using an inverse approach, and to correlate these to the experimentally measured yield strength for pipeline steels. To establish the inverse approach, the model was tested in the first stage for common materials such as steel and aluminium alloys. This inverse approach technique aims to determine the tensile properties by analyzing the full load-displacement curves. In addition, by further analysis of the FE modelling results, a new technique to determine yield strength based on the load-displacement curve

and indenter geometry was developed and validated with the experimental results. This technique, utilizing the nearly-flat indenter geometry along with cavity expansion theory and/or slipline theory, allows one to determine yield strength directly from an experimental load-displacement curve. The advantage of using this technique is that there is no need to use regression fitting or other assumptions of the material properties to estimate yield strength, or require FE modelling. Different steel and aluminium alloys were tested and the results correlated well with the yield strength measured by conventional tensile testing. Validating this indentation method as a localized strength measurement technique is essential, so that it can be used to conveniently test different regions of a weld joint. Once the method was validated, the yield strength was measured for different API-X80 pipeline steel welds using the nearly flat tip indenter. The indentation based measurements of the apparent yield strength were correlated with the microstructure and hardness values in each zone. Moreover, the indentation technique was able to characterize narrow zones in the weld and heat effected zone (HAZ) such as reheated weld metal, deposited weld metal, coarse grain heat effected zone (CGHAZ), and fine grain heat effected zone (FGHAZ).

Digital Image Correlation (DIC) was also used to map the strain distribution during transverse tensile testing for the welds. DIC data provided further evidence of the strain distribution post-yielding, along with more information regarding the effect of strength mismatch level on strain distribution through the welding joint. The result of the strain map also was correlated with the formed microstructure in the WM and HAZ. The DIC data were used to construct local stress-strain curves based on the iso-stress condition assumption. The tensile yield strength results were compared with the indentation yield strength in different zones through and across the weld zone and the results showed good

agreement between them and suggest that the nearly flat tip indentation technique could be used as a tool to determine the level of strength mismatch between a weld metal and base metal. In addition, the convenience of the indentation technique allows one to determine strength mismatch in both the longitudinal and transverse directions revealing that the estimation of the strength mismatch using the all-weld metal could overestimate the strength mismatch level up to 10%, which may lead to non-conservative design.

Finally, further study of the mechanical properties of the weld metal in the longitudinal and transverse directions indicated that the weld metal has anisotropic properties. The indentation results were compared with conventional tensile test results for all-weld metal and cross-weld specimens; results from the latter specimens also supports anisotropy of strength in the weld. These results were also supported by hardness mapping and detailed microstructral cheracterztion of the weld metal. This understanding is essential to improve the integrity and reliability of welds and testing procedures for pipeline applications.

Acknowledgements

In the name of Allah the beneficent the merciful. I wish to express my profound gratitude to Allah for his grace and mercy granted to me right from birth to date, "Thanks my God".

My profound gratitude goes to my country Libya for the support and grand even during the most difficult situations and unstable conditions.

I wish to render my unreserved gratitude to my project supervisor Prof. Adrian Gerlich for his support and guidance and time given to me during this work. You gave me all the support and freedom I would ever need to conduct experiments and do an original research toward this PhD thesis. I will never forget it, thank you and God bless you. I would also like to show my appreciation to Canmet Materials staff especially Dr. Hari Sihma for his continuous support and guidance to perform the simulation process and analyze the results. I would like also to show my appreciation to our technical staffs that have helped me through the practical work, especially Mr Mark Griffet.

My heartfelt gratitude goes to the TransCanada Pipeline and NSERC for their support and fund of this project. I wish to acknowledge the support and encouragement of my colleagues and friends at CAMJ group, especially Emanuel Santos, Nazmul Huda, Yuji Kisika, Lugman Shah, and Rafael Ribeiro. Thank you for your continuous support and valuable discussion and contribution to this work.

Abdelbaset R. H. Midawi *Waterloo, ON, Canada, 2018*

Dedication

This is dedicated to the one I love. My heartfelt gratitude goes to my Father Ramadan Midawi and to the spirit of my mom Fatma Aaron, and my wife's Areij Mohamed for their support both morally and spiritually, and for their patience and love. I also would like to dedicate it to my brothers Dr. Taher and Mr. Hamad Midawi for their support and encouragement.

Table of Contents

List of Tables

List of Figures

"Education is our passport to the future, for tomorrow belongs to the people who prepare for it today".

Malcolm X.

Chapter 1

Introduction

1.1 Background

Global oil and gas consumption has increased over the last few decades and is expected to continue to increase. According to the report from International Energy Organization World Energy Consumption Outlook report 2016, the demand for energy sources will grow by 56 percent between 2010 and 2040. Total world energy use will increase from 524 quadrillion British thermal units (Btu) in 2010 to 630 quadrillion Btu in 2020 and to 820 quadrillion Btu by 2040 as shown in Figure 1.1. Most growth occurs in countries outside the Organization for Economic Cooperation and Development (Non-OECD). This demand encourages the oil and natural gas companies nowadays to make the transportation of oil and gas from the point of origin across countries more efficient and economical, which drives them to use new grades of high-pressure long distance pipelines [146].

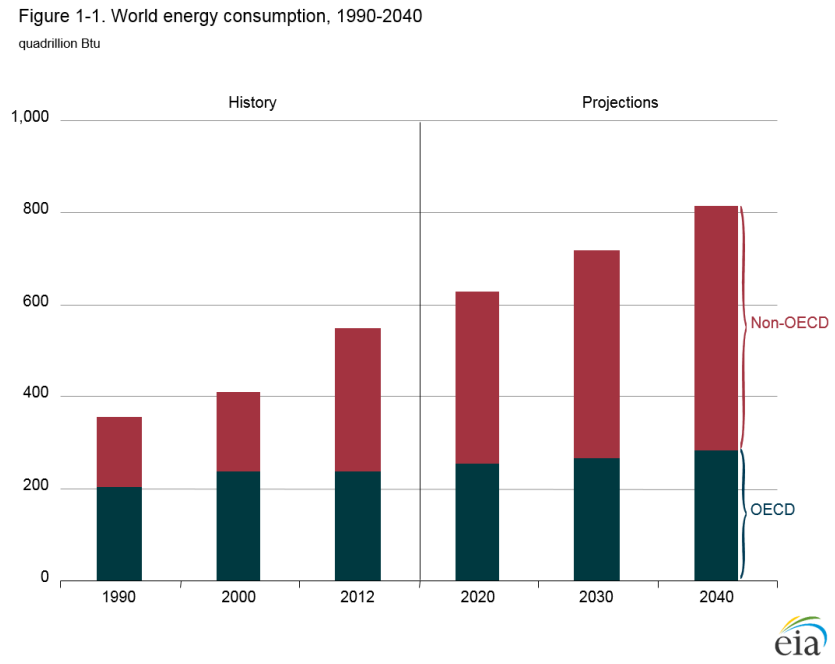

Figure 1.1: Expected world energy consumption, 1990-2040 (Reprinted with permisson) [146].

Many pipeline projects for oil and gas transport have been planned between Canada and United State. As shown in Figure 1.2, this includes TransCanada's proposed Keystone XL pipeline designed to carry oil sands crude south from Alberta to refineries in Texas. Figure 1.2 shows the map for existing pipelines and proposed routes. Most standards and codes for high strength steel that specify design requirements and testing procedures are limited to steels with strength less than 550 MPa. Newer grades such as X100 and X120 are now being produced, but are still experimental and are specified to require unique engineering standards to be met, which go above the existing pipeline standards, such as CSA, DNV, and API standards [6, 39, 74]. Thus, a gap exists between steel makers and construction companies [119]. The main concern for construction companies stems

from the uncertainty in the mechanical properties of the welds. Therefore, there is a need to improve welding processes used for pipeline steels in order to transport oil and gas in efficient and reliable way, especially using newer high-strength steels. Circumferential girth welds are an efficient way to join pipe segments to form a pipeline. However, like other joining techniques, it produces heterogeneous structures in the fusion zone or Weld Metal (WM), and Heat Affected Zone (HAZ), which differ from the base metal structure. The mechanical properties, specifically the hardening behaviour, of the fusion zone and HAZ are differ significantly from those of the parent material. These zones may be particularly different in the latest pipe materials produced by the Thermo-Mechanically Controlled Processing (TMCP) route, which offers a cheaper and more effective means of producing these pipeline steels than traditional hot rolled and normalized steels.

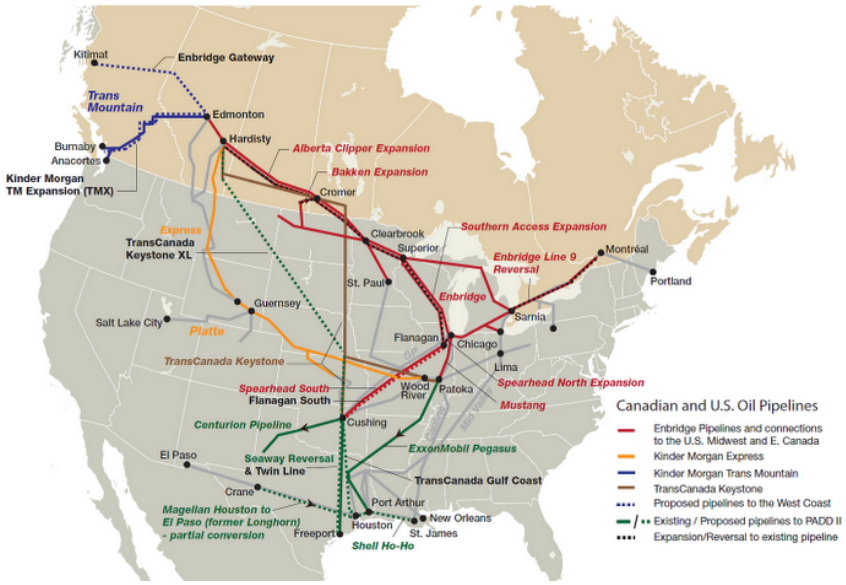

Figure 1.2: Map of existing and proposed pipelines projects to transport oil and gas between Canada and the United States [25].

The need to achieve higher strength accompanied with sufficient toughness and ductility has motivated the improvement of high strength steel properties for harsh environments such as low-temperature, high-pressure, and corrosive service. These newer steel grades afford operation at 20 MPa internal pressure (current pipelines operate at approximately 10 MPa), which can be seen as an advanced variant of High Strength Low Alloy (HSLA) steels, and are designated according to the American Petroleum Institute (API) as X80, X100, and X120, where the number denotes yield strength in ksi. However, using welding processes such as Gas Metal Arc Welding (GMAW) to fill the joint with weld metal for a thick pipe can create heterogeneity in the mechanical properties. This is particularly true when a multipass welding procedure are used to join thick pipe, which exposes weld metal to multiple thermal cycles and changes the microstructure throughout the weld joint. Using variations of the GMAW process, such as single torch, dual torch, or tandem torch will also influence the heterogeneity in the weld metal. Although the GMAW dual torch method can deposit more weld metal in a single pass while reducing overall cost compared to single torch GMAW, the mechanical properties may potentially degrade if the welding parameters are not carefully controlled [122, 158]. Additionally, during the welding process, the microstructure of these steels changes due to the formation of a HAZ. Thermal cycles generally exceed the phase transformation temperatures in the weld metal and HAZ, leading to a significant variation in the mechanical properties. The high temperatures achieved in the HAZ often lead to decreases in fracture toughness, typically due to grain growth as a result of carbide dissolution and formation of a coarse grain structure. In multi-pass welds, an intercritically re-heated coarse grain HAZ is formed. The re-heated zones produce some undesirable islands called martensite austenite (M-A) constituents,

leading to the formation of local brittle zones. The small brittle zones in the weld joint can create a failure initiation point, which may restrict the qualification of a weldment or weld procedure [73, 128]. In order to qualify the mechanical properties of the welded structure, hardness, tensile strength, and toughness are usually measured. However, multi-pass welding of pipeline steel creates heterogeneity in the weld region and leads to variation in the mechanical properties. Owing to the size of the HAZs, conventional techniques of measurement are difficult to use. Therefore, it is essential to establish new methods to identify the mechanical properties for different zones in the weld region. The focus of the this research is to develop methods to test local tensile yield strength heterogeneity through the WM and HAZ of welded pipeline steels. The technique should also be applicable to the base metals. With aging pipelines being modified or expanded, welding on these existing lines is more routine, and non-destructive or superficial testing methods for verifying their properties are becoming more important. Therefore, developing an accurate and non destructive technique to measure mechanical properties could lead to a standard and/or a simple method for field measurements.

1.2 Objectives

This study aims to correlate the observed microstructure in weld metal of GMAW pipeline joints with their mechanical properties such as: hardness and yield strength. The focus will be on a representative API-X80 line pipe grade weldment using commercially available welding consumables. Microstructure analysis will be conducted on the as-deposited and reheated regions of the weld in each pass. The microhardness distribution will be mea-

sured in the deposited passes and reheated zones using a hardness mapping technique and correlated with the observed microstructures. A nearly flat-tip indenter will be used to measure the load versus displacement during a micro-scale indentation test. It is proposed to develop techniques to estimate mechanical properties such as yield strength, stress-strain behaviour of the substrate using the instrumented indentation technique.

1.3 Overwiew of the methods

The load-displacement behavior from instrumented indentation will be used in an inverse framework, wherein finite element computations are used to estimate the stress-strain response of the base metal. The inverse approach will be conducted on base metal samples to establish the procedure and then will be applied on welded pipelines joints. The computations also yield insights into the small-strain response of the substrate, which are then used to develop rapid methods to determine yield strength for all areas of the weldment. Validating this indentation method as a localized strength measurement technique is essential, so that it can be used to conveniently test different regions of a weld joint. Once the method is validated, the yield strength distribution is mapped using this indentation method to assess the strength mismatch across different pipeline welded joints. In addition, Digital Image Correlation (DIC) is used to map the strain distribution during transverse tensile weld testing. DIC could provide further evidence of the strain distribution post-yielding, and provide an indication of the most representative tensile test procedure for describing the level of weld metal strength overmatching achieved using a given weld procedure. The result of the strain map can then be correlated with the formed microstructure.

This understanding is essential to improve the integrity and reliability of welds and testing procedures for pipeline applications.

1.4 Thesis outline

This thesis consists of nine chapters. The first chapter presents the motivation behind this work and state the main objectives of the thesis. In the second chapter general background knowledge about the line pipe steel and the manufacturing process of the line pipe steel. The effect of alloying element and the welding processes are also discussed in this chapter. In addition, welding metallurgy and the microstructure of the weld and heat effected zone is briefly described. Literature review, which includes an overview of characterization methods, such as indentation technique and issues, such as strength overmatching are also discussed. By the end of chapter two specific objectives are stated. In chapter three, the procedure of welding and sample extraction was explained. The mechanical testing procedure, such as tensile testing, DIC setting, and hardness testing was also discussed. Subsequently, the procedure of building the indentation Finite Element Model using ABAQUS software is also described. Chapter four through chapter eight represent the content in published or submitted manuscripts. The main focus of these chapters is to validate the nearly flat tip indentation as a tool to measure the yield strength for engineering materials. In addition, to apply this technique for pipeline application, in order to assess the strength mismatch and evaluate narrow zones such as HAZ and reheated weld metal. Lastly, chapter nine summarizes the main findings of this work and suggest some opportunities for future research.

Chapter 2

Literature Review

2.1 Iron and steel

Steel is an Iron-Carbon alloy that contains up to 2.1wt% carbon (all % values for composition will be in wt% henceforth) and a variety of other alloying elements. Beyond 2.1% carbon content the alloy is considered cast iron, rather than steel. Figure 2.1 shows the main classifaction of steel based on the alloying elements. Different alloying elements are added to steel to enhance various properties, and it can be classified based on these alloying elements, performance, and applications into hundreds of grades [22]. Due to the transformation during welding process or heat tretments the final microstructure of steel depends on many factors including the heating rate, cooling rate, peak temperature, and chemical composition. There are different classification for steels, a simple and popular way to classify steels are based on chemical composition as shown in Figure 2.1. In this

work the focus will be on high strength low alloy steels particularly linepipe steel and it's welds [132].

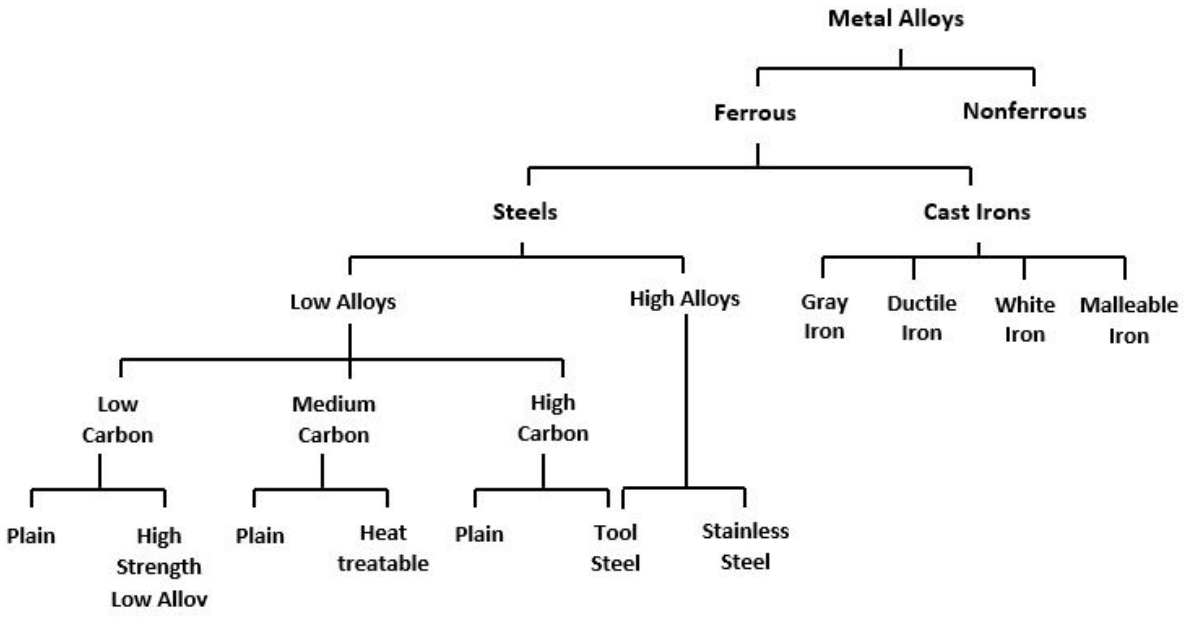

Figure 2.1: Ferrous metals classification [132]

.

2.1.1 High strength low alloy steels (HSLA Steel)

Low alloy steel, as the name indicates, contains small amounts of alloying elements that produce remarkable improvements in the steel properties. Low alloy steel is generally defined as having a 1.5% to 5% total alloy content. Common alloying elements are manganese, silicon, chromium, nickel, molybdenum, and vanadium. Low alloy steels may contain as many as four or five of these elements in varying amounts [38]. High strength low alloy (HSLA) steels or micro-alloyed steel are classified as low alloy steels since the total percentage of

alloying elements is less than 4% [38]. Many grades have been designed to provide specific desirable combinations of properties such as strength, toughness, formability, weldability, and atmospheric corrosion resistance [123]. These properties make HSLA steels desirable for many applications, such as oil and gas pipelines, heavy-duty highway and off-road vehicles, construction and farm machinery, industrial equipment, pressure vessels, bridges, offshore structures, power transmission towers, light poles, as well as building beams and panels.

The base metal microstructure design is a key variable in determining material mechanical properties to ensure safe and optimal performance under the desired operating conditions. This design relies on optimizing the chemical composition in the base metal and welding zone. HSLA steels, including pipeline steels such as X80 and X100, have different and complex microstructural arrangements based on their chemical compositions and manufacturing processes. For example, Thermo-Mechanical Controlled Processing (TMCP) routes followed by accelerated cooling (AcC) have usually been used for pipeline steels since 1985 to get a fully baintic structure and thus improve strength and toughness simultaneously. Optimizing the chemical composition and controlling the cooling rate are the main parameters to achieve the desired microstucture [33]. The classifications of pipeline steel are usually based on yield strength. Figure 2.2 shows the development of pipeline steels through the last few decades. Changes to HSLA steel manufacturing processing routes and optimization of HSLA steel chemistry have resulted in a steady increase in steel strength over the years. Overall the prevailing trend in chemistry is to reduce carbon content while adding alloying elements to achieve combinations of high strength and toughness through both grain refinement and precipitation strengthening.

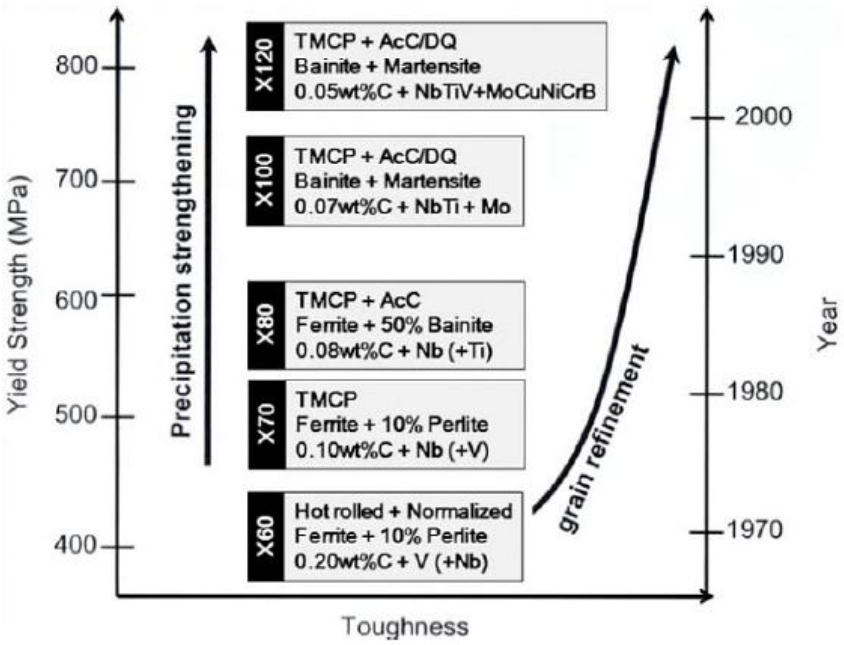

Figure 2.2: Development of linepipe steel over the time (Reprinted with permisson) [128]
.

One of the traditional methods of comparing steel chemistry is using the concept of carbon equivalent (CE). This is based on the concept that alloying elements (other than carbon) will increase the potential for martensite to form during accelerated cooling, thus increasing the hardness. There have been many experimentally derived formulas proposed for CE, and this will be discussed in a later section. It has traditionally been accepted that CE values greater than 0.4wt% were considered non-weldable due to the high likelihood of forming brittle martensite in the HAZ, which would crack during cooling of the weld [42]. Therefore, in order to weld HSLA steels the CE value should be maintained less than 0.4 wt%.

2.1.2 Pipeline steel

Steel makers use TMCP techniques with controlled cooling and chemistry optimization to produce grades with high strength. The increase in strength allows the fabrication of pipes with thinner walls, which directly affects the overall construction costs since lower weights are transported to a location, and less filler metal is needed to join each section. Figure 2.3 shows the reduction in pipeline weight achieved through the improvement in yield strength of pipeline steel [54, 69]

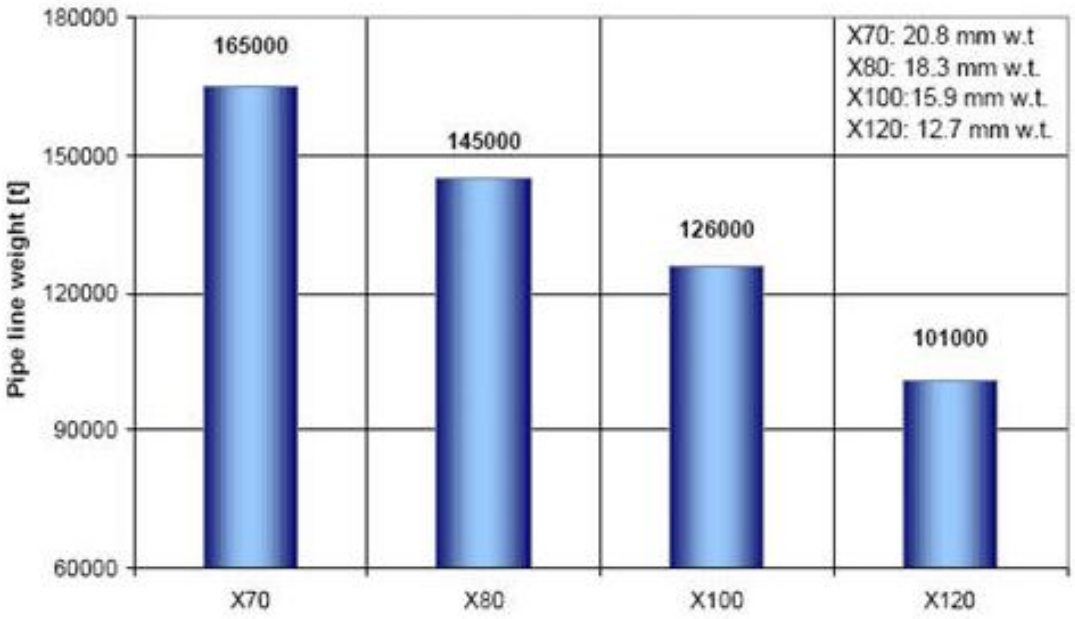

Figure 2.3: Reduction of pipeline weight when wall thickness (w.t.) decreases for high strength steel linepipe grades (Reprinted with permisson) [54]

.

X80 grade

The X80 linepipe steels, with their minimum specified mean yield stress (SMYS) of 80 Ksi (ie: 550 MPa), were the first produced by TMCP and accelerated cooling AcC, specifically to achieve a combination of a bainite and ferrite microstructure [53]. This provides the required fracture resistance at the specified yield strength. As shown in Figure 2.2, the progress since the 1970s in pipeline materials has produced increased yield strength, improved low temperature toughness, increased weldibility through reduced carbon equivalents, and optimized chemical composition. Figure 2.4 shows typical X80 base metal microstructure, which mainly is composed of fine bainite and ferrite, as expected for steel produced using a TMCP.

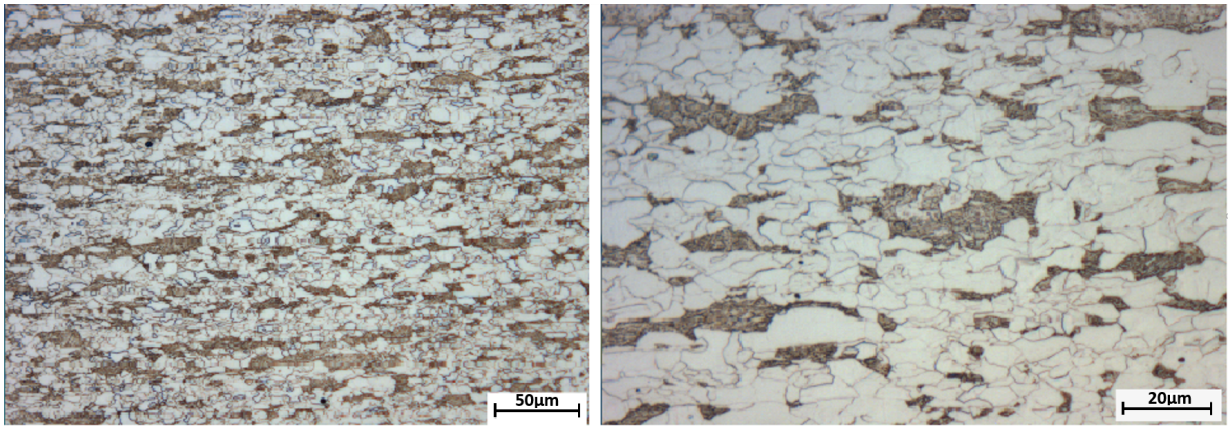

Figure 2.4: Optical microscopic image for X80 line pipe steel base metal structure consist of ferrite white phase and bainite dark phase.

X100 grade

Grade X100 steel was developed in the 1990s for long distance pipeline applications. The designation X100 refers to a SMYS of 100 Ksi (690 MPa). The X100 microstructure is designed to be higher strength through the application of TMCP techniques and accelerated cooling. There are multiple processing routes to achieve the strength needed for X100 steel. The microstructure of X100 steel is a mainly bainitic with some martensitic regions and a few grain boundary ferrite (GF) structures with an average size of 5 to 10 μm, with some elongated grains due to the TMCP rolling [95]. Optimizing carbon content, carbon

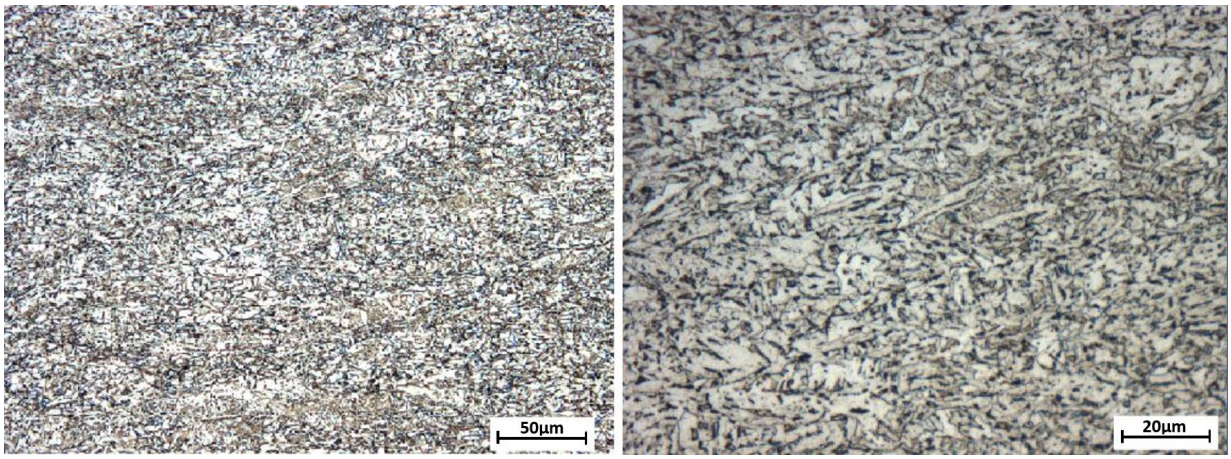

Figure 2.5: Optical microscopic image for X100 line pipe steel base metal structure consist of ferrite and bainite.

equivalent, the cooling rate and the cooling stop temperature during TMCP + AcC allows one to produce pipeline steel with high strength as shown in Figure 2.6 [69]. Various procedures were used to achieve sufficient mechanical performance and weldability, where Method (A) shown in Figure 2.6 in particular was effective for X100 by using a comparatively high carbon content and carbon equivalent. This method facilitates developing an

X100 plate at a low cooling rate and high accelerated cooling stop temperature. However, the disadvantage of this method is the lower weldability of the product, due to high carbon equivalent and lower HAZ toughness. Method (B) introduces low carbon content and carbon equivalent. The weldability could be improved using this approach although a decrease in the effective elements such as Ni, Mo, V, or Ti may reduce heat affected zone (HAZ) mechanical properties. Method (C) utilizes an intermediate carbon content level, and carbon equivalent tends to optimize production flexibility produces high toughness properties, good weldability, and better HAZ properties. [122].

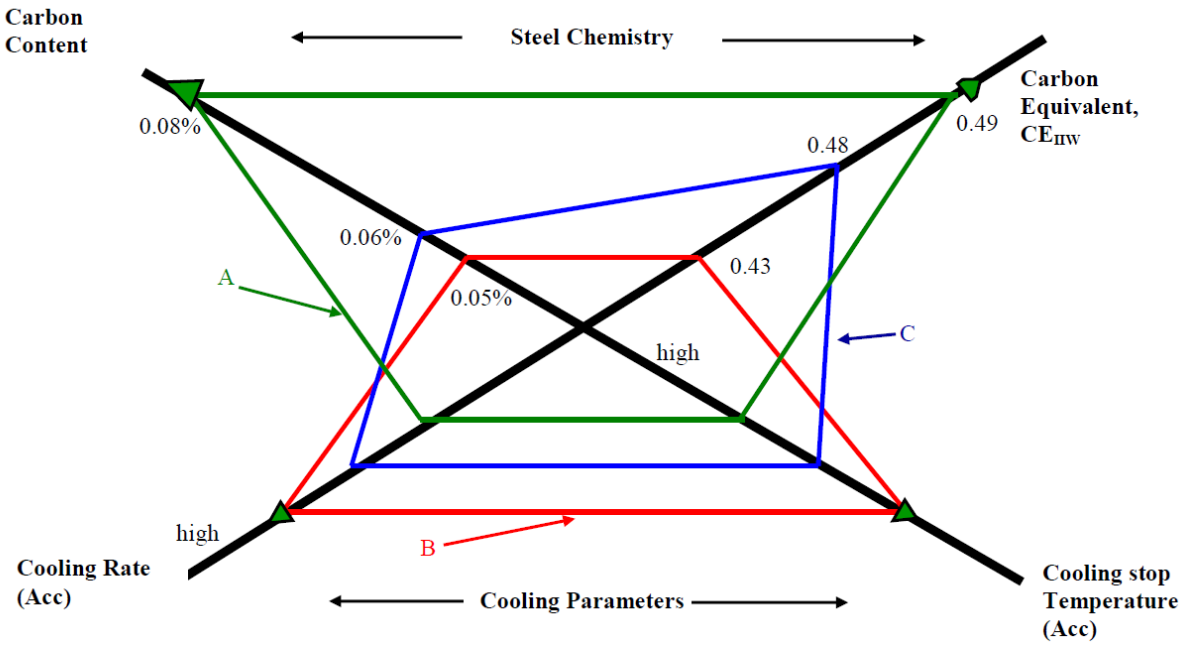

Figure 2.6: New approach to develop pipeline steel (Reprinted with permisson) [54, 122].

2.2 Thermo-mechanical controlled processing (TMCP)

During the past few decades of high strength steel development, the primary goal for steel makers has been to save weight, reduce cost, improve mechanical properties, and improve weldability. To achieve these goals, steelmakers developed alternative processing routes, such as TMCP, or quenching and tempering [119]. TMCP has been used since 1980 to improve mechanical properties for pipeline steel grades such as X80, X100, and X120 through optimizing the process parameters and chemical composition of the steel alloy. Additionally, the reduction of carbon content in pipeline steels lead to increases in the weldability of the steel and removed the need for preheat or post heat treatments [51]. The base metal microstructure varies based on the chemical composition, steel grade, and processing conditions. The TMCP techniques are typically used to control the resulting microstructure by the formation of effective precipitates, solid solution strengthening, and grain refined microstructures. Refined microstructures can be readily achieved by controlling cooling rates during rolling process. Using alloying elements, such as Ti, Nb, V, Ni, and Mo with small amounts (less than 200 ppm) of N, O, and maintaining C content in the range of 0.05 to 0.15wt% can produce sub-micron sized stable precipitates that can increase strength and toughness simultaneously [10]. Figure 2.7 shows a schematic diagram of the thermo-mechanically controlled process used to produce high-strength, micro-alloyed steel. After the initial heating to dissolve all precipitates, the steel is then deformed mechanically to induce recrystallization and refine the initial austenite grains. It is then rolled above the austenite-ferrite transformation temperature and at the same time below the recrystallization temperature to produce a heavily pancaked austenite structure [10]. In addition,

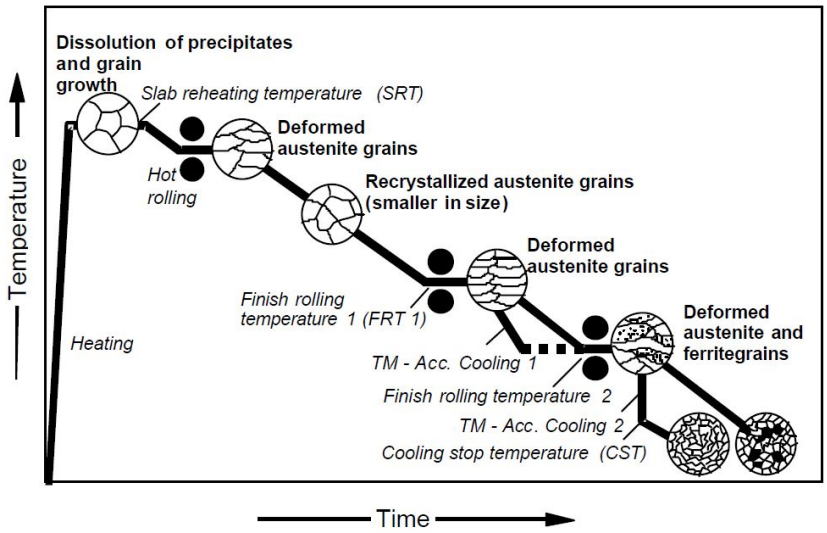

Figure 2.7: TMCP and AcC process diagram for steel (Reprinted with permisson) [68].

the grain refinement that occurs during the rapid-quench (AcC) is performed to meet the strain based design requirements, with respect to toughness and strength. The steel undergoes final deformation between 350 and 450 °C to increase the final dislocation volume fraction and promote formation of fine precipitates. The final rolling operation can also produce sub-grains to increase strength. The combination of rolling at high temperatures and accelerated cooling (TMCP + AcC) produces a very fine and favorable microstructure that has high strength and toughness, which are the main desirable properties for pipeline steel applications [51, 117].

The optimization of TMCP procedures is still under development, and in 1998 a new TMCP called Unconventional TMCP was developed to fabricate steel with high strength and toughness by producing microstructure that has a combination of bainite and fine dispersed particles of martensite-austenite (MA) constituents [128]. The processing routes

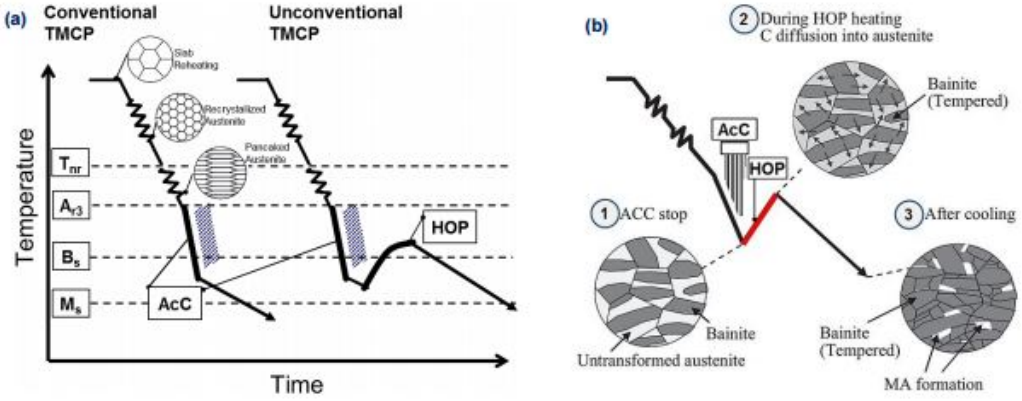

Figure 2.8: Complex thermo-mechanical controlled processing (TMCP) routes followed by accelerated cooling (AcC). a- TMCP and AcC diagram for conventional and unconventional processing. b- Microstructural changes promoted by HOP process (Reprinted with permisson)[111, 128].

shown in Figure 2.8-a, using the online heat-treatment process (HOP) and an advanced accelerated cooling device make it possible to achieve this microstructure combination. The main feature of the so-called unconventional TMCP technique is that induction heating is applied after the accelerated cooling process, which allows carbon to diffuse into austenite and produce the martensite-austenite (MA) constituents. Then the air is used to cool the structure to room temperature as shown in Figure 2.8-b [111, 128].

2.3 Effect of alloying elements

The key variable in determining material mechanical properties is the base metal microstructure designing, which can be achieved by optimizing the chemical composition in the base metal and welding zone. The main function of alloying elements is strengthening steel through different mechanisms, such as solid solution strengthening, precipitation

strengthening, and controlling the recrystallization temperature, which influences grain refinement. In this section the effect and motivation of adding various alloying elements and their typical content in pipeline steels is discussed briefly as follows [33, 128].

- **Carbon (0.03-0.1wt %):** Increases in carbon content leads to an increase in hardness and strength by forming carbides and increase in the amount of acicular ferrite at the expense of grain boundary ferrite. However, excessive increase in carbon content may lead to reduce ductility and toughness, which reduce weldability of steel. Therefore, the carbon content should be controlled to optimize toughness and improve weldability of steel [115, 138].

- **Manganese (1.5-2.0wt %):** Increases hardenability by changing microstructure to either acicular ferrite or martensite without deterioration impact toughness. Adding Mn with Nickel in the weld metal deposite will increase both upper and lower shelf of toughness and reduce the transition temperature[120, 160].

- **Silicon (0.1-0.6wt %):** Increasing Si content in the weld metal will improve strength by solid solution strengthening mechanism. In addition, Silicon has strong deoxidisng capabilites; therefore, it is usually added to remove extra oxygen during welding [88, 138]. In the HAZ, silicon has sometimes been observed to have a deterimental effect on toughness due to promotion of M-A constituents [33].

- **Nickel (0.2-1.5wt %):** Increases strength through interstitial solid solution strengthening. Nickel also promotes effective ferite strengthening, and at the same time increase toughness. Optimizing Ni with other alloying elements such as Mn offer a

good compromise between cost, strength, and toughness [88, 160].

- **Chromium (0.1-1.0wt %):** Increase steel hardenability due to formation of stable carbides. Adding chromium up to 1 % in the weld metal could raise the content of acicular ferrtie at the expense of grain boundary ferrite, above this level the structure will be dominted by baintic structure, which may reduce toughness [88].

- **Vanadium (0.03-0.08wt %):** Vanadium contributes to strengthening by forming fine precipitite particles in ferrite during cooling by lowering austenite to ferrite transformation temperature [38]. Vanadium also can form very stable carbides and nitrides, which improve the properties of the HAZs during welding since it is reduce the grain growth and promote fine grained transformation products [88].

- **Niobium (0.03-0.06wt %):** Niobium like vanadium is a very effective element to improve yield strength of steel since it is help to form carbides, which improve the strength by precipitation hardening and is considered a very effective ferrite grain refiner. [38, 43, 46, 159].

- **Titanium (0.005-0.03wt %):** Titanium is an efficient deoxidiser and have a strong affinity for carbon and nitrogen. Titanium forms fine TiN precipitates, which retard austenite grain growth in the HAZ. In the weld metal titnium form titanum carbides (inclusions TiO/TiO_2) that promote the formation of acicular ferrite structure. [45, 46, 100].

- **Boron (up to 500 ppm):** This is a powerful interstitial solid solution element, which increases hardenability and promotes a baintic structure by supperssing the

formation of polygonal ferrite. The combination of boron and titnium in the weld metals has been reported as a method to improve low temperature toughness properties [13, 82, 88].

- **Molybdenum (0.2-0.6wt %):** Improves strength and toughness simultaneously by promoting formation of acicular ferrite also improve strength by precipitation strengthening particularly in combination with Nb [82, 88, 105].

- **Oxygen (up to 250 ppm):** The oxygen helps to form non-metallic inclusions with elements such as titanium and manganese, which promote formation of acicular ferrite structure. Excessive increase in oxygen content in the weld metal will change size and distrbution of the non-metallic inclusions and that will promote the formation of undesirable weld microstructures such as grain boundary ferrite and ferrite side plates, due to a reduction in the prior austenite grain size. The toughness consequently decreases since the large inclusions provide crack initiation sites. [14, 88, 120, 137, 138].

- **Nitrogen (80-240 ppm):** Nitrogen, like boron and carbon has a small atomic radius and can fit interstitally within the steel lattice; therefore, improve strength. If nitrogen present with titanium will form nitride and improves toughness if the size of particles maintained less than 100 *nm*. In the weld metal if nitrogen present more than 300 *ppm* will cause porosity [14, 46, 88].

2.4 Weldability of pipeline steels

In welding metallurgy, the hardenability is generally used as an indicator of material weldability for steel alloys. Due to the formation of a high-volume fraction of hard phases such as martensite, martensite-austenite (MA) constituents, and carbides, which may increase hardness and reduce weldability. The key variables that should be taken in consideration involve the welding process, welding parameters, and material to be welded. One critical issue is to avoid martensite formation, which leads to excessive hardness and cracking in either the WM or HAZ. Hydrogen-induced cracking is usually expected when hardenability is high; therefore, the weldability of steel decreases and preheating process become necessary to avoid welding cracks. Some empirical equations take as input the carbon and content of alloying elements to predict the weldability of steel. Three primary carbon equivalent formulas have been widely used: the carbon equivalent based on the International Institute of Welding formula (CE_{IIW}), the Ito-Bessyo formula parameter crack measurement (P_{cm}), and the Yurioka formula (CEN). These formulas can be used for large groups of steel grades including microalloyed steel and pipeline steel. The CE_{IIW} formulas can also be used in the HAZ and WM to predict suitable preheat temperature and the post-heat temperatures, which may suppress martensite formation if it is a concern [97, 141]. The International Institute of Welding formula (CE_{IIW}) was developed in 1967 for steel that has carbon more than 0.18 wt%. In general, if the CE_{IIW} is less than 0.4 the steel will be weldable and the susceptibility to hydrogen cracking will decrease. However, preheat values in range of 100 to 200 °C are usually applied in pipeline construction to remove any moisture or contaminations (which may also be sources of hydrogen) from the workpiece

before welding [141].

$$CE_{IIW} = \mathrm{C} + \frac{\mathrm{Mn}}{6} + \frac{\mathrm{Cu{+}Ni}}{15} + \frac{\mathrm{Cr{+}Mo{+}V}}{5} \tag{2.1}$$

For steels with less than 0.18wt% carbon content such as those in the typical linepipe steels, C_{eq} formula devised by Duren [41] as shown in Equation 2.2 below is usualy used. P_{cm} formula also can be used in this case, the P_{cm} was developed by Japanese researchers Ito *et al.* [76] to describe the hardenability of pipeline steels. The elements listed in equation 2.3 represent the alloy content, in weight percent, for particular steel alloy. The value of P_{cm} is only valid for steels with less than 0.22 wt% carbon. The P_{cm} is a good predictor for hydrogen induced crack susceptibility, and should be in a range less than 0.25 to avoid cracking in low alloy high strength steel [76].

$$C_{eq} = \mathrm{C} + \frac{\mathrm{Si}}{25} + \frac{\mathrm{Mn{+}Cu}}{16} + \frac{\mathrm{Cr}}{10} + \frac{\mathrm{Ni}}{40} + \frac{\mathrm{Mo}}{15} + \frac{\mathrm{V}}{10} \tag{2.2}$$

$$P_{cm} = \mathrm{C} + \frac{\mathrm{Si}}{30} + \frac{\mathrm{Mn{+}Cu{+}Cr}}{20} + \frac{\mathrm{Ni}}{60} + \frac{\mathrm{Mo}}{15} + \frac{\mathrm{V}}{10} + 5B \tag{2.3}$$

The CEN formula was developed by Yurioka in 1987, and it was also proposed for the use of microalloyed steels. Yurioka showed strong relationship between CEN formula and P_{cm} formula for low alloy steel with carbon content less than 0.17 wt% [157].

$$CEN = \mathrm{C} + \mathrm{A(C)} \times \frac{\mathrm{Si}}{24} + \frac{\mathrm{Mn}}{6} + \frac{\mathrm{Cu}}{15} + \frac{\mathrm{Cr{+}Mo{+}Nb{+}V}}{5} + 5B \tag{2.4}$$

where:

$$A(C) = 0.75 + 0.25\text{tanh}[20 \times (\text{C} - 0.12)] \tag{2.5}$$

In this study C_{eq} formula developed by Duren [41] and P_{cm} formula suggested by Ito *et al.* [76] were used to determine the steel weldability since the line pipe steel in this work contains carbon less than 0.1 wt%.

2.5 Welding processes

Manual Shielded Metal Arc Welding (SMAW) and mechanised Gas Metal Arc Welding (GMAW) are usually used in the field for welding of high strength pipeline steels. Mechanised GMAW techniques are more common considering they offer higher productivity, which is beneficial considering the long distances required for natural gas transportation involving large diameter and high-pressure pipeline. This technique also allows fabricators to reduce the overall cost, while maintaining both strength and toughness at high level [95, 134].

2.5.1 Gas metal arc welding (GMAW)

The GMAW process melts and joins metals by heating them with an arc established between a continuously fed filler wire electrode and the base metals, as shown in Figure 2.9. Shielding of the arc and the molten weld pool is often obtained by using inert gases such

as argon or helium, which is why GMAW is also called the metal inert gas (MIG) welding process. Since non-inert gases, particularly CO_2, are also used, the acronym GMAW is used as a more general term [78, 134].

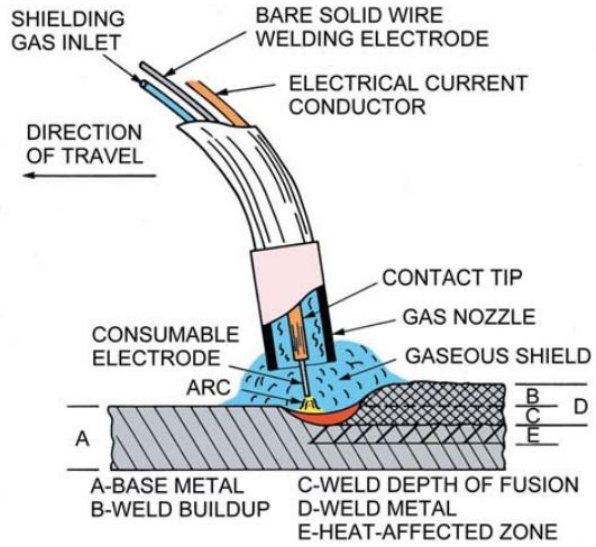

Figure 2.9: Schematic diagram of GMAW process (Reprinted with permisson) [78]

.

2.5.2 Heat input consideration

Heat input is a relative measure of the energy transferred per unit length of weld. It influences the cooling rate as shown in Figure 2.10, which may affect the resulting mechanical properties and microstructure of the weld region. In general, increases in the heat input lead to a decrease in cooling rate and reduced strength and hardness due to formation of soft zones in the microstructures, while impact toughness may increase [47].

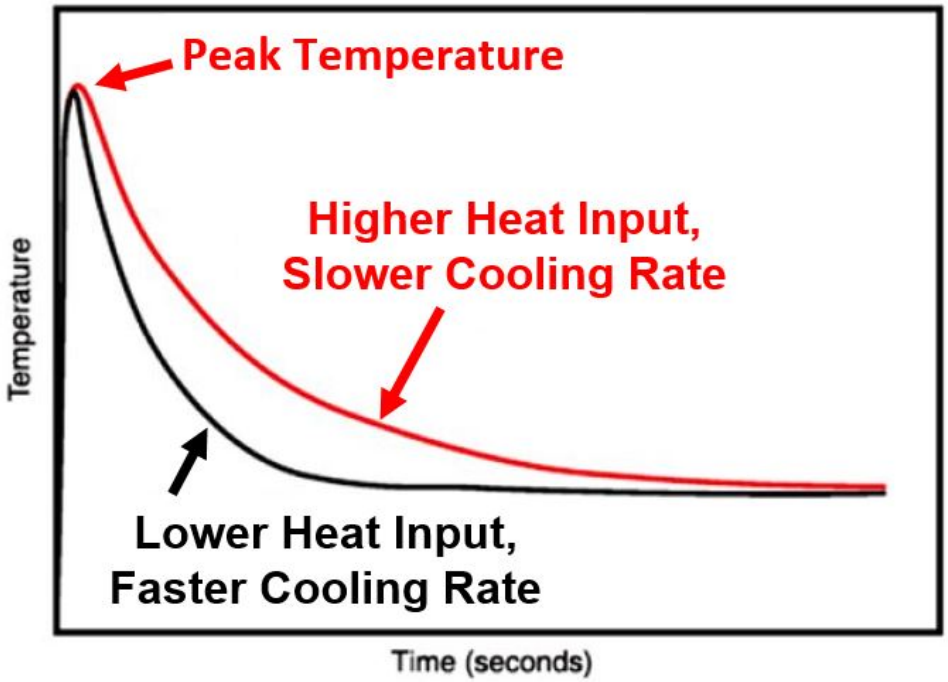

Figure 2.10: Effect of heat input on cooling rate adpted from [47].

To calculate the heat input, the main parameters that directly influences the weld thermal cycle should be monitored accurately. The traditional method is to calculate heat input by measuring average or RMS values for voltage and current, and calculating the product of these divided by the travel speed per minute, as shown in equation 2.6.

$$HeatInput = \frac{Voltage \times Current \times 60}{TravelSpeed \times 1000} \tag{2.6}$$

where: Voltage: average or RMS voltage in Volt, Current: average or RMS current in Ampere and Travel speed: mm/min, Heat input: kJ/mm.

Increasing the current generally leads to increase width, penetration, and reinforcement

of the weld bead. Meanwhile, voltage can be changed by controlling the arc length or stick-out length (ie: length of electrode between the arc and the contact tip), The bead width and deposition rate will vary according to arc length; where a high arc length usually creates high voltage, while increasing stick-out length is usually associated with lower voltage values, which increase reinforcement height and decreases the bead width. Moreover, using other power supply waveforms such as pulse mode, constant current (CC), and constant voltage (CV) will affect the voltage and current values [117, 158]. In this work, constant voltage mode was used to create all the welds.

2.6 Welding metallurgy

The latest grades of linepipe steels are usually produced by the TMCP and AcC process with alloying elements such as Nb, V, Ti, Ni, and Mo. These elements can produce strong and stable carbide, nitride, and oxide particles. Therefore, the strength and toughness is increased significantly in TMCP by contributions from solution strengthening, precipitation hardening, and grain refinement as discussed in the previous section [38]. The effect of strengthening methods can be reduced significantly during welding process due to the high temperatures experienced, especially in the HAZ. The extent of the HAZ depends on the heat input value, as the heat input increases the HAZ peak temperature increases, which allows grain growth to occur close to the fusion line and leads to coarsening of the austenite grains. This is often accelerated by the dissolution of carbides and nitrides particles, which also decrease the precipitation strengthening contribution to microstructure and therefore, mechanical properties will be decrease. To improve toughness in the HAZ, Ti

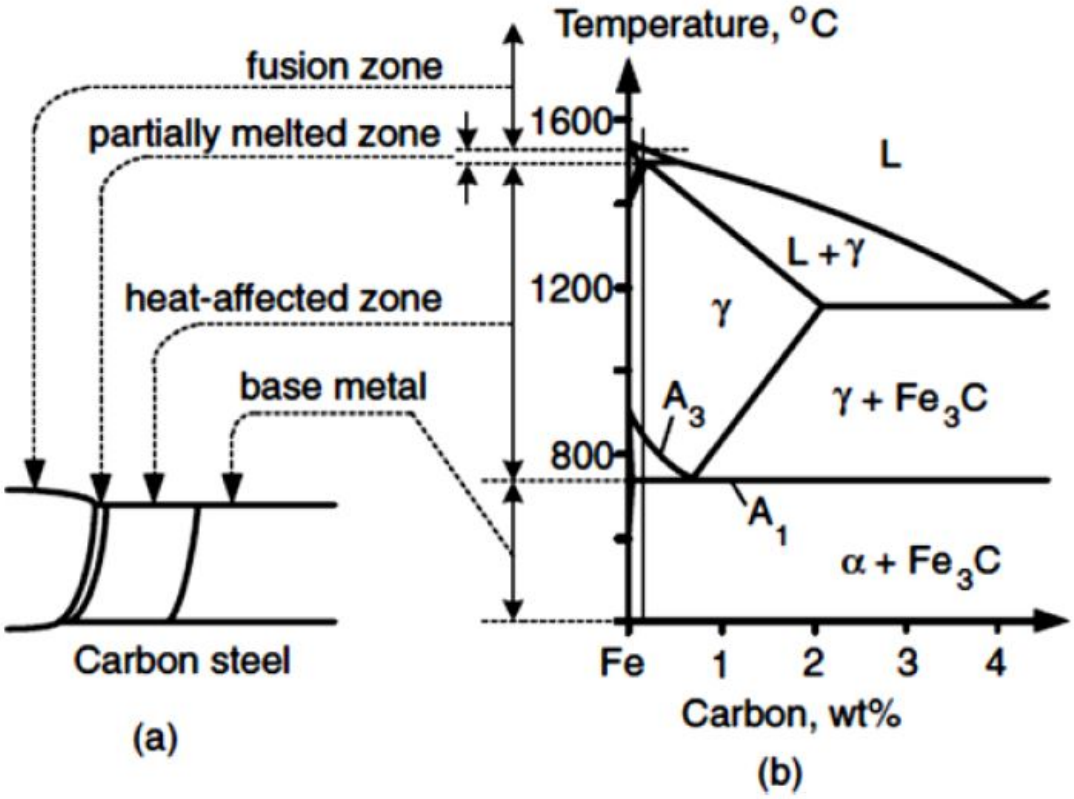

Figure 2.11: Iron-carbon phase diagram with schemtic diagram shows thermal cycle of welding process (Reprinted with permisson) [134].

and N contents should be optimized to be closed to stoichiometric ratio Ti/N=3.42, which promotes pinning of austenite grains by forming TiN particles as reported by Baker [13]. The range of the thermal cycle for each zone in the welding joint schematically described in the Figure 2.11.

2.6.1 Weld metal (WM)

In order to weld pipeline the weld joint consists of numerous weld passes, which create heterogeneous weld metal due to the multiple thermal cycle. As a result, the weld metal microstructure change from location to another based on the thermal history. The weld metal microstructure can be classified into as-deposited weld metal, which experience single thermal cycle as in the case of the cap pass and root pass. The second region is called reheated weld metal, which is reheated in the subsequent weld passes. Therefore, solid state reconstructive and displacive transformation products may be found in the weld metal and HAZ [87]. In this section the typical microstructures usually formed in the pipeline fusion zone such as acicular ferrite, bainite, Widmanstatten ferrite, and grain boundary ferrite will be discussed briefly.

- **Acicular Ferrite**: The desirable weld metal microstructure formed in the pipeline steel welds is acicular ferrite (AF) or sometimes referred as a "basket-weave structure". It is generally accepted that acicular ferrite microstructure has high strength and toughness due to the interlocking plate shape with fine grain size and high angle grain boundaries, which improve strength and toughness simultaneously [62, 75]. It is reported that the aspect ratio of the acicualr ferrite ranges from 1:4 to 1:10 μm with a very fine ferrite grain size (Typically 1 to 3 μm) [11, 19, 60]. In order to form acicular ferrite microstructure nonmetallic inclusions such as MnO, TiO, TiN, and AlO should be presented in the weld metal microstructure. These inclusions work as a nucleation sites for the acicular ferrite within the austenite grains [17, 103]. To this end large prior ausenite grain size with controlled oxygen content ($\simeq 200ppm$)

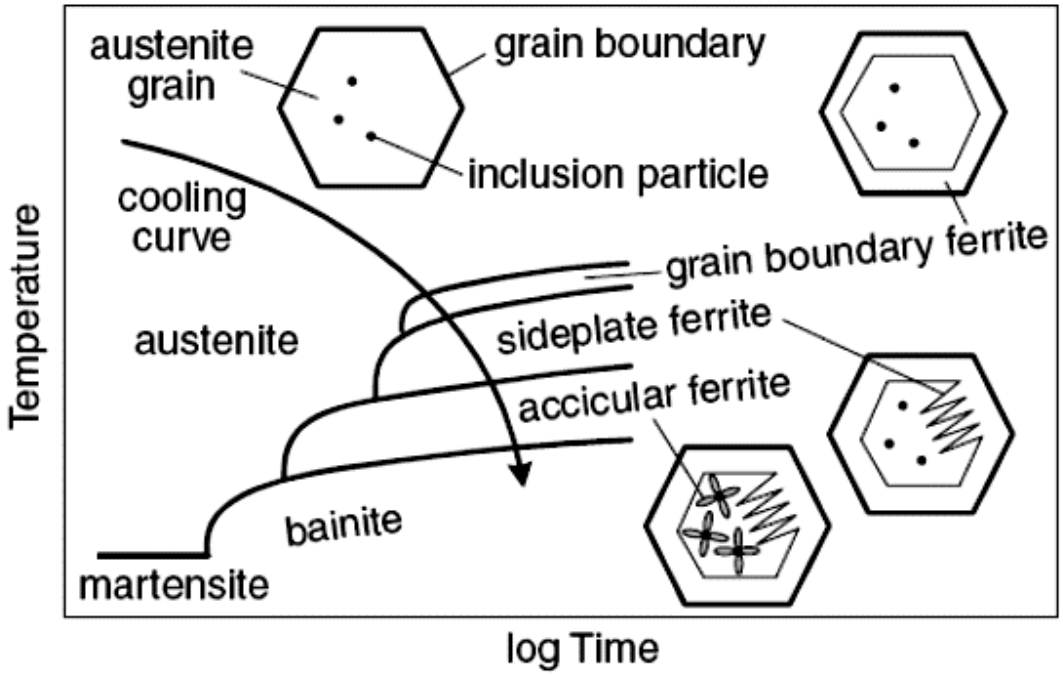

Figure 2.12: Schemtic daigram shows acicualr ferrite zone on CCT for high strength low alloy steel (Reprinted with permisson) [134].

and balance of microalloying elements such as Ti, Mn, Mo, Nb, and V could lead to increase the formation of acicular ferrite microstructure [60, 87, 144]. In addition, the cooling rate and particles dispersion effect as can be seen in schemtic diagram in Figure 2.12 should be considered as well in order to form the acicular ferrite microstructure [87]. However, as mentioned before the multipass welding process that is usually used in the pipeline welding may alter the formation of acicular ferrite in the overall joint due to the multiple thermal cycles [103]. Therefore, other microstructures such as upper/lower bainite and Widmanstatten ferrite may form, which leads to reduction in toughness of the weld metal [60]. The formation of such

phases depends upon many parameters, such as the cooling rate, peak temperature, preheating temperature, shielding gas composition, and chemical composition of the welding consumable [87, 145].

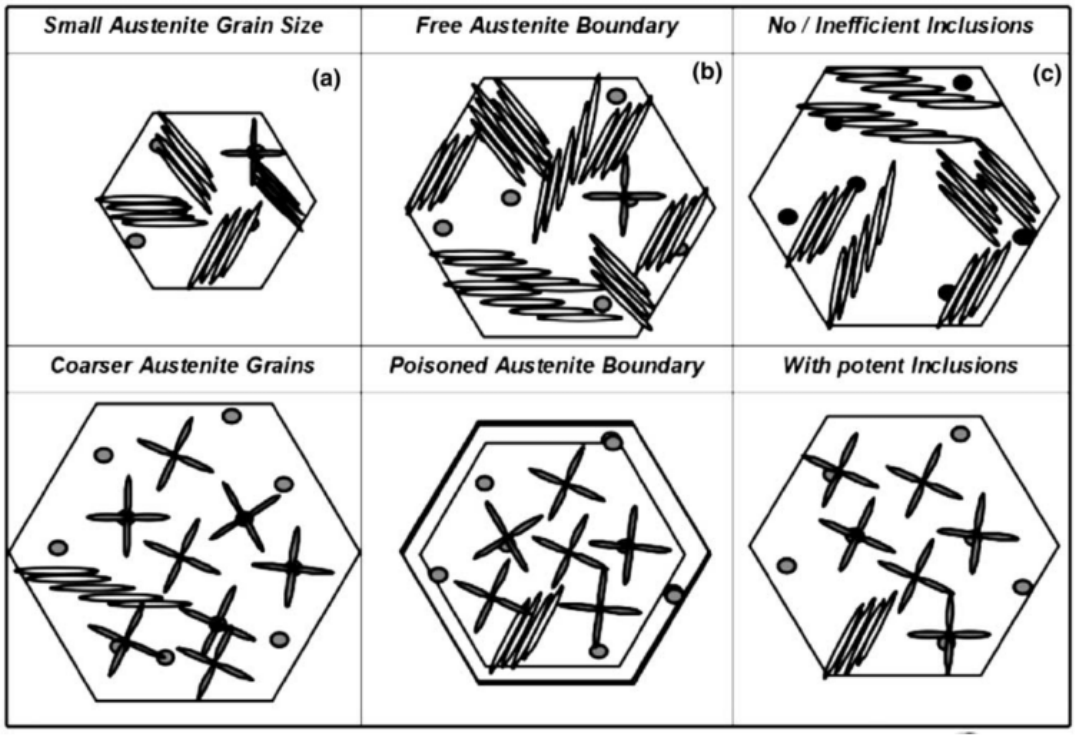

Figure 2.13: Schematic illustrations of different mechanisms by which bainite transformation can be stifled to obtain predominantly acicular ferrite: (a) Austenite grain size effect: with large grain size, the $\gamma - \gamma$ grain boundary area per unit volume decreases for a given inclusion density. (b) Poisoned austenite grain boundary: by forming a thin layer of allotriomorphic ferrite, the $\gamma - \gamma$ grain boundary can be made ineffective due to reduced area of favorably oriented α/γ interface, as well as, carbon enrichment near the interface (c) Presence of potent inclusions: for a given austenite grain if we increase the number of potent inclusions, then acicular ferrite nucleation will be favored. Note: γ refers to the austenite, and α refers to the ferrite.(Reprinted with permisson) [11, 12]

- **Bainitic microstructure**: Bainite can be classified into two categories, namely

upper bainite and lower bainite, which have distinct structure based on the transformation temperature. If the carbon precipitates as cementite between the ferrite plates this is classified as upper bainite structure. In the case of lower bainite the carbides precipitates between and within the ferrite plates. The bainite laths may grow directly from the prior austenite grain boundary referred to as FS(A) in the IIW classification [34] or interagranular bainite, which grows from the non-metallic inclusions inside the prior austenite grain. Thewlis [145] referred to this as I(B). This depends on the density and size of inclusions and may result in a very fine structure like acicular ferrite.

- **Widmanstatten ferrite (WF) microsructure**: In the weld zone and HAZ the bainite and widmanstatten ferrite microsructures can be easily confused. Therefore, this structure is sometimes referred to as ferrite with second phase (FS). WF may be expected to occur at higher temperature than upper bainite and exhibit a generally coarser microstructure. In addition, the microconstituent between the WF plates may be expected to be mixture of martensite-austenite or bainite. The primary WF plates grows directly from prior austenite grain boundary and it is difficult to identify them. IIW classified the WF with aligned microphase FS(A) that grows from existing allotriomorphic ferrite as secondary ferrite [34, 145]. Therefore, in order to distinguish the WF structure from upper bainite colour etching method may be used to identify them. Nano-hardness measurements technique also can be used to distinguish the WF structure from upper bainite, WF should exhibit a lower hardness compared to upper bainite [145].

- **Grain Boundary Ferrite (GBF) microsructure**: When high heat input is applied with lean welding consumables are used in the welding process, reconstructive transformation may take place. The transformation from austenite to ferrite occurs by a reconstruction process and diffusion process will be involved. Prior austenite, along with grain boundary ferrite (GBF) or polygonal ferrite (PF) structures may form. As a result the mechanical properties of the weld metal or HAZ will be reduced due to the presence of these coarser structures.

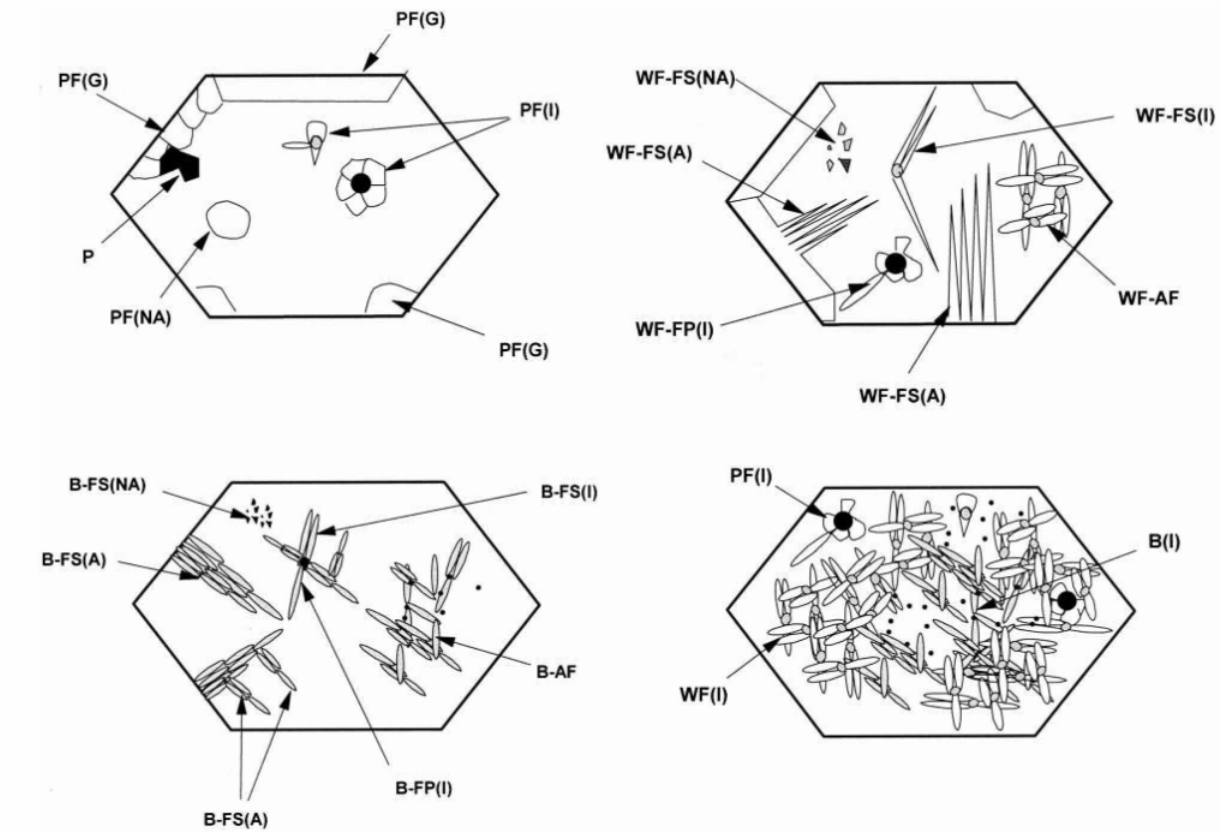

Figure 2.14: Schematic illustrations show different $\gamma - \alpha$ tranformation products based on Thewlis classifaction (Reprinted with permisson) [145].

2.6.2 Heat affected zone (HAZ)

The typical mirostructure for X80 line pipe steel is a combination of ferrite and bainite, which can provide high strength without any loss in toughness. However, during the welding process that initial balance between strength and toughness in the BM can be lost in the HAZ due to the thermal cycle of the weld [95]. The schematic diagram in Figure 2.15 illustrates different HAZ regions that usually form in single pass weld (a) and a multipass weld (b). Depending on the steel grade and operting condtion, the thickness of the linepipe is ranged from 12 mm to 25 mm. It is normally necessary to perform multipass weld to fill a pipeline joint with a wall thickness of more than 6 mm. Softening in the HAZ usually occur due to the experience of high temperature, which may dissolve some precipitate particles or reheated and normalized in HAZ. Therefore, a reduction in the mechanical properties such as strength and toughness is expected. To avoid this dilemma steel makers have developed new technology, which involves dispersing fine TiO particles in structure of the base metal. TiO particles present inside of the austenite grains serve as nuclei of intragranular ferrite (IGF) [110, 143]. By doing so, the austenite grains will be pinned and as a result the mechanical properties of the HAZ could be improved. The HAZ temperature varies from about 1450 °C close to partially melted zone (PMZ) to about 723 °C close to the A1 temperature boundary as shown in the Figure 2.11, which defines the upper limit where austenite is stable. The cooling rate will vary based on the peak temperature of each zone.

Therefore, the HAZ can be classified into four zones based on the thermal cycle, peak temperature, and grain appearance. However, it should be noted that the chemical com-

position remains constant across the HAZ since it remains below the melting point [97]. Brief introduction about each HAZ region is presented below:

- **CGHAZ** : The coarse grain heat effected zone (CGHAZ) usually experiences temperatures above the A3 temperature, typically from about 1000 °C to 1450 °C. Due to the high temperature history the precipitate particles dissolve and no longer pin the austenite grain boundaries, which allows the grain size to increase. The microstructure and mechanical properties can vary widely in the CGHAZ based on the base metal chemical composition, microstructure constituents, and welding parameters [42].

- **FGHAZ**: The fine grain heat effected zone (FGHAZ) experiences temperatures above A3 in the range of 1100 °C to 850 °C, where carbide and carbonitrides precipitates do not dissolve completely and continue work to pin the austenite grain boundary movement [115]. The grains are actually refined in this region as a result of the recrystallization that occurs, however time and temperatures are not sufficient to cause growth of the newly recrystallized grains.

- **ICCGAZ**: The intercritical region (ICCGHAZ) usually exposed to temperature in range between A1 and below A3, and the microstructure is mixture of ferrite and austenite as shown in the Fe-C phase diagram 2.11. Upon cooling the austentite will transform to another phase and that depends on cooling rate [115].

- **SCGHAZ**: In the subcritical heat effected zone (SCGCHAZ), the temperature does not exceed the A1 temperature, in which case no austenite can form, such that the

microstructure remains almost same as base metal microstructure. However, the precipitation of carbides in martensite may occur in this region [44].

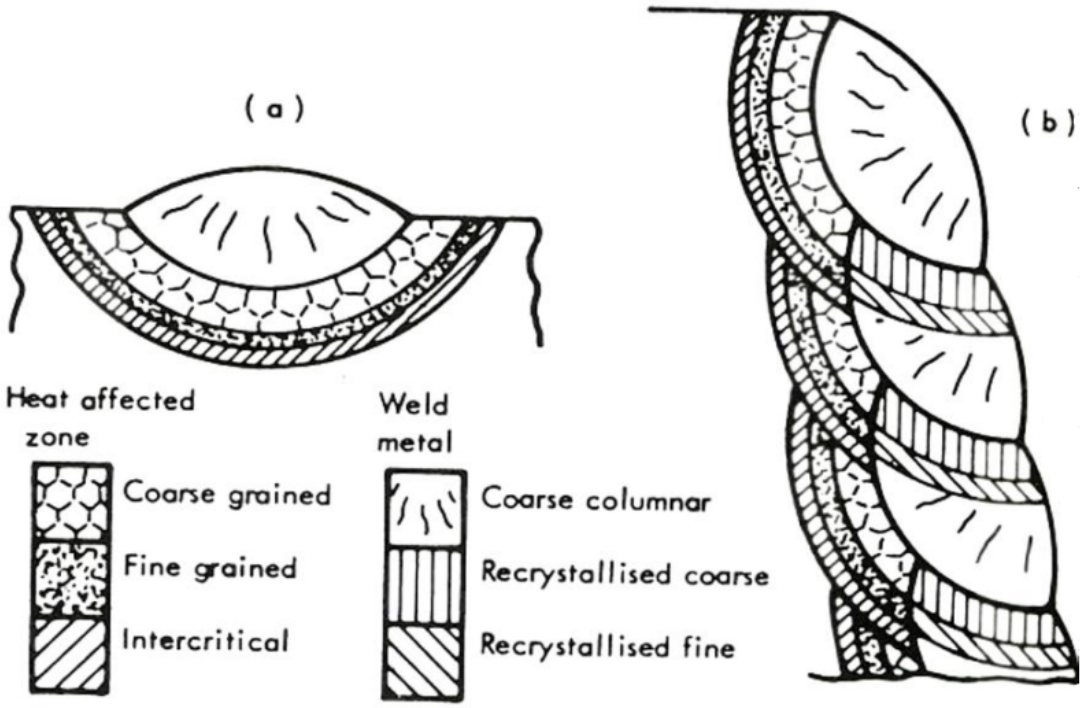

Figure 2.15: Schematic diagram shows different HAZ and WM formed in a)- Single pass weld b)- Multipass weld (Reprinted with permisson) [42].

2.7 Strain based design (SBD) criteria for pipelines

Most of the active pipeline design standards are based on a stress criterion that is considered suitable for steel with a known yield point and tensile strength. However, the stress in long-distance pipelines may exceed the yield point under some situations, typically following

shifts in the soil, or in harsh terrains, earthquakes, and landslides. In these situations, owing to the displacement controlled loading, strain-based design criteria are used in modern cross-country pipelines. These are designed to allow stress to exceed beyond the yield stress such that some plastic deformation occurs during service or installation even though the pipeline is still able to meet the operation requirements [104]. In order to design according to strain criteria there are some important requirements that should be achieved such as high toughness at low temperatures, high ductility or high strain capacity, and weld strength overmatching. In this work, the focus will be on weld strength overmatching.

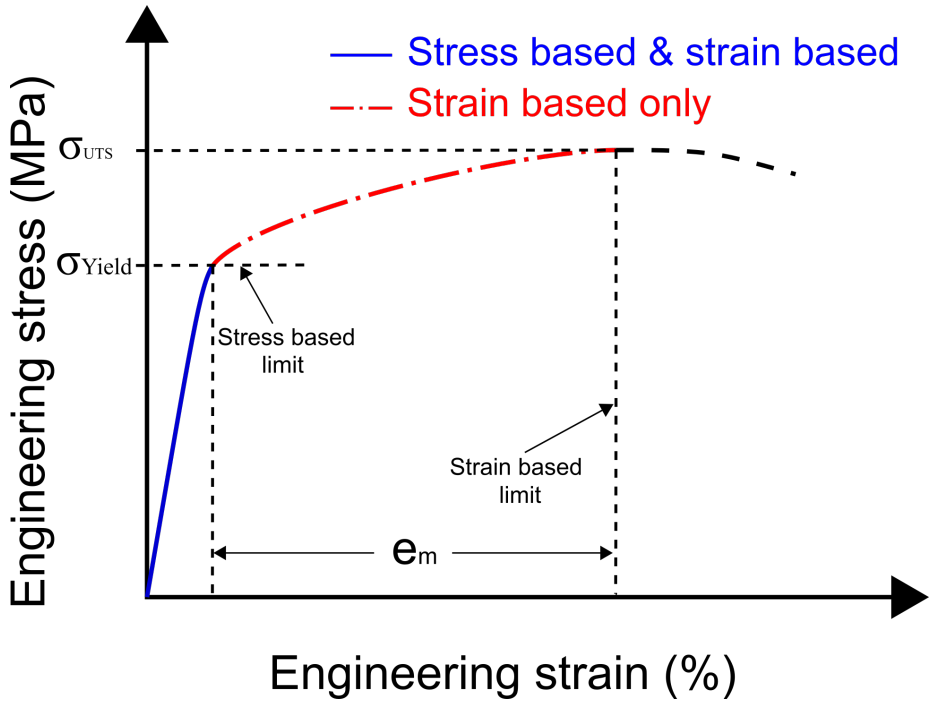

Figure 2.16: Strain based versus stress based design adpated from[128].

2.7.1 Strength overmatching

Strength overmatching is considered one of the main requirements for modern pipeline steels and can be defined according to the DNV-OS-F101 standard as achieving a weld metal tensile yield strength, which is higher than the yield strength of the parent pipe for all material conditions and strain levels under consideration [39]. Welding procedures and specifications using existing welding technologies such as GMAW and SMAW for producing joints with good toughness and strength have been developed to achieve this requirement for various pipeline grades [72, 89, 108]. However, meeting the specified minimum strength requirements for pipeline applications to overmatch base metal strength remains a challenge currently facing the pipeline industry. Some investigations have reported that undermatching the WM strength will cause straining of the weld, while overmatching the weld metal strength causes gross section yielding in the pipe [95] or may potentially lead to strain localization in the HAZ. In general, for pipeline applications the common strategy is to produce a weld metal strength, which overmatches the pipe yield strength; however, this can lead to some undesirable results when applied to higher strength pipe, such as X80 or higher grades [153]. For instance, when welding processes are selected such that the yield strength of the material in the weld region increases, the toughness of the weld region decreases and susceptibility to weld cracking becomes a concern [52, 121]. The DNV-OS-F101 standard specifies that an overmatch limit for longitudinal girth welds exposed to strains less than 0.4% should be at least 80 MPa above SMYS of the base metal for offshore applications [39]; however, no specific magnitude of overmatching has been imposed for onshore applications in Canada.

Early work done by Funderburk concluded that matching strength is not formally specified for all joints according to the American Welding Society [48]. Although, it is generally expected that the strength of the weld metal should be equal or greater than base metal strength for groove joints and tensile load applications. In pipeline applications, pipe loads during events such as earthquakes, soil sliding or even during the fabrication in the field may result in pipe stresses, which go beyond the elastic region. Under these severe loading conditions, it is therefore preferred to distribute the deformation throughout the base metal. If weld metal strength undermatching occurs, collapse in the weld metal may occur, since the size of the joint relative to the pipe is small, resulting in strain localization in the weld joint [48]. Recently, Hertele [65] conducted a numerical study to assess the effect of weld strength mismatch on strain capacity for pipeline welds. The conclusion was that the relation between strength overmatching and strain capacity is approximately linear up to the point of collapse. The definition of overmatching used in that study was based on the flow stress which is (average of yield strength and ultimate tensile strength) [65]. Hertele also studied the effect of strength overmatching on crack driving force and found that driving force of a flaw is reduced as the degree of weld strength overmatch increases. In addition, he concluded that the overmatching level increase can shield the WM and adjacent area (HAZ) from failure and shift the failure toward the base metal [65].

Bally [15] studied the local properties of pipeline girth weld by means of hardness mapping technique, and reported that when strength overmatching is considered the calculation of the strength mis-match should be done based on the minimum yield strength value in the weld zone. However, to the best knowledge of the author of this thesis, no research has been done to characterize the weld metal in different directions to check whether the

weld displays isotropy in the yield strength, and the impact of the anisotropy on over-matching criteria. Therefore, in this work, the strength of the weld will be characterized in different directions to investigate the properties of weld and effect of that on the strength mis-matching. The strength mis-match will be defined based on yield strength as described in the equation 2.7.

$$M = \frac{\sigma_{y(Weldmetal)}}{\sigma_{y(Basemetal)}} \tag{2.7}$$

2.8 Elastic-plastic property evaluation using indentation method[1]

2.8.1 Hardness correlation method

Hardness tests have been used for a long time as standard method to characterize engineering materials in the metal industry and research, since it provides an easy, reliable, nondestructive, and inexpensive method. In the hardness test hard indenter made of diamond or tungsten carbide is usually used. By measuring the indentation area left by the indenter shape and knowing the applied load, the hardness number can be determined. There are three different standard methods to represent hardness number: Vickers, Brinell, and Rockwell hardness test. In the current study Vickers hardness test was used to measure hardness value for pipeline joints as required by the standards such as API-1104, CSA

[1]Part of this section has been published in International Journal of Solids and Structures on 29 September 2016,available online:http://dx.doi.org/10.1016/j.ijsolstr.2016.09.036,A.R.H. Midawi,C.H.M. Simha, M.A. Gesing, A. Gerlich, Elastic-plastic property evaluation using a nearly flat instrumented indenter.

Z662-15, and DNV-OS-F101 [6, 39, 74]. The Vickers hardness test use pyramid indenter geometry with 136 ° between the faces. The hardness test data has been used to estimate yield strength for metals and alloys using statistical correlations or strain hardening response. For instance,the relationships for yield stress presented by Tabor in 1951 [140] proposed the following equation to estimate yield strength based on hardness value for some engineering materials:

$$\sigma_y = \frac{H}{3} \tag{2.8}$$

for the case of copper, while a ratio of:

$$\sigma_y = \frac{H}{2.9} \tag{2.9}$$

was suggested for steel. However, the Tabor's formula assumes the strain hardening coefficient to be equal to zero. Other researchers who studied the effect of strain hardening coefficient such as Marcinkowski *et al.* [3] found that $\sigma_y = H/5$ for annealed Fe-Cr alloys, and Speich and Warlimont [49] found that $\sigma_y = H/4$ for some low carbon martensitec Fe-Ni alloys.

Later in 1971 Cahoon *et al.* [24] modified Tabor equation to be more general, which takes into account the strain hardening coefficient or Meyer's coefficient as in the equation shown below:

$$\sigma_y = \frac{H}{3} \times (B)^{(m-2)} \tag{2.10}$$

where H is the Vickers hardness number, B is a constant depend on the material type, and M is the Meyer's hardness coefficient. The strain hardening coefficient can then be calculated as described by Cahoon *et al.* [23] using the following equation:

$$n = (m - 2) \tag{2.11}$$

However, this method requires performing several indentations with varying loads and indenter diameters as well as a regression analysis on a load versus indentation diameter plot. It is our experience that there is a significant experimental error associated with this approach especially for the high-hardening steels evaluated in this work. In addition, in some cases materials can not be extracted to perform tensile test and determine strain hardening coefficient such as the case of the HAZ. Therefore, these correlations can not be used without knowing the strain hardening coefficient.

2.8.2 Instrumented indentation technique

Many studies over the recent decades were done to determine mechanical properties for engineering materials using hardness testing as discussed in the previous section. However, this has faced with great difficulty until the recent advances in technology based on instrumented indentation testing. This indentation test allows one to measure force as a function of the penetration depth during the indentation process as shown the schematic diagram in Figure 2.17. This has motivated comprehensive experimental, theoretical and numerical investigations exploring the mechanical property characterization of materials using instrumented indentation technique [147].

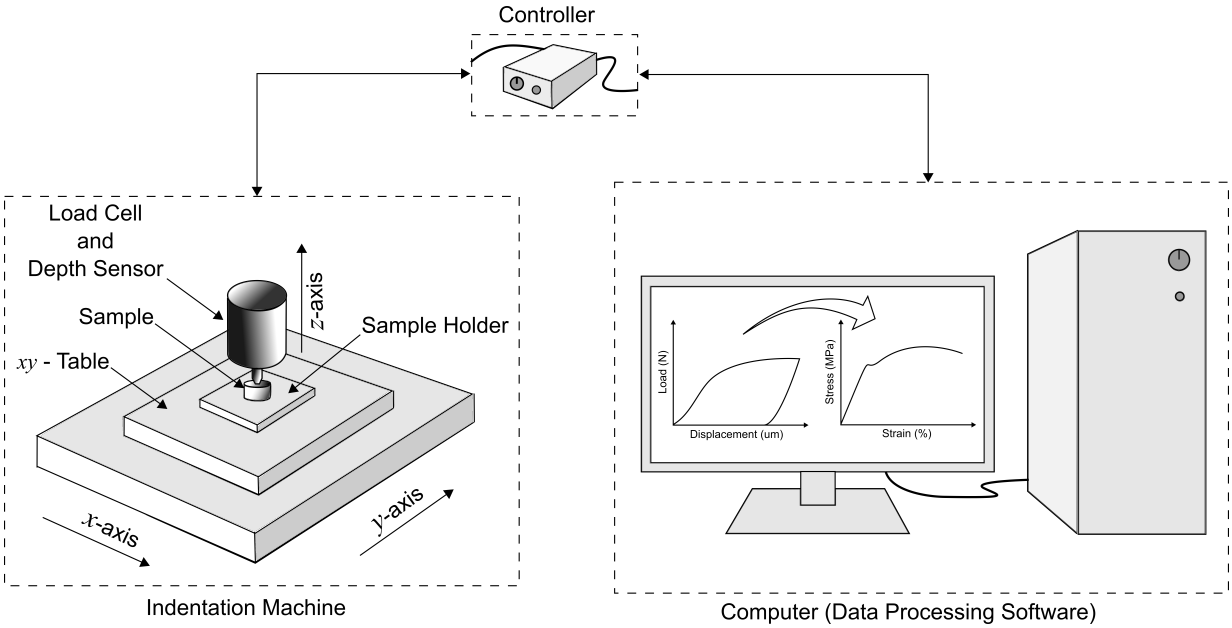

Figure 2.17: Schematic diagram shows the instrumented indentation process.

Early work on instrumented indentation using micron-sized sharp indenters was carried out by Wierenga *et al.* [150] for characterizing metal thin films and polymers, and by Loubet *et al.* [99] for elasto-plastic assessment of magnesium oxide. Subsequently, Oliver *et al.* [113] developed the technique of nano-indentation (or ultra-low load indentation) using nano-sized sharp indenters for modulus and hardness evaluation. For recent reviews, see the articles by Oliver *et al.* 2004 [114] and Vanlandingham *et al.* 2003 [147]. A marked limitation associated with a sharp indenter is that the maximum strain that can be attained, is limited to approximately 8% per indentation; this can be mitigated by the use of spherical indenters wherein the maximum strain is governed by the radii of indenter and contact area. Representative instances of instrumented spherical indentation to obtain elastic moduli and flow curves may be found in articles by Taljat *et al.* [142], Herber *et*

al. [63], Nayebi *et al.* [107], and Beghini *et al.* [16].

For the most part, determination of hardness using either the sharp or the spherical indenters has relied on empirical models and/or cavity expansion theory. Bhattacharya *et al.* [20] augmented instrumented indentation with finite element computation; they were able to obtain estimates of elastic moduli (using the unloading response) and hardness from sharp indentation tests and computations. This is the so-called forward approach, wherein the tensile stress-strain response, obtained using uni-axial stress test, is used to model the indentation test. In instrumented indentation, especially with spherical indenters, the strain range achieved is comparable if not higher than the ultimate strain obtained using dog-bone specimens is feasible (see subsequent citations). Large-scale finite element computations of sharp indentation were also carried out by Giannakopoulos *et al.* [50] to obtain empirical relationships for yield, moduli and hardness to within 10% uncertainty. Subsequent improvements to the foregoing approach may be found in the article by Dao *et al.* [36]. Representative instances of similar efforts for spherical indenters can be found in the articles by Alcala *et al.* [2], Taljat *et al.* [142], and Nayebi*et al.* [107]. In many of the foregoing schemes, empirical relationships or non-dimensional force-displacement relationships calibrated using computations are in the context of an inverse approach to extract elasto-plastic properties - no repeated finite element computations are required for the inverse approach. A limitation of these methods is a partial reliance on empirical relationships, or the assumption of a hardening model in calibrating the relationships, which constrains application to materials that conform to the model. The reported uncertainties in the evaluated yield and hardening properties could be 10% or higher.

To reduce the uncertainty in estimation of elasto-plastic properties, the inverse (some-

times called reverse) approach has been developed and this approach does not require any empirical relationships. Herein, an initially assumed stress-strain curve for the substrate (Swift, Hollomon, or Voce laws) is used to model the indentation test and if the computed load-displacement curve does not match the indentation curve to within a specified tolerance, the finite element simulation is repeated after adjusting the assumed stress-strain curve per some algorithm, until the desired tolerance is met. Adjustment of the stress-strain curve per iteration may be carried out using an optimization algorithm or some other criterion. Beghini *et al.* [16] obtained Hollomon model parameters for steel, copper and aluminium alloys using an optimization algorithm and the loading portion of the indentation curve. Antunes *et al.* [5], on the other hand, used the method of bisection to fit only the hardening exponent of the Swift law. In the latter two articles the estimated stress-strain curves were compared with curves obtained through conventional testing and the agreement was excellent; for conventional steel and aluminium alloys, the stress-strain curve were found to be within the usual engineering expectation of 10%.

Owing to the low uncertainty of the inverse approach, it has received wide attention. Chung *et al.* [30] have used it to characterize welds and heat-affected zones in automotive steels; Yonezu *et al.* [155] applied it to welds in stainless steels, and Clayton [31] to titanium alloys. In addition to elastic-plastic behavior, Li *et al.* [94] applied damage-mechanics, in an inverse framework, to investigate defect evolution in a stainless steel, and Brammer *et al.* [21] have studied the effect of surface imperfections.

Further developments in sharp indenters have centered around estimation of elasto-plastic properties using the so-called dual indenter approach, wherein instrumented indenters with two different apex angles are used, such as the work done by Chollacoop *et al.* [29].

However, the uniqueness of the stress-strain curve estimated using this approach has been called into question. Theoretical studies have demonstrated the existence of "mystical materials" whose material properties differ, but whose indentation behavior is identical; see articles by Chen *et al.* [27], Cheng *et al.* [28], and Phadikar *et al.* [118] for a discussion of this issue.

Another approach is the cyclic ball indentation test which was developed by Haggag [55] is based on applying progressive loading with partial unloading until the maximum load or depth is reached, then the ball indenter is fully unloaded. The data during each cycle collected and analyzed to determine the stress and strain values. As the load increased the the indentation depth increase as can be seen in the Figure 2.18. The load and plastic depth for each cycle can then be used to estimate true stress as shown in equation (2.12) and true plastic strain as shown in equation (2.13) below:

$$\sigma_t = \frac{4P}{\pi \times \delta \times d_p^2} \tag{2.12}$$

$$\epsilon_P = \frac{0.2 \times d_p}{D} \tag{2.13}$$

where: (σ_t) is the true stress, P is the indentation load, (δ) is the plastic zone parameter, (d_p) is the plastic indentation diameter,(ϵ_p) is the plastic true strain, and D is the diameter of the ball indenter. In order to calculate the (d_p) Haggag [56] suggested the following equation:

$$d_P = [0.5C \times D \times [(h_p)^2 + (d_p/2)^2]/[(h_p)^2 + (d_p/2)^2 - h_p \times D]]^{1/3} \tag{2.14}$$

where h_p is the plastic depth at each cycle as shown in Figure 2.18 and C is a constant can be calculated using the following equation:

$$C = 5.47 \times P(1/E_1 + 1/E_2) \tag{2.15}$$

where P is the applied indentation load, E_1 is the elastic modulus of the indenter, and E_2 is the elastic modulus of the substrate.

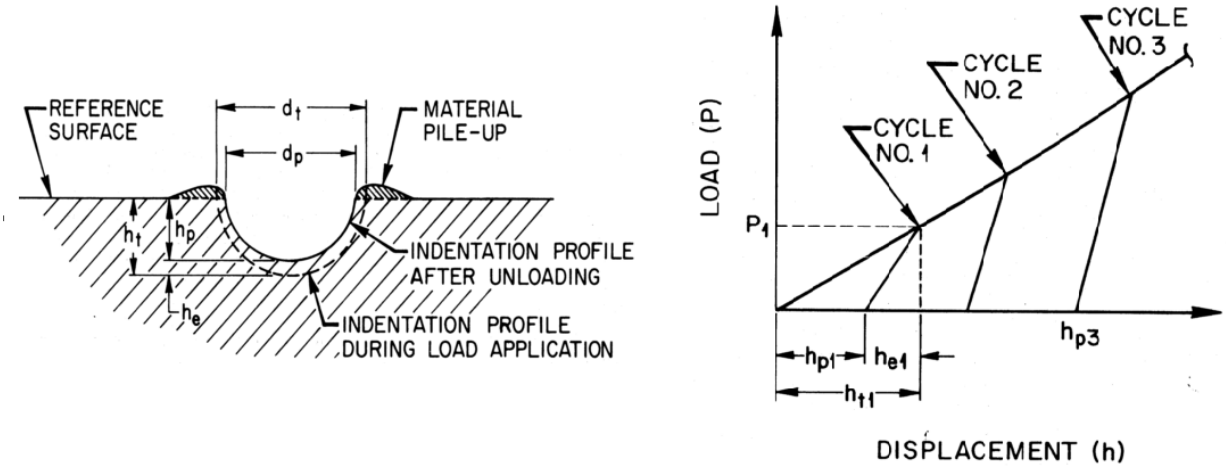

Figure 2.18: Schematic diagram show cyclic indentation process (Reprinted with permisson) [57].

Haggag *et al.* [57] stated that during cyclic indentation process as the indentation depth increase the volume of the material underneath the indenter increased and forced to flow under multi-axial compression unlike the uni-axial tensile test. The yield strength

and the work hardening occur simultaneously and there is no single yield point. Each cycle yield strength increased as the work hardening increase. Therefore, to calculate yield strength using automated ball indentation technique equation 2.16 was proposed. Where A is the material yield strength parameter and can be determined by drawing (P/d_t^2) versus $(d_t/D)^{(m-2)}$, β_m is the material yield slope, and B is the yield strength offset constant. Haggag *et al.* [58] reported a single value for β_m that can be used for all carbon steels (0.2285). To calculate β_m value for any material regression analysis of different yield strength for same material class should be investigated.

$$\sigma_y = \beta_m \times A + B \tag{2.16}$$

As discussed in the previous section the spherical tipped indenters have been analyzed in detail in order to establish stress-strain curves for different materials based on cyclic indentation approach; however, reliable tensile yield strength data could not be derived [4]. During indentation testing on elastic-plastic materials such as steel, the surface area around a spherical indenter will be deformed as the load is applied. When the yield point is exceeded the material will deform plastically and the material around the indenter will start piling-up or sinking-in, making it difficult to determine the true contact area between the indenter and the specimen. Consequently, the apparent stress will be inaccurate since the true area is unknown during plastic deformation, and the actual stress-strain relationship will be difficult to determine [4].

All of the above cited work used either sharp or spherical indenters. There is a third class of indenter geometry, which is the flat indenter, and this geometry has not received the same

attention. The shape of the indentation curve (S-shape) using this geometry affords some advantages. Using the instrumented indenter and finite element computations, Riccardi *et al.* [127] estimated yield of several metals, Lu *et al.* [102] have estimated mechanical properties of a polymer and aluminum alloy, and Hu *et al.* [71] have obtained elastic moduli and yield strength for steel and aluminium alloys. In all of the preceding citations, there was no direct comparison between experimental and computed indentation curves, which is a prelude to the implementation of an inverse approach for the flat indenter geometry.

As discussed earlier, different indenters shapes could be used with the instrumented indentation technique such as conical, spherical, or flat tip indenter. Each indenter geometry has a unique shape that will reflect on the resultant load-displacement curve as shown in Figure 2.19. The advantage of using flat tip or cylindrical indenter is that load-displacement curve is very similar to the stress-strain curve as shown in Figure 2.19, which give an indication when the yield stress occur and since the cross section area of the indenter is constant in the first stage, yield strength could be estimated based on the load and the indenter contact area. However, simulating the indentation process will be quite complex due to the excessive deformation near the indenter edges, which required to use special techniques such as adaptive mesh. That might be the reason many researchers did not provide direct comparison between experimental and computed indentation curves since it will be expensive in terms of simulation time.

Recently, Leroux [93] developed a method to estimate yield strength using flat tip indenters; the method uses the inflection point of the load-displacement curve to estimate yield force and relied on the assumption that the indenter had a cylindrical shape so that the yield strength was simply calculated by dividing the inflection force by area of the

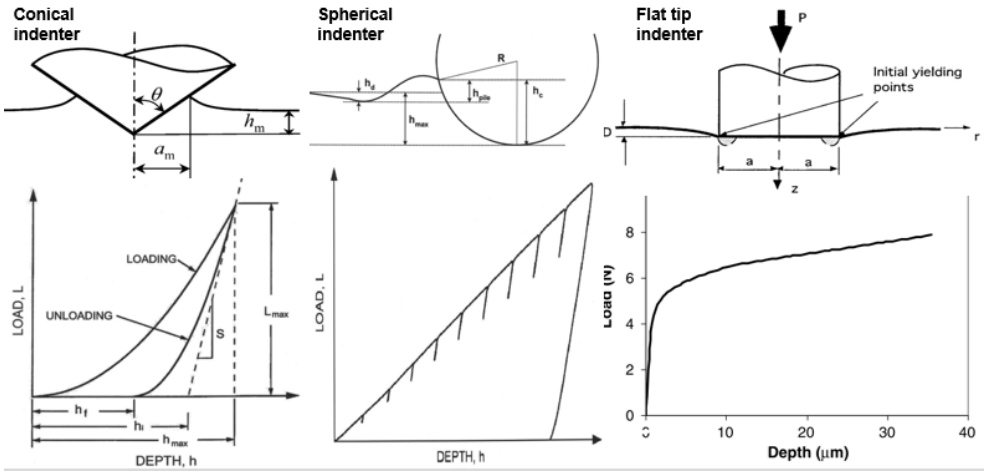

Figure 2.19: Effect of indenter geometry on the load-displacement curve (adapted from) [36, 102, 156].

indenter. Figure 2.20 show the indenter shape on the left side along with experimental load-displacement curve in the right side. The inventor of the machine provide a built in software to detect the inflection point and by using the indenter area the yield strength could be calculated. Leroux claims that *" inflection point of the first derivative, or a change from positive to negative of the second derivative, corresponds to the measured yield point"*. However, Leroux did not provide a physical basis or rationale to support this method. Further research conducted by Hu *et al.* [71] using the same indenter allowed an estimate of the elastic moduli and yield strength for different engineering alloys to be made by means of a combined experimental-computational approach. Despite this, there was no direct comparison between experimental and computed indentation curves presented. The main advantage of using flat tip indenter is that the contact area does not change as drastically as with spherical or Vickers indenters during the indentation process, which allows one to determine yield strength at relatively low magnitudes of plastic deformation.

Therefore, the actual indenter geometry and direct comparison between experimental and numerical indentation studies requires more attention. The effect of idealizing the indenter as perfectly flat tip on the load-displacement curve also will be studied using FEM, in order to understand the contact mechanics and elaborate the agreement between tensile yield strength and indentation yield strength measurements.

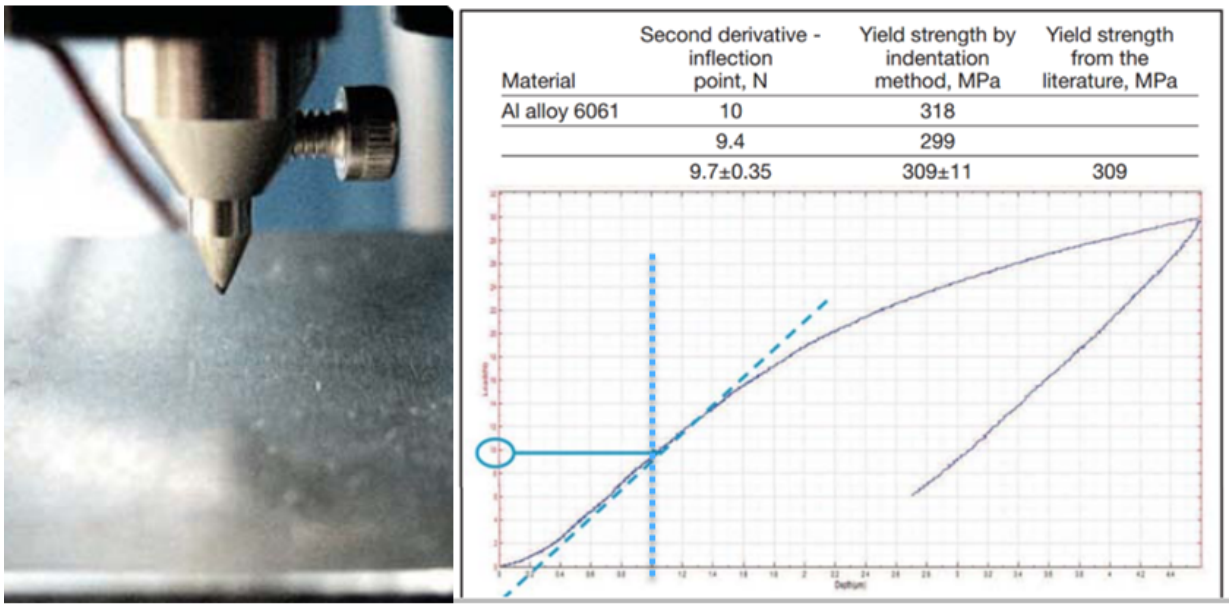

Figure 2.20: Nanovea proposed yield strength method based on inflection point criteria (Reprinted with permisson) [93].

2.9 Specific objectives

This study aims to develop and investigate new techniques that can be used to evaluate the mechanical properties of pipeline steel joints using the state-of-the-art techniques in order to determine how bulk versus local strength overmatching affect the overall transverse

mechanical strength of the joint. The specific research objectives are summarized as follows:

1- Compare weld metal mechanical properties for different X80 pipeline consumables using tensile testing and instrumented indentation techniques. A correlation between the local yield strength measured using DIC tensile testing with the indentation yield strength results will reveal how the minor differences in the welding consumables could effect the local properties of the weld.

2- Employ finite element analysis tools to validate the experimental results that are obtained using indentation in order to characterize the mechanical properties of tested material through an inverse approach. In addition, develop a new and rapid method using instrumented indentation technique to measure yield strength for engineering materials such as pipeline welded joints.

3- Evaluate the strength mismatch for different X80 pipeline joints with different levels of strength mismatching using indentation. In addition, measure the yield strength for different zones across the weld such as reheated weld metal, as-deposited weld metal, CGHAZ, and FGHAZ using the instrumented indentation technique.

Chapter 3

Methodology

This chapter presents the details of the materials, welding joint fabrication process, sample extraction and preparation for microscopy, mechanical testing, and finite element modelling procedures. Since the focus of this study is pipeline steel welds, the methodology will focus on pipeline weld preparation and characterization. Other materials that were investigated in this thesis and specific parameters or sample preparation method will described briefly in each chapter.

3.1 Welding procedure and equipment

Robotic multi-pass Gas Metal Arc Welding (GMAW) was employed to fabricate all the welds presented in this thesis. The welding samples were sectioned from API-X80 24" pipe and the groove prepared as shown in Figure 3.1-a. To calculate the nominal heat input the robotic welder was connected to data acquisition system (DAQ) to collect the voltage

and current signals and measure the average power for each welding pass. To control the cooling rate and remove the moisture from the samples, preheating up to approximately 150 °C was applied prior to the weld and the interpass temperature kept about the same as preheating temperature. To fill the joint six passes were performed as schematically shown in Figure 3.1-b. To avoid incomplete fusion on the sides of the groove the robot was set to perform a sine weave motion during the welding.

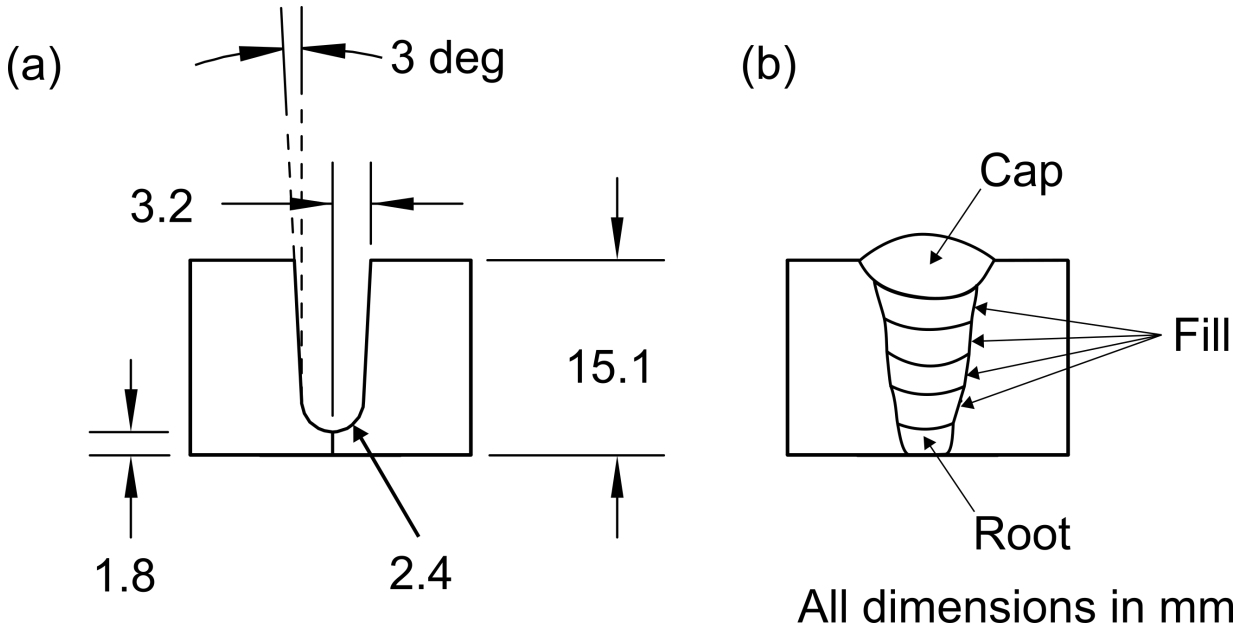

Figure 3.1: schematic diagram shows a)- The groove design b)- The welding passes sequence.

3.2 X-ray inspection and chemical composition analysis

All welded samples were inspected using X-rays to check if any welding defects were present in the fusion zone such as porosity and lack of fusion, which may effect any mechanical testing results later on. The samples that passed the X-ray inspection were processed to perform chemical compositions analysis. Small samples (20mm x 20mm) were cut from base metal and all-weld metal in order to perform the chemical compositions analysis. Chemical analysis was performed according to ASTM standards E1097-12 modified and ASTM E1479-99 (2011). Details of the chemical composition of the samples can be found in the appendix.

3.3 Tensile test and DIC setting

Yield strength is usually determined from traditional tensile testing using a rigid test frame, which elongates the material while measuring force and displacement, thus allowing one to derive a stress-strain curve. The standard uniaxial tensile tests were performed at an initial displacement rate 1 mm/min and at room temperature. Many mechanical properties can be evaluated from a stress-strain curve: yield strength, tensile strength, elastic modulus, uniform elongation, strain hardening exponent, ductility of the material and strain at fracture. In this work, tensile testing was performed according to ASTM E8/E8M [135]. Figure 3.2 shows the locations of the samples that were extracted using wire electro-discharge machining (wire EDM).

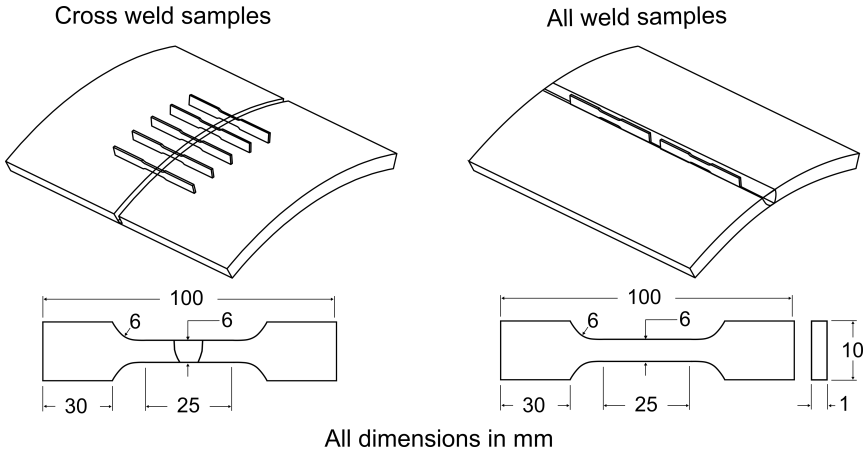

Figure 3.2: schematic diagram shows the extraction location for tensile coupons in transverse and longitudinal directions of the welds.

In order to measure extension within the original gauge length and calculate strain during the tensile test, an extensometer with a specific gauge length is usually used. However, when testing welded structures such that the cross section of the tensile coupon includes different zones BM, WM, and HAZ, the microstructures of these zones are different. Therefore, local and non-contact measurement techniques should be used in this case to map the strain and measure the local properties for each zone. The Digital Image Correlation (DIC) technique that was developed recently can provide full-field strain measurements and map the strain in two and even three dimensions. Hence, the DIC was employed to measure the deformation during tensile testing and calculate the strain.

Digital image correlation (DIC) is a method to measure relative displacement of surface features of a sample while it is being deformed. In order to correlate images with strain values, the specimen surface should have sufficient contrast. This image contrast can be obtained by applying random speckle pattern using white and black spray paint. A

correlation function is used to compare the respective displacement between deformed and un-deformed states. If sufficient points on the surface were displaced, DIC can produce an image to represent the displacement magnitudes in different directions relative to the original state; which can be used to determine the full strain map in the whole area, process that has been automated and developed by Correlated Solutions Inc.[139] In this work, a VIC-3D-DIC system was used as shown in Figure 3.3, and this was used to map strain in three dimensions and generate stress-strain curves for individual zones (WM & HAZ) across the weld joint. To do so, an iso-stress condition was assumed to derive the stress-strain curves for individual zones and determine the yield strength for each zone, as demonstrated in prior studies [98, 126]. The step size and the subset size used in this study was 29 and 7 respectively to reveal strain in different zones without losing any details, for more information about step size and subset size effect on the strain map quality see article by Kashfuddoja *et al.* [85].

Figure 3.3: VIC-3D digital image correlation system that used to map the strain [35].

3.4 Sample preparation for microscopic examination

Small samples were cut from the welded sections using a band saw in order to characterize the microstructure and perform the hardness test in different zones through the weld joint. The samples were hot mounted using conductive bakelite to observe different microstructure under optical mocroscope and/or scanning electron microscope SEM. The samples were prepared according to ASTM standard guide for preparation of metallographic E3-11 [7]. The mounted samples were ground using silica grit paper starting with 120, 240, 320, 400, 600, 1200 sizes; then polished using cloth pad and alumina powder with water

lubricant for 15 minutes. Automated diamond polishing was used to ensure high quality surface finish with different particle size starting by 9 μm, 3 μm, and then 1 μm. After polishing, the samples were etched using 5% Nital solution and rinsed with water followed by alcohol.

3.5 Hardness map and yield strength indentation test

The samples from the cross section of the weld that was prepared for the microstructure evaluation was used to perform the hardness mapping. The Vickers hardness test was performed according to the ASTM-E384 standard. The indentation load was set to be 0.3 kgf and the spacing between the indents was about 3 times the indent diagonal to avoid any interaction of the plastic deformation field. Figure 3.4 below shows approximately 1000 indents performed to cover the cross section of the weld. The Vickers hardness was measured for all the indents automatically and exported to a spreadsheet in order to create a hardness map for the weld cross section. Figure 3.5 illustrates the Nanovea-M1 instrumented indentation machine that was used to measure the yield strength. It should be noted that a 100 μm nearly flat tip diamond indenter was used for all of the pipeline steel welds reported in this work.

This size of the indenter was selected based on the load capacity for this machine, which is 40 N. Due to the variance in the mechanical properties of the investigated materials, different load setting was used for each material. The approach speed was set to 20 μm/min, which corresponds to the speed at which the indenter moves from its starting point towards the sample. Once sample contacts surface, the displacement and force were reset to zero.

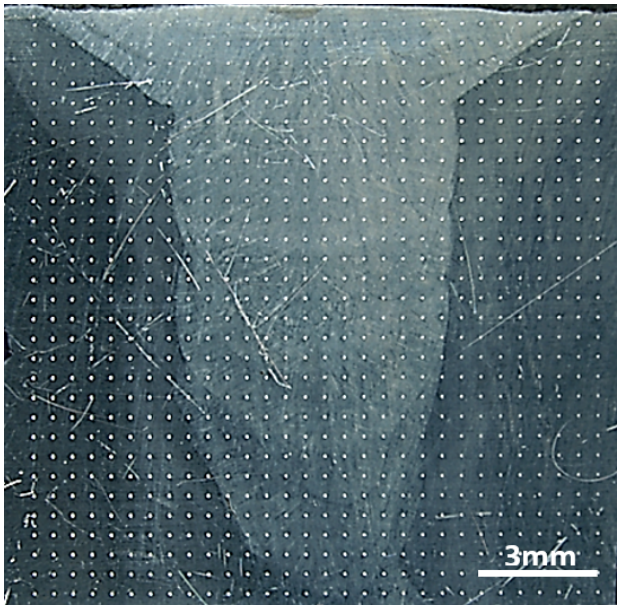

Figure 3.4: Cross section of the weld shows the hardness map pattern.

The instrument moves the indenter towards the sample at a steady rate until the force sensor registers the force specified in the "*ContactLoad*" parameter, which was set to be 30 μN for all tests. Once the contact load parameter is attained, the instrument switches to force control, and then ramps-up the force at the specified loading rate. After reaching the peak load, the load is removed at the same rate. Under idealized vibration isolated conditions, the force and displacement are resolved to within 0.6 mN and 3 nm, respectively.

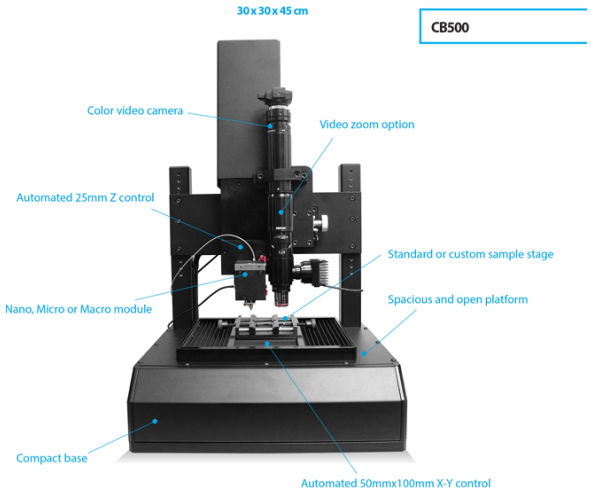

Figure 3.5: The instrumented indentation machine used to estimate yield strength and hardness.

3.6 Finite element modelling procedure

3.6.1 Introduction to ABAQUS software package

In order to simulate the indentation process, the commercial finite element analysis (FEA) software package ABAQUS 6.14 was used. ABAQUS is a powerful simulation program based on finite element method and capable of simulating simple linear problems to most complex non-linear problems. ABAQUS software consists of two main modules ABAQUS/standard and ABAQUS/explicit. The standard solver can be used to simulate wide range of static linear and non-linear problems maintaining the accuracy and reliability of the results. Explicit solver it is suitable for simulating dynamic problems when inertial effects have to be included. The indentation problem and tensile test problem are assumed

to be quasi-static problems in which no rate or time effect will be considered. Therefore, ABAQUS/Standard was used in this work to perform the analysis. The ABAQUS-CAE interface, is used to create the model, submit and monitor the job interactively, and evaluate the results.

The pre-processing stage starts by creating solid model in order to define the mechanical properties, assembly of parts, define the steps, define the interaction between the parts if you have a contact problem, set the loading condition, assign the boundary conditions, generate the mesh, and submit the job. In the post-processing stage the results were visualized and extracted in order to compare it with the experimental results. In this work, millimeter (mm), Newton (N), and MegaPascal (MPa) units are used for length, force, and stress respectively.

3.6.2 Non-linear analysis using ABAQUS

In the indentation problem, owing to the plastic deformation and contact between the indenter and substrate, non-linearity on account of material behavior and contact are present. An incremental approach is adopted by the solver to solve the indentation problem. The user suggests the initial increment size and maximum numbers of increments in the step to find the approximate solution. To converge this also may require ABAQUS to do several iterations to find the acceptable solution, this method called Newton-Raphson method. In addition, after each increment ABAQUS update the stresses and strains then process to new increment. The sum of all increments responses is the approximate solution for the non-linear analysis. When ABAQUS/Standard is used the steps take place over a

period of time; however, this time has no physical meaning.

3.6.3 Material mechanical behavior

Uni-axial tensile tests are routinely used to characterize the mechanical properties of metals and alloys. Most of the metals show linear elastic behavior at low strain values, the relationship between stress (σ) and strain (ϵ) in this region governed by Hooke's law for isotropic linear elastic materials as shown in equation 3.1, where E is the elastic modulus or Young's modulus, which represents the stiffness of the material. Note that the elastic deformation is recoverable when the applied load is removed.

$$\sigma = E \times \epsilon \tag{3.1}$$

When the applied stress is beyond the yield stress value (σ_y), the response is non-linear, which is referred to as plastic behavior. In most metals, yield strength determined by plotting parallel line at 0.2% offset strain [135] or by taking the stress at 0.5% strain in welding standards such as CSA-Z662-15 [6]. To describe the plastic deformation, a power law hardening model Holloman (1944) is often used as expressed in equation 3.2.

$$\begin{cases} \sigma = E \times \epsilon & \text{if}(\epsilon \leq \sigma_y/E), \\ \sigma = K \times \epsilon^n & \text{if}(\epsilon \geq \sigma_y/E) \end{cases} \tag{3.2}$$

However, not all materials can be expressed by the power law model. Therefore, other relationships can be used to describe the hardening behavior of the materials. Most of

these models are based on empirical equations and can be used to describe the material behavior in the plastic region such as: Ludwik model (1909)

$$\sigma_t = \sigma_y + K \times \epsilon^n \tag{3.3}$$

The Swift model (1947) also can be used to describe the hardening behavior for materials that undergo flow stress saturation [112]:

$$\sigma_t = K(\epsilon_s + \epsilon)^n \tag{3.4}$$

where: σ_t and ϵ refer to true stress and true strain respectively and K, n, σ_y, ϵ_s, and E are materials constant can be determined experimentally.

The Voce model (1948) also can be used in the case of flat stress- strain data in the plastic zone since it includes more parameters that can describe the hardening behavior of such a material as shown in equation 3.5

$$\sigma_t = \sigma_y + (\sigma_s - \sigma_y)(1 - \exp(\epsilon \times n)) \tag{3.5}$$

Selecting the hardening model depends on the material behaviour in the plastic regime and the model that gives better agreement with the experimental results should be used. Figure 3.6 shows X80 pipeline stress-strain data were fitted into Ludwik model and Swift model and as can be seen the Swift model showed better fit based on best fit analysis that will be discussed later in Chapter 5.

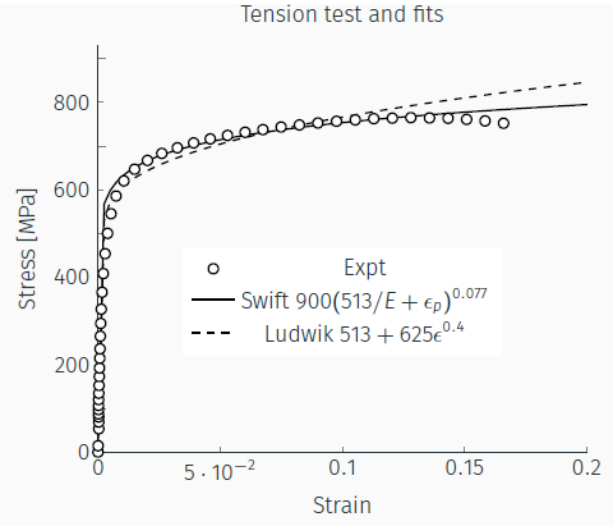

Figure 3.6: Tensile test data for X80 pipeline steel fitted into two different hardening models.

3.6.4 Finite element modelling of indentation

Since the indentation problem has symmetry in terms of loading and geometry it can be considered an axi-symmetric problem. Many studies showed that the indenter is much stiffer than the substrate and can be considered as a rigid body [26, 90]. To verify the validity of this assumption and to check the stiffness or compliance of the machine a study was conducted by assuming the indenter is a deformable body. The results showed that for materials like steel and aluminium the assumption of rigid indenter is valid, more details can be found in Chapter 5.

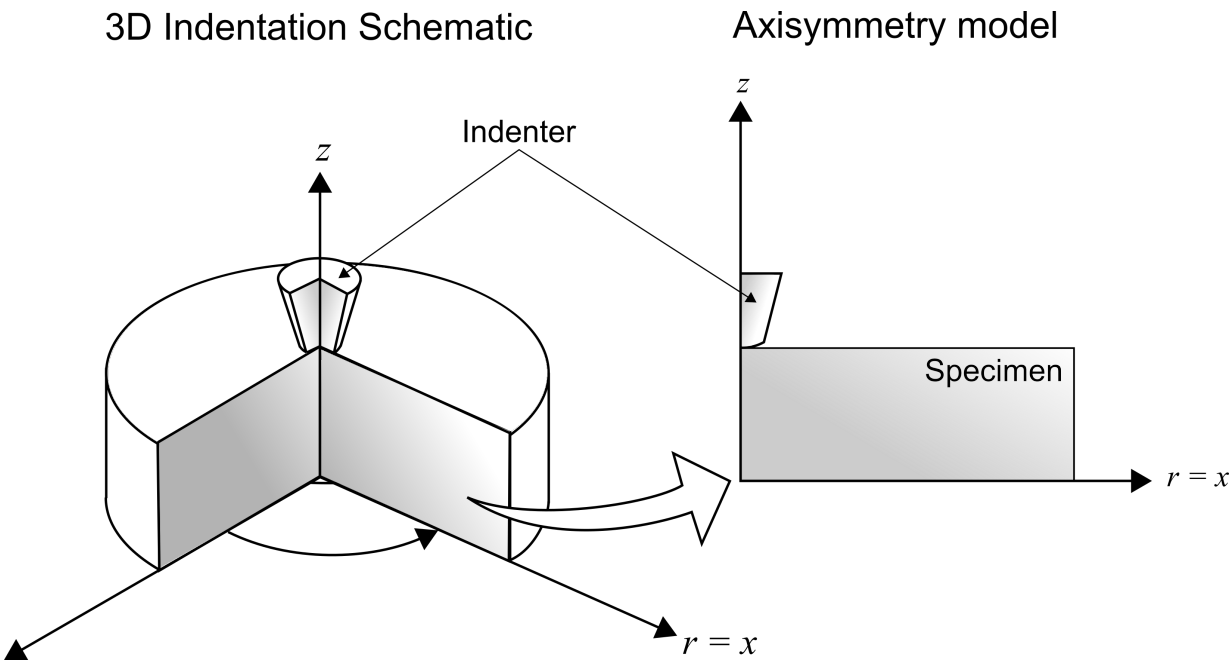

Figure 3.7: schematic diagram for indentation problem.

Material property input

In order to model the elasto-plastic behavior of the tested materials in ABAQUS and check the validity of the assumptions made in the model, there are two ways to input the material behavior (Stress-Strain) relationship. First, input stress and strain data directly as a table, which required performing uni-axial tensile test for the tested materials. Second, the the stress- strain data was fitted to a hardening model and a subroutine was used to run the model. In both cases the elastic Young's modulus and the Poisson's ratio should be given. When the stress-strain data is inputed into the material properties, ABAQUS expects the stress strain data to be entered as true stress and true-plastic strain. The following equations usually used to convert the nominal stress to true stress and nominal strain to

true strain:

$$\begin{cases} \sigma_t = \sigma_{eng} \times (1 + \epsilon_{eng}) & (TrueStress), \\ \epsilon_t = ln(1 + \epsilon_{eng}) & (TrueStrain) \end{cases} \tag{3.6}$$

The true strain (total) should be then converted to plastic strain by subtracting the elastic part, using the following equation:

$$\epsilon_p = \epsilon_t - \sigma_{ty}/E \tag{3.7}$$

where ϵ_p is the plastic part of the true strain.

To verify the model, check the stability of the solution, and study the mesh convergence, tensile test data was used in the first stage. Once the model was verified the UHARD user subroutine was used in ABAQUS/standard to describe the plastic part of the stress strain curve. Constitutive models such as Swift, Voce, or Ludwick as described earlier can be used for this purpose using the UHARD subroutine, which will also play an important role in the iterative inverse approach as will be described in Chapter 5 .

Element type, mesh design and boundary conditions

Four-node axi-symmetric linear quadrilateral elements were used in this study. The element type used in ABAQUS is CAX4R, which is an axi-symmetric, 4-noded, bilinear element. Reduced integration with hourglass control technique was used to prevent excessive mesh distortion. It is also reported that first-order elements work better with contact

problems due to the way the elements calculate consistent nodal loads for a constant pressure [37, 152]. In addition, many solutions are required for the inverse approach, which required efficient simulation time. Therefore, mesh size study was conducted using forward approach by using experimental stress-strain data in the finite element model and compare the FE load-displacement curves to the experimental load-displacement curves. The convergence study showed that 6000 elements are sufficient for the indentation problem under consideration. The mesh was designed to be very fine near the contact area as shown in Figure 3.8. The bottom line is set to be fixed. An axis of symmetry was specified along

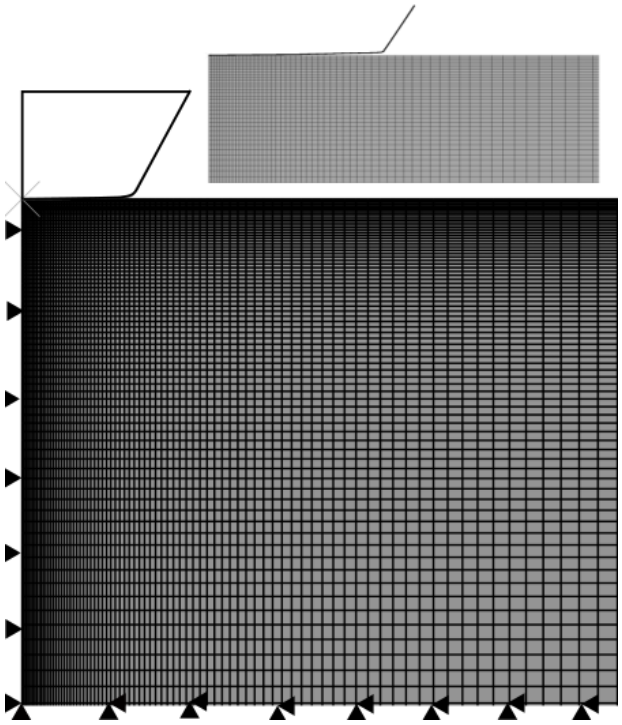

Figure 3.8: Mesh used for the indentation computation and the details of the boundary conditions.

the center line. The right and top edges does not have any constraints and are free to

move as shown in Figure 3.8. The indentation model was carried out using both load and displacement control. There was no difference between the computed indentation response using these two loading methods.

3.7 Inverse approach procedure to estimate elastic-plastic properties for engineering alloys

In the present study, an inverse approach that uses the Efficient Global Optimization (EGO) technique [79] is used to obtain stress-strain curves back from the indentation force-displacement measurements. Since the inverse approach relies on results of several finite element computation, no assumptions about the stress-strain response is required. Indeed, any metal strength model (hardening model) may be used in this scheme. In the first stage the selection of the hardening model will be based on uni-axial tensile test data to develop the inverse approach using a nearly flat-tip indenter geometry. In the inverse approach, the objective function is minimized using efficient global optimization (EGO) algorithm that was developed by Jones *et al.* [79]. The algorithm is used to adjust the parameters of the strength model so as to minimize the error in the difference between the experimental load-displacement curve and the computational load-displacement curve. In order to run the EGO algorithm efficiently, the material parameters that need to be optimized should be given within a certain maximum and minimum bounds. UHARD subroutine should be used in this case in the finite element software to control the material hardening parameters, which are yield strength, hardening coefficient, and hardening exponent [37]. As mentioned

above, any hardening law such as (Swift, Voce, or Ludwik) could be used in the inverse approach. In the absence of stress-strain data, some engineering judgement is necessary to specify the bounds of hardening parameters.

Figure 3.9 shows a flowchart of the inverse approach. As can be seen in the flowchart, an iteration process is involved by comparing the average experimental load-displacement curve to the computational load-displacement curve. To reduce computation time, the objective function ϕ can be set to be within a reasonable tolerance $\pm(5-10\%)$, although a lower value of ϕ can be chosen; however, that might be an expensive in terms of the computation time. The procedure for the inverse approach and the selection of the hardening model will be discussed in Chapter 5 in more detail.

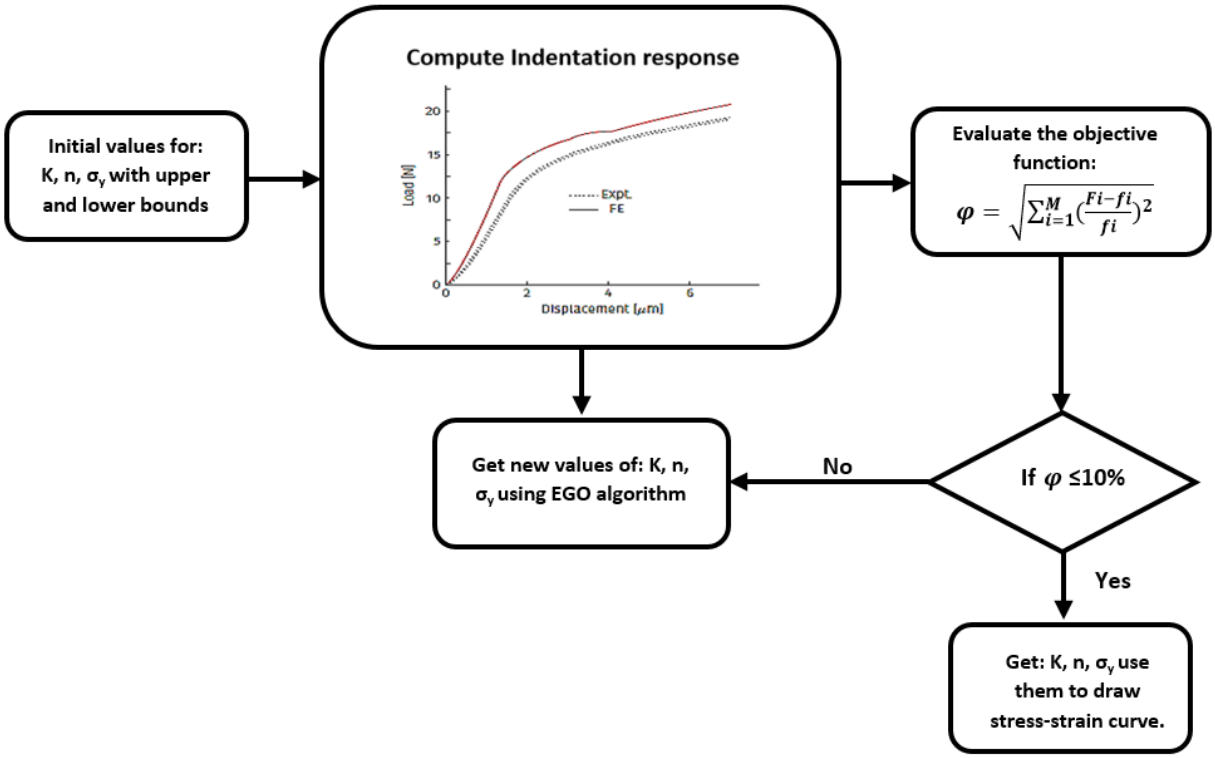

Figure 3.9: Flowchart showing the inverse approach procedure to determine the hardening parameters of the material based on indentation force-displacement response. Note that k, n, and σ_y are the hardening parameters, ϕ is minimization objective function, and F_i and f_i are the computational and experimental indentation forces respectively.

Chapter 4

Characterization of Local Mechanical Properties of X80 Pipeline Welds Using Indentation Technique[1]

4.1 Overview

An instrumented indentation technique is proposed as a method to directly measure the local yield strength distribution in each zone of gas metal arc welds produced in X80 linepipe. The joints were produced with different microstructures and mechanical properties by applying shielding gases with varying Ar/CO_2 ratios of 50 to 15% CO_2 and the addition of a

[1]This chapter is published Manuscript in ASME-International Pipeline Conference on 26 September 2016, available online: https://doi.org/10.1115/IPC2016-64238 , ARH Midawi, Y Kisaka, EBF Santos, AP Gerlich - 2016 11th International Pipeline Conference, Characterization of Local Mechanical Properties of X80 Pipeline Girth Welds Using Advanced Techniques.

pure titanium wire into the weld pool was used to achieve in-situ alloying. The local yield strength distribution for each weld zone was then measured with instrumented indentation. The mapped yield strength distributions measured by instrumented indentation was compared to the hardness distribution. In addition, the yield strength of each zone obtained by instrumented indentation were then compared to tensile test results from Digital Image Correlation (DIC), in order to obtain stress-strain curves for each microstructural zone of the weld. The yield strength results obtained from both techniques are in good agreement, suggesting that instrumented indentation can be useful method to measure the local yield strengths of specific regions in a welded joint.

4.2 Background

Mechanical properties such as yield strength, tensile strength, the strain hardening coefficient and the yield to tensile strength (Y/T) ratio are widely used in pipeline design standards and codes as an acceptance criteria [39, 104]. These mechanical properties are generally obtained following conventional tension test standards; for example, the ASTM-E8 [135] where the standard tensile test specimen is subjected to uniaxial tensile force and then the stress is plotted as a function of strain. The standard tensile test method [135] is widely applied and accepted for testing specimens of homogeneous and inhomogeneous properties. However, care should be taken when testing specimens that have inhomogeneous properties, as in the case of welded joints. Transverse tensile tests are frequently applied as a qualification requirement for a weld procedure, however these tests can not provide information regarding the properties of individual zones, such as weld metal and

heat affected zone.

The properties of the different regions of welded joints vary significantly between and within the different regions of the weld: weld metal (WM), heat affected zone (HAZ) and base metal (BM). For example, for a multipass weld, the properties within the WM and HAZ can be very different for the re-heated zones. To evaluate the tensile properties of a specific zone by standard tensile procedures it is necessary to extract full dogbone specimens from these zones, which is impractical due to technical limitations with their fine scale and geometry. Therefore, a standard tensile test procedure can not reveal the properties of the joint at a micro level, but rather the overall properties.

Many researchers are working to develop alternative techniques to measure locaalized material properties. One promising technique that has been increasingly being used for local characterization of strain is digital image correlation (DIC). Researchers have been using this technique to map and characterize the strain distrbution for the different weld zones [98, 130, 151] as discussed in Chapter 3.

Another technique for local mechanical property measurement is the instrumented cyclic indentation method or sometimes called Automated Ball Indentation (ABI). This technique uses a ball indenter and indents the material at same location with increasing load for each cycle. From the load and displacement data, a number of equations are used to calculate the stress-strain in the plastic regime [57, 77, 86]. For more details see Chapter 2. Although this method is considered a non-destructive method to evaluate mechanical properties, this methodology is based on empirical relationships and curve fitting or data regression [152]. In addition, this method does not have the capability to provide

yield strength value because it evaluates the response in the plastic deformation regime. Furthermore, since a ball indenter is used, it is not suitable for the application of low loads, which is necessary to extract of yield strength information. Meanwhile, other welding research centers such as The Welding Institute (TWI) in the UK published call for proposals aiming to develop and standardize an indentation technique to be used to measure the local mechanical properties of welded joints and predict the full stress-strain behavior based on the inverse approach [136], which further points to the need for such testing methods to be developed and standardized.

Recently, Leroux [93] reported the development of a instrumented indentation testing method for measuring yield strength. In this method, a flat-tip indenter was used to estimate yield strength from the indentation curve. Hu *et al.* [71] used this method to measure yield strength for different engineering alloys and used a numerical model to validate the experimental results. However, to the author's best knowledge, this method has not being applied yet to characterize the yield strength of the different zones of a welded joint. The aim of this study is to apply and validate the new indentation technique that uses flat tip indenter as a method to measure the local yield strength distribution for girth welds of X80 pipeline steels. Three different zones are evaluated: weld metal, heat affected zone and base metal. To validate the yield strength results obtained by the indentation method, they were compared to yield strength obtained by DIC technique and correlated with hardness profiles.

4.3 Experimental procedure

4.3.1 Welding

Two weld samples were produced using a robotic GMA welder equipped with a Lincoln Power Wave 455M power supply. Curved sections of API 5L-X80 steel pipe were used to produce welded joints with different weld metal microstructure, and consequently mechanical properties. The welds were made with two different welding wires and two different shielding gases. The specimens were designated TP-4 and TP-8. TP-4 was welded using a wire consumable, which contains molybdenum and titanium, with a 50% Ar-50%CO_2 shielding gas mixture. On the other hand, the specimen TP-8 was produced with a wire, which has no titanium, with 85% Ar-15%CO_2 shielding gas mixture. For TP-8, in-situ alloying of the root pass was performed by the addition of a thin titanium wire. The final chemistries of the weld metals are shown in Table 4.1. To produce the welded joints, welding using the constant voltage (CV) mode was performed with parameters as shown in Table 4.2. As noted in Table 4.2, the voltage for welds using Ar-50% CO_2 needed to be increased by approximately 1.5 V in order to maintain a similar arc length compared to the welds using Ar-15% CO_2. The welded joints were produced in the flat position in a butt joint configuration with U-shape grooves having a bevel angle of 3° and a 1.8 mm root face, using a 1/8 circumferential pipe section cut from a 24" pipe diameter as shown in Figure 4.1. Preheat and interpass temperature were initially set and maintained to be approximately 150 °C. Figure 4.2 shows the welding set-up of how the pipe sections were clamped together during welding.

Table 4.1: Chemical composition of deposited weld metal.

Element (wt%)	Specimen	
	TP-4	TP-8
C	0.057	0.085
Si	0.45	0.52
Mn	1.57	1.73
Mo	0.57	0.52
Cu	0.18	0.32
Ni	0.05	0.07
Cr	0.02	0.02
Al	<0.01	<0.01
Ti	0.03	0.02
O	0.034	0.020
N	0.0033	0.0035
Ceq	0.2256	0.2723

After welding, standard metallography techniques were used to investigate the microstructure of the joint. Then hardness and indentation testing were performed. The cross weld tensile samples were extracted as explained in the methodology Chapter 3.

Table 4.2: Welding parameters used for each pass in X80 welds.

	Voltage (V)		Wire feed speed	Current	Travel speed	Heat input
	TP 4	TP 8	(m/min)	(A)	(cm/min)	(kJ/cm)
Root pass	27.5	26.0	9.5	300	120	3.5
Hot pass	27.5	26.0	8.5	280	60	6.3
Filler pass 1	27.5	26.0	8.5	280	60	6.3
Filler pass 2	27.5	26.0	8.5	280	60	6.3
Filler pass 3	27.5	26.0	8.5	280	60	6.3
Cap pass	24.5	23.0	6.0	220	30	10.1

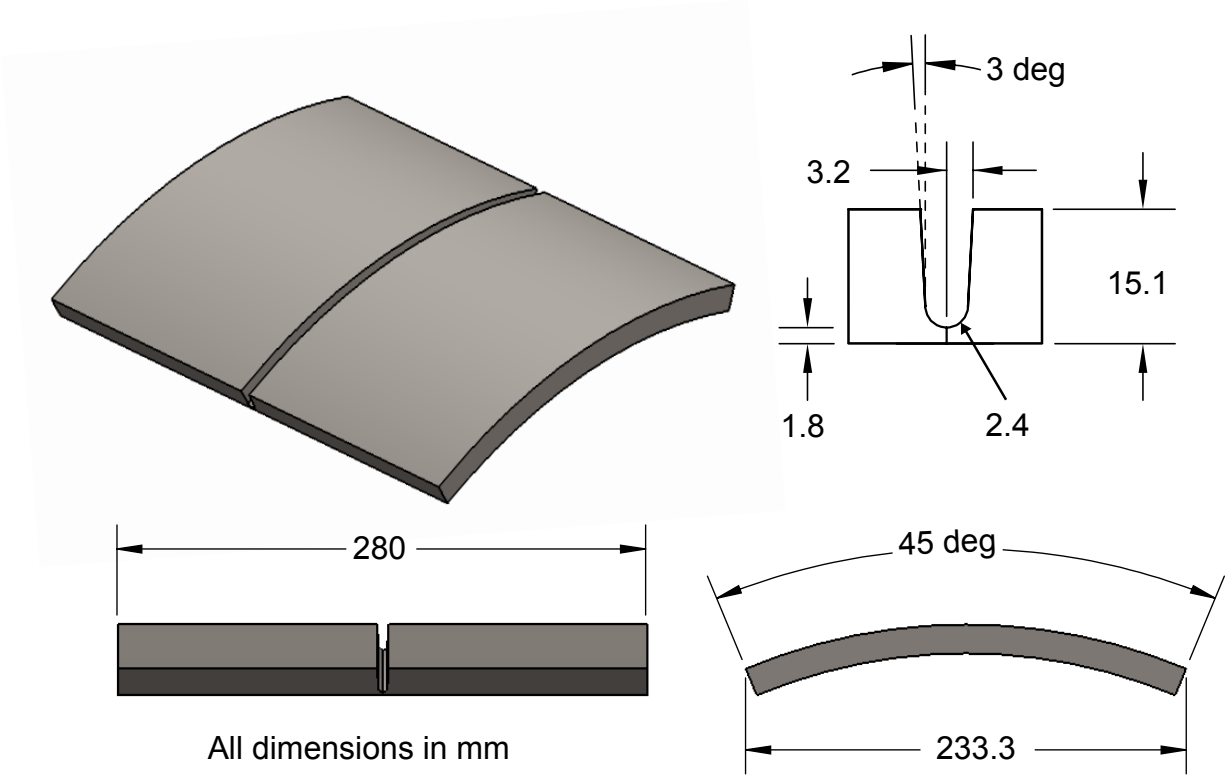

Figure 4.1: Joint configuration and groove dimensions.

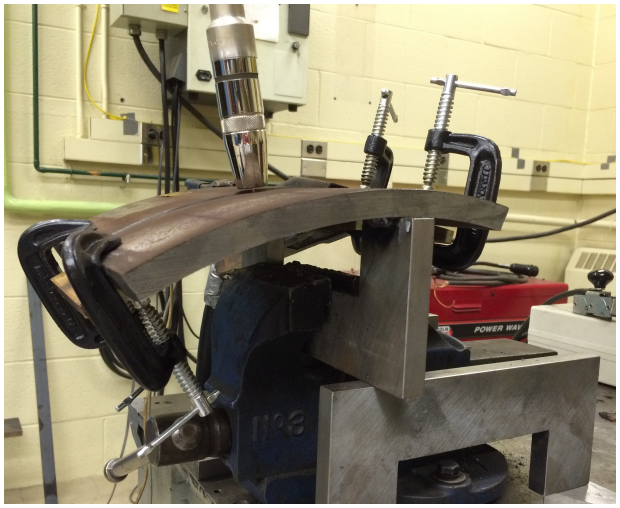

Figure 4.2: Detail of welding set-up.

4.3.2 Indentation testing

Conventional hardness testing was performed across the welded joint using Vickers hardness indenter with a 0.3 kg load and a dwell time of 15 s. The distance between consecutive indents was approximately 400 μm. The instrumented indentation machine used to measure the yield strength was a Nanovea microhardness tester (Model M1). The region where instrumented indentation measurements were performed corresponds to the inside of the dashed rectangle shown on Figure 4.3. This area is 7.6 mm wide by 1.6 mm high. The spacing between the indentations was set to be 400 μm in order to avoid any interaction between strain fields or hardening effects. This provided a total of 100 indents for each sample. It should be pointed out that the sample should be prepared per metallographic standard practices with final polishing to 1 μm diamond paste to achieve a flat surface in order to get clear load-displacement curves. Since the base material is API-5L-X80 high

strength steel with a minimum yield strength of 550 MPa. A 100 μm indenter was used to ensure the loads during indentation did not exceed the force capacity of the indentation machine. The other indentations parameters were: maximum load of 20 N, loading rate of 40 N/min, contact load of 20 μN and approaching speed of 3 $\mu m/min$.

4.3.3 DIC strain mapping during tensile testing

Tensile tests were performed using a Tinius Olsen machine (Model H10KT) equipped with DIC apparatus from Correlated Solutions Inc., model HSI-VIC 3D. Sub-size coupons were machined from the mid-thickness area of the joint using electrical discharge machining (EDM) technique as explained in the methodology Chapter 3. Figure 4.4 (a) shows tensile coupon prepared for tensile test in order to identify the weld regions and Figure 4.4 (b) is an image of the same sample from the other side shows the speckle pattern.

For each welding condition, three samples were prepared and tested to ensure repeatability. The DIC technique was used to produce a strain map for individual zones across the welded joint. At least three points were averaged in the WM, HAZ and base metal regions and used to construct the stress-strain curves for individual zones. The assumption of iso-stress condition was used to build stress-strain curve for each zone as described in prior work [126, 151]. It should be noted that based on this iso-stress assumption, the exact stress can not be accurately described past the yield, since the sample cross-section changes, particularly near the ultimate tensile stress.

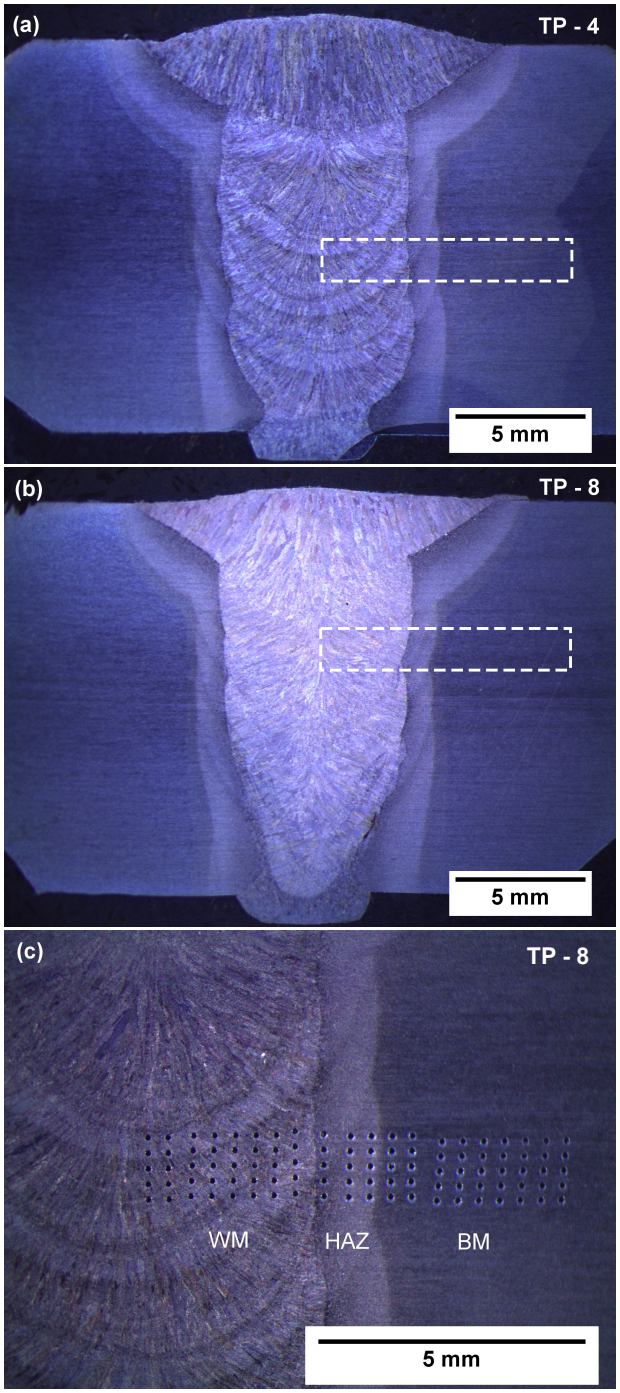

Figure 4.3: Macrographs show the cross section of the weld and dashed boxes show where the indentations were performed (a) TP-4 sample, (b) TP-8 sample, and (c) a close look show the indentations in each zone.

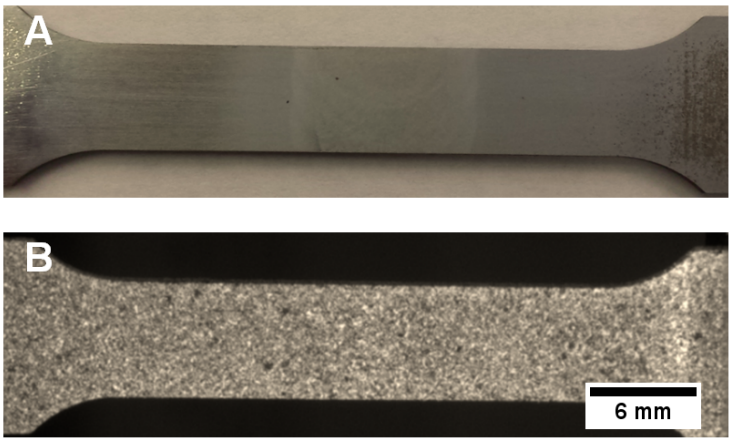

Figure 4.4: Tensile specimen a- Showing the weld regions and b- Speckle pattern prepared for the DIC.

4.4 Results and discussion

4.4.1 Microstructure

The characteristic microstructure of the weld metal for both specimens are shown in Figure 4.5. Acicular ferrite is the dominant microstructure for both welding conditions, however, specimen TP-8 presented a finer and more homogeneous structure, as shown in Figure 4.5 (b). It has been widely reported that titanium, when combined with other elements such as oxygen and nitrogen, can act as nucleation sites for acicular ferrite [11, 17, 18], however it can be noted that TP-4 specimen, contains slightly a higher amount of grain boundary ferrite, see Figure 4.5 (a). As reported by Terashima and Bhadeshia [144] this can be attributed to a higher amount of oxygen in the shielding gas used for sample TP-4, which leads to an increase of grain boundary ferrite. It was experimentally verified that the weld metal for TP-4 contains higher amount of oxygen as shown in Table 4.1.

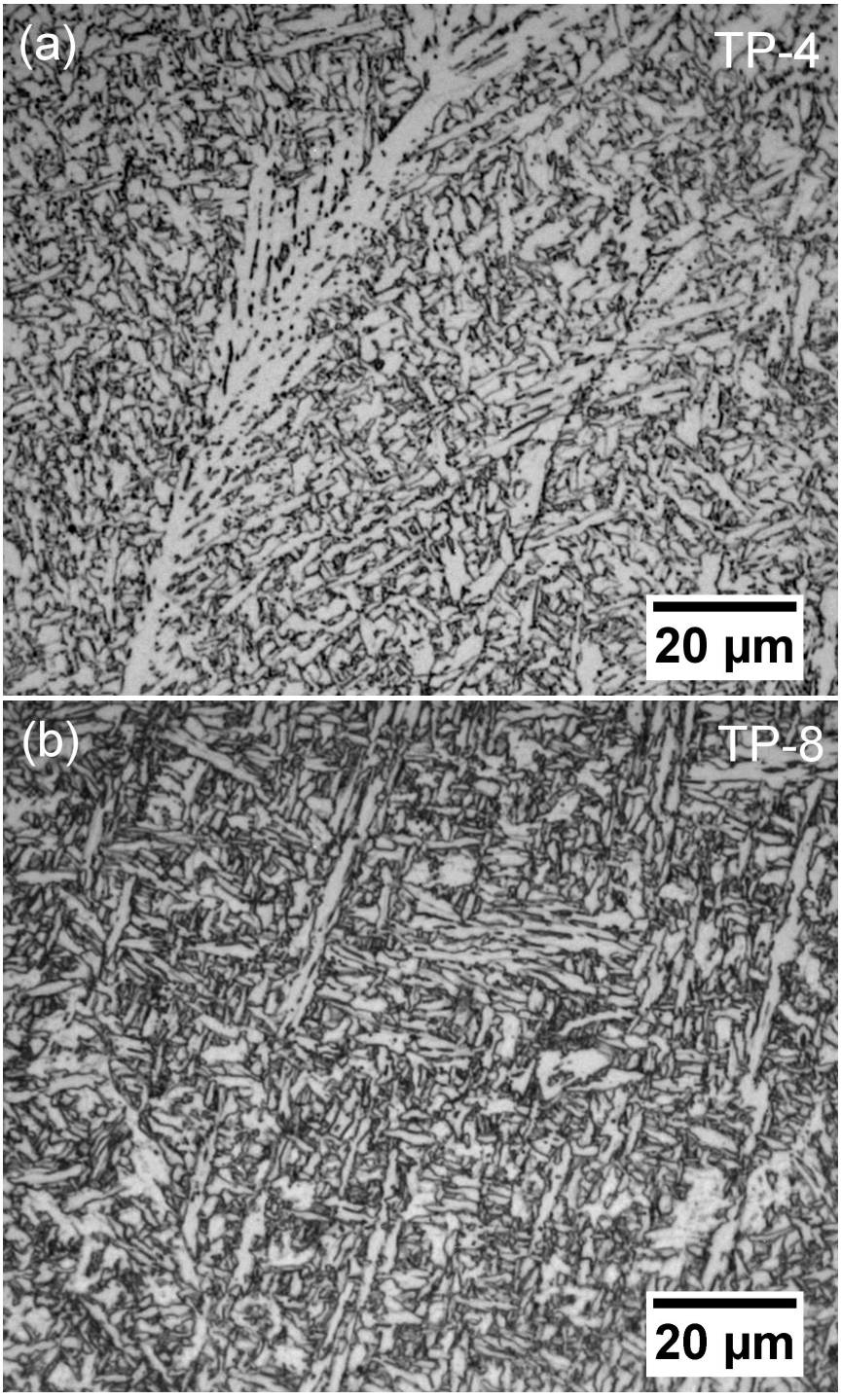

Figure 4.5: As deposited weld metal microstructure a) TP-4 and b) TP-8.

4.4.2 Hardness test

Microhardness was mapped for the entire weld cross-section as shown on Figure 4.6. It can be seen from the microhardness map that TP-8 welds overmatch the hardness values for base metal, while TP-4 welds can be considered as even match condition. For both weld conditions, the average hardness for the base metal and heat affected zone are nearly the same, 225±10 $HV_{0.3}$ and 200±15 $HV_{0.3}$ respectively.

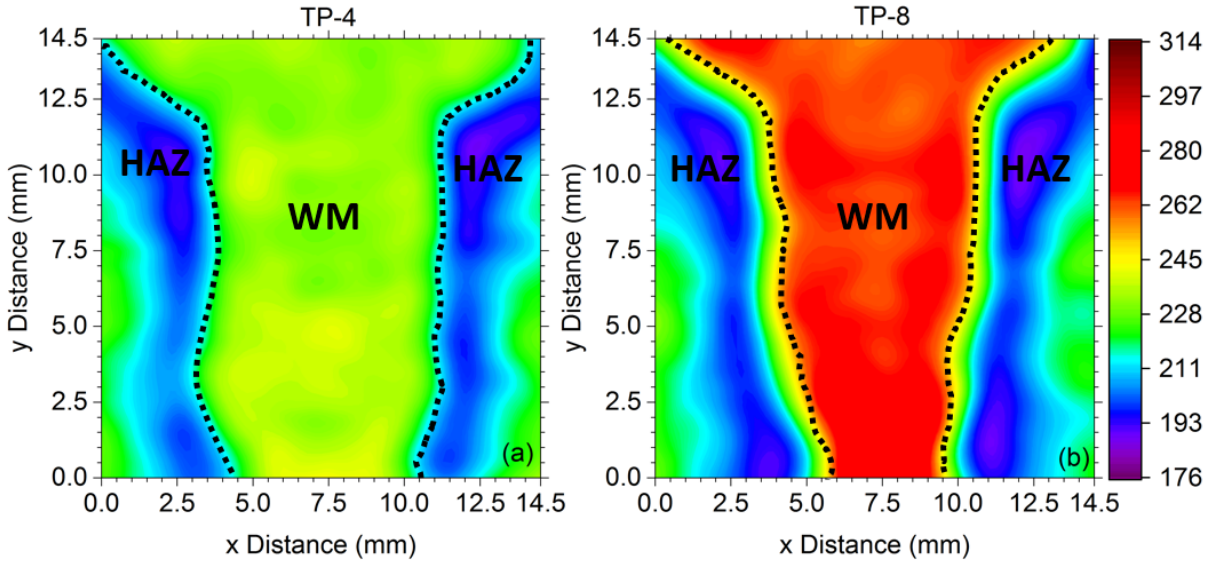

Figure 4.6: The microhardness maps for the welded joints showed the difference in the hardness between the weld metals.

The similar hardness was observed in the HAZ for both samples is also reasonable since the heat input of both conditions was similar. As for the weld metal, sample TP-8 exhibited higher hardness values, 270±14 $HV_{0.3}$ compared to 233±9 $HV_{0.3}$ for TP-4. This is explained by the finer and more homogeneous acicular ferrite exhibited in Figure 4.5b. In addition, the difference in the hardness can be attributed to the difference in the carbon

equivalent between both condition. The TP-8 sample showed higher carbon equivalent compared to TP-4 sample as shown in Table 4.1 and this is largely owing to the presence of C, Mn, and Cu.

4.4.3 Yield strength indentation test

Figure 4.7 shows typical load-displacement curves for individual zones of the weld joint. These curves are used by the Nanovea software to extract the yield strength value for each test. The load that correspond to yield is equivalent to the inflection point of the load-displacement curve [93]. As can be inferred from the curves the response and hardening behaviour for each zone is different, which is consistent to difference in microstructure for these distinct zones. It was observed that within the weld metal and heat affected zone, the load-displacement response varied from point to point. This is because of the multiple thermal cycles during the multi pass welding process, which is leads to heterogeneity in the microstructure of these zones. Figure 4.8 shows the comparison of yield strength and hardness. The bottom part of Figure 4.8 (a) and (b) shows the yield strength map obtained from the indentation technique for the region shown in Figure 4.3.

It can be noted that the lower yield strength was recorded in the HAZ for both conditions. On the upper portion of Figure 4.8 (a) and (b) the average yield strength across the weld is plotted and compared with the hardness profile. From Table 4.3 it can be noted that in both samples, the weld metal had the highest yield strength. The weld metal in specimen TP-8 exhibited higher values of around 655±22 MPa while specimen TP-4 a lower value of 627 ±10 MPa. The yield strengths for the HAZ of both welds was nearly the

same; 605±6 MPa for TP-4 and 599±5 MPa for TP-8. Note that as shown in Figure 4.8 the average yield strength has the same trend presented by the hardness values, which suggests the indentation technique is promising for evaluation of yield strength. In addition, as shown in the yield strength map, this technique can also be used even to distinguish strength in different weld metal zones: as deposited and reheated. The latter are because of the thermal cycles during the multi-pass welding process.

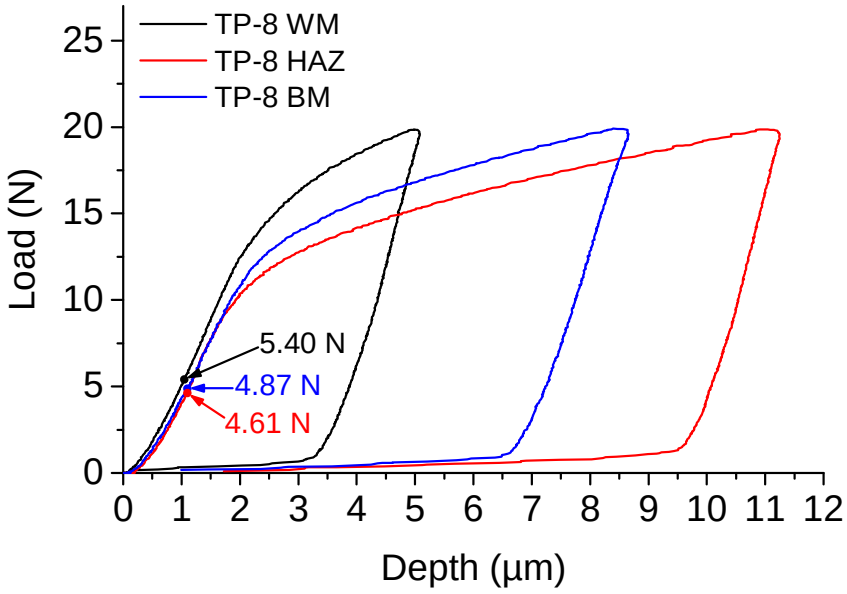

Figure 4.7: Average indentation load-displacement curves for weld metal, heat affected zone, and BM for TP-8 weld. The arrows show the force at the inflection point that picked up automatically by the machine software.

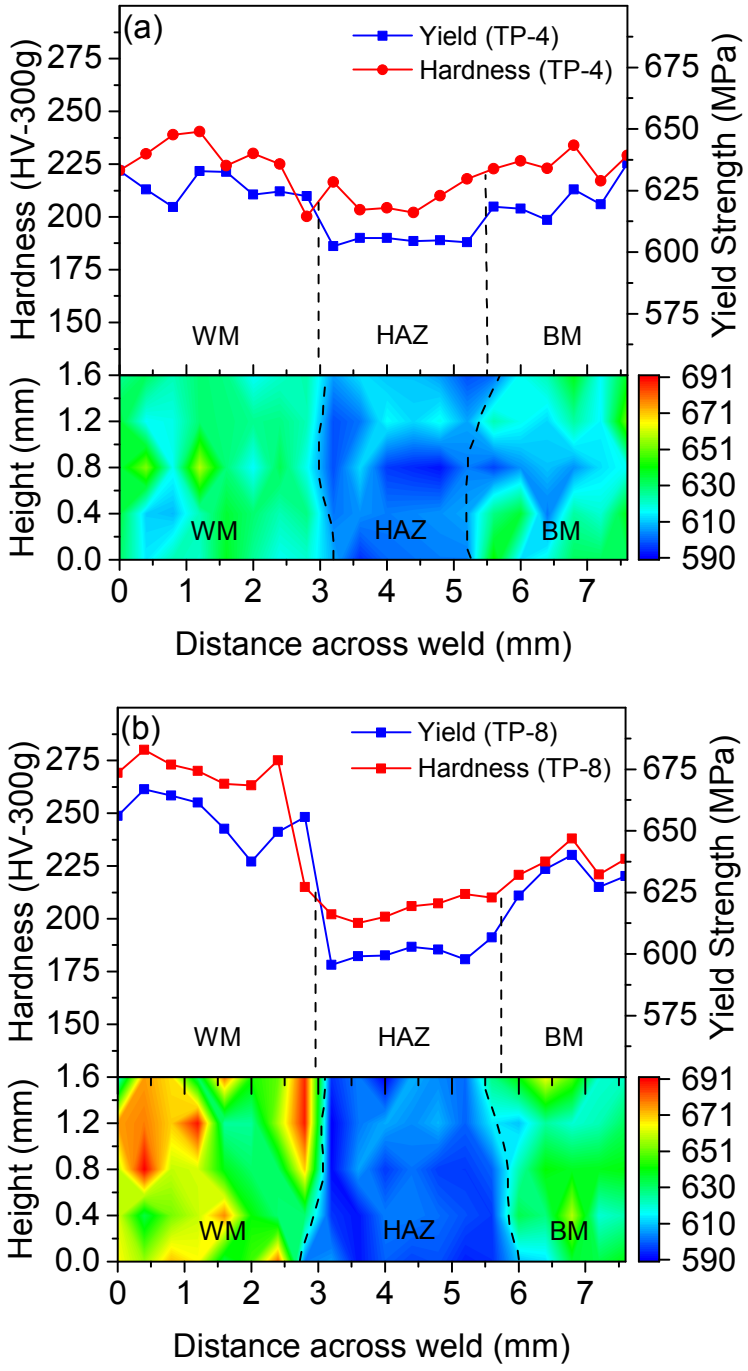

Figure 4.8: Yield strength map for each welding condition at the bottom along with hardness and yield strength profile in same zone at the top (a) TP-4, (b) TP-8.

4.4.4 DIC tensile test

From the tensile test it was verified that all the failure occurred in the HAZ, for both TP-4 and TP-8. Figure 4.9 depicts the local stress-strain curves for the different weld regions. The TP-4 weld metal yield strength obtained by DIC was determined to be 613±5 MPa compared to 627±10 MPa from indentation, while specimen TP-8 sample exhibited higher strength with an average 658±13 MPa compared to 655±22 MPa from indentation. Similarly to the indentation technique, the DIC results also indicated that the minimum yield strength was measured in the HAZ for both conditions.

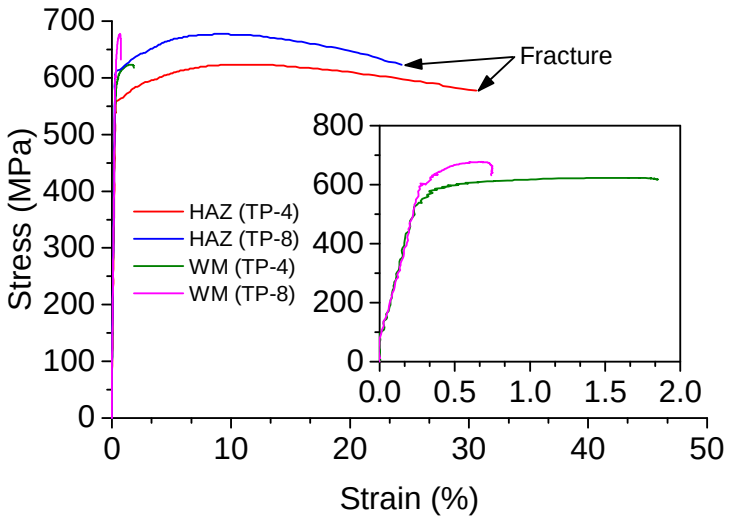

Figure 4.9: DIC stress-strain curves for weld metal and heat affected zone with elastic behaviour shown in inset.

DIC measurements indicate that the yield strength for the HAZ was approximately 580±15 MPa for TP-4 specimen, and 589±14 MPa for TP-8, respectively; see Table 4.3. This measurement, in comparison to the indentation technique, has a maximum error of

8.1%. This difference might be attributed to the as deposited/reheated area ratio in the weld metal, and ICGHAZ/CGHAZ in the HAZ, which will be considered as a future work, and that can lead to more accurate results.

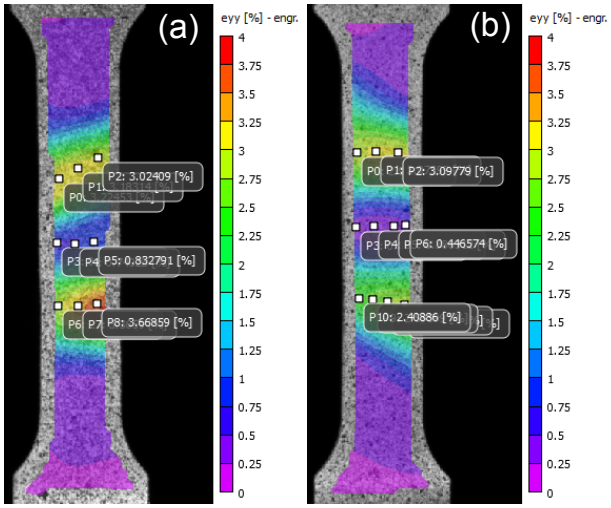

Figure 4.10: DIC local strain mapping at global strain value of 1.5% (A) TP-4 (B) TP-8.

From Figure 4.10 it was noted that for the same global strain of around 1.5%, the average strain of the TP-8 WM was 0.45% compared to 0.9% for the TP-4 WM. Therefore, in order to achieve the same global strain of the HAZ of TP-8 should accommodate a higher amount of stress.

Table 4.3: Comparison of yield strength for the different zones measured by indentation technique (Ind.) and tensile test (DIC).

Specimen	Weld Metal			Heat Affected Zone		
	Ind.(MPa)	DIC (MPa)	Error (%)	Ind. MPa)	DIC MPa)	Error (%)
TP-4	627±10	613±5	4.8%	605±6	580±15	8.1%
TP-8	655±22	658±13	5.7%	599±5	589±14	5.0%

The 3D waterfall graphs of the two weld as shown in Figure 4.11, where it can be noticed that the total amount of strain accommodated at the weld metal for the TP-8 weld is lower than that for TP-4 weld, which is therefore consistent with the higher yield strength of the weld metal in sample TP-8. The DIC 3D strain-time plot also shows how the strain accumulated over the time during tensile test, which could be used to investigate the effect of strength mismatch on strain capacity of each zone in strain based design approach. Comparing the 3D plots of the local strain accumulated in the HAZ in both conditions, it is clear the lower strength condition TP-4 HAZ showed higher strain compared to TP-8.

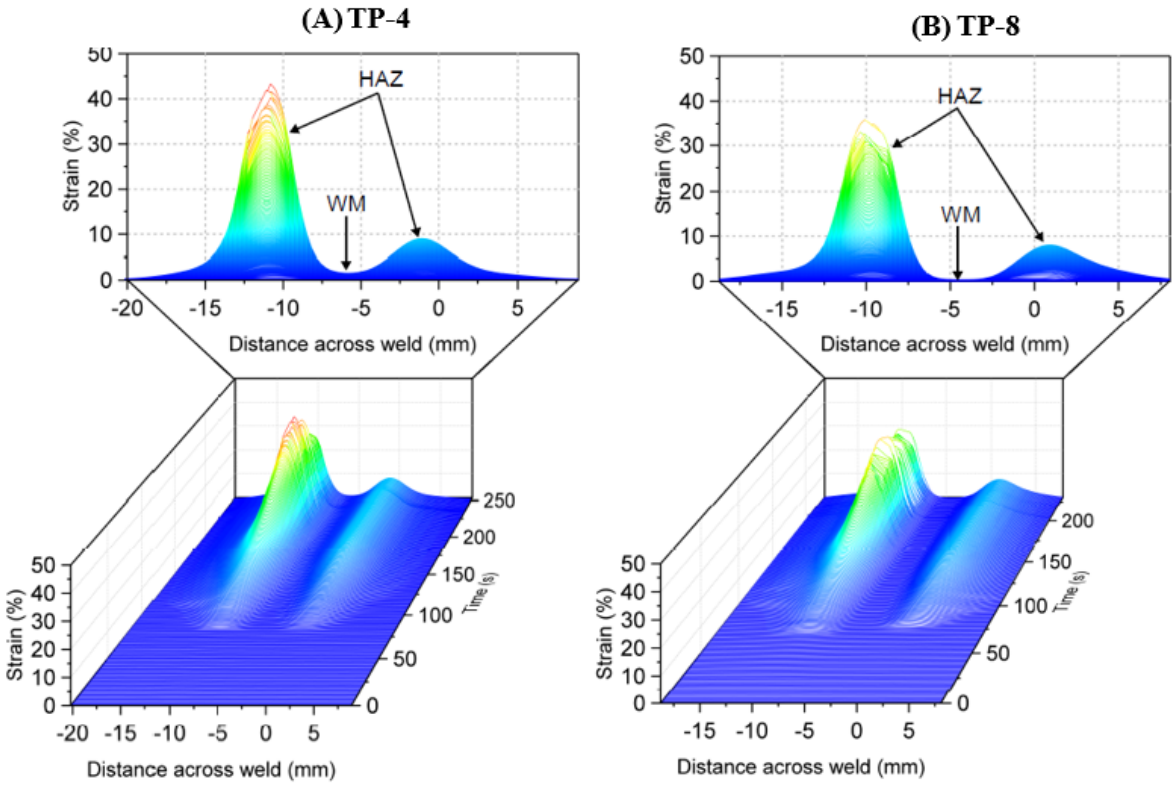

Figure 4.11: DIC strain mapping over the time for (A) TP-4 (B) TP-8.

4.5 Summary/ Remarks

The local yield strength of two X80 pipeline steel weld joints were characterized by employing indentation technique and digital image correlation (DIC). The microhardness map was also obtained. These strength measurements were found to be consistent with transverse hardness profiles. The agreement between instrumented indentation and DIC measurements suggest that the indentation method may be potentially used as a tool for evaluating overmatching in the welded structures without the need for extraction and machining of tensile specimens. The combined methods also provide useful information regarding the differences in mechanical performance between the weld metal, HAZ, and base metal. These differences may also be useful in correlating to fracture toughness in future studies.

However, the indentation technique in this study was used as provided by the inventor to detect the yield force and calculate the yield strength based on inflection point method using built in software. Therefore, the following chapter will focus on understanding the theory behind this technique and the mechanics of the contact using the flat tip intender geometry. FE modelling will be employed to verify the obtained yield strength results and to explain the mechanics of contact. The validation of this technique could lead to its widespread application for measuring yield strength directly for weld qualification purposes, and possibly as a quality control measure in the field, which would streamline testing since indentation tests can be automated and are simpler than tensile tests. It also provides far more detailed local property measurements, which can be used for numerical modelling of the bulk strain of a joint during strain based design.

Chapter 5

Elastic-Plastic Property Evaluation Using A Nearly Flat Instrumented Indenter[1]

5.1 Overview

A 100-μm diameter, nearly flat, instrumented, indenter is used to indent AA-6463 aluminium and X80 pipeline steel. In contrast to sharp and spherical indenters, a rising load-displacement response is followed by a concave - downwards response during indentation. The substrate materials are characterized using tension and compression tests. Yield

[1]This chapter is published Manuscript in International Journal of Solids and Structures on 29 September 2016,available online:http://dx.doi.org/10.1016/j.ijsolstr.2016.09.036, A.R.H. Midawi,C.H.M. Simha, M.A. Gesing, A. Gerlich, Elastic-plastic property evaluation using a nearly flat instrumented indenter.

strengths measured under compression are within +/- 10% of the tensile values thereby providing partial support for assuming symmetric tension-compression response. Based on imaging of the actual indenter using a Scanning Electron Microscope, a model of the indenter that accounts for the curved contact profile was created, assumed to be rigid in finite element simulations. In the simulations, tensile yield strength and flow properties, obtained by tensile testing are used to describe the behavior of the substrate and good agreement with measured indentation force-displacement curves was obtained when the exact shape of the indenter was used. The agreement is poor when the contact profile of the indenter was idealized as flat. In the context of the inverse approach, using the Efficient Global Optimization technique, fits to the stress-strain curves of both of the alloys were obtained, and again the curvature of the indenter contact profile is found to be crucial. This work sets the stage for a broader deployment of the inverse approach to map the stress-strain response of heterogeneous microstructures such as welds.

5.2 Background

Indentation tests with spherical (Brinell) and sharp (Berkovich or Vickers) indenters are widely used to measure the hardness and characterize mechanical properties of engineering materials. Typically, for metals, the properties are restricted to tensile strength and the conversion of hardness to strength is done using empirical formulas, see monograph by Tabor [140]. However, when indentation testing is augmented with continuous measurement of force and displacement, additional mechanical properties such as elastic modulus, and yield may be estimated; see, for instance, the article by Bhattacharya *et al.* [20]. In the

present work, a micron-sized indenter is used in an instrumented machine to indent typical aluminum and steel alloys, and a computational technique for the estimation of the yield strength and flow curve is proposed. This provides a basis for estimation of the entire stress-strain curve through instrumented indentation.

The nearly flat-tip indenter in an instrumented machine was used to study the indentation response of two conventional engineering alloys. The intended application for the techniques developed in this work is the mapping of stress-strain curves in welds and adjacent regions. Using stress-strain curves obtained from conventional methods, the indentation process is modelled using finite element computation; furthermore, an inverse approach that uses the technique of Efficient Global Optimization (EGO) is used to obtain stress-strain curves from the indentation force-displacement measurements. As the inverse approach relies on iterative finite element computations no assumptions about the indentation response is required. Indeed, any metal strength model (hardening model) may be used in this scheme. Of course, the choice of the hardening model based on only the indentation response is not obvious and is suggested as a point for further investigation. Another potential criticism of stress-strain curves obtained from indentation curves is that the measurement is carried out under compressive stress states, whilst, in practice, stress-strain curves in tension are required. Similarity of tensile and compressive response is often tacitly assumed. This assumption is partially assessed in this work by comparing tensile stress-strain curves used to model the indentation test with compressive stress-strain curves.

5.3 Materials and sample preparation

Two alloys were assessed in this work AA-6463 a wrought aluminum-magnesium-silicon alloy of 1.2-mm thickness and an X80 high-strength line pipe grade steel of 15-mm thickness. In the case of the AA-6463, the indentation direction was perpendicular to the rolling direction and in the case of the X80 steel the indentation direction was parallel to the long axis of the pipe. Orientation dependence (with respect to rolling direction) of indentation curves has been observed but not addressed in the present work. Samples were prepared per the ASTM procedure for metallographic sample preparation E3-11 [7]. Three samples for each material were cut with dimensions of 2 cm by 2 cm and molded with hot mounting bakelite. The specimens were ground and polished according to the ASTM standard as explained in the methodology Chapter 3. The specimens were then cleaned by water and alcohol and etched to identify different phases in the microstructure. The optical microscope in the indentation tester was used to ensure the quality of the surface preparation.

5.4 Indentation procedure

Microhardness instrumented indentation tester (Nanovea-M1) was used to perform indentations tests. Semi-flat diamond tip with 100 μm diameter was employed to carry out the indentation tests for both the AA-6463 and X80 pipeline steel. The load capacity for this machine is 40 N during measurement. Due to the variance in the mechanical properties of the tested materials, different load settings were used for each material as shown in Table

5.1. The shape of the indenter was assessed by obtaining Scanning Electron Microscope (SEM) images of the indenter. Making reference to Figure 5.1, the indenter tip is not flat and cannot be idealized as a flat surface. The reason the shape of the indenter tip is crucial will become clear in the section on finite element computations. Hereafter, the actual profile is referred to as curved, and the ideal flat case is referred to as idealized.

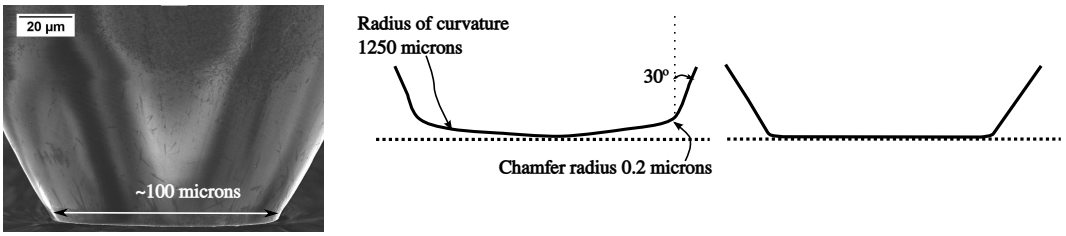

Figure 5.1: Scanning Electron Microscope image of the indenter, revealing it is not perfectly flat. The surface profile digitized from the SEM image as shown in the middle, and contrasted with ideal flat profile on the right.

Figure 5.2 presents an optical micrograph of the indented surface of X80 steel in the top row. Significant plastic deformation (the so-called pileup) leads to distortion of the image around the indentation. Also note that the 100 μm indenter spans several grains and bands. The X80 line pipe steels, are produced by a thermo-mechanical controlled process TMCP and accelerated cooling. The X80 base metal studied had a combination of bainite and ferrite microstructures, with an average ferrite grain size of less than 10 μm. The microstructure exhibited some banding of the discontinuous carbide-containing phase along the rolling direction, which can be noted in Figure 5.2. From the indentation image, it can be seen that the indenter spans several of the ferrite and second phase bands, and the repeatability of the indentation curves in the next section show that the results are an average of the phases and not influenced by the discontinuous bands observed in the

microstructure.

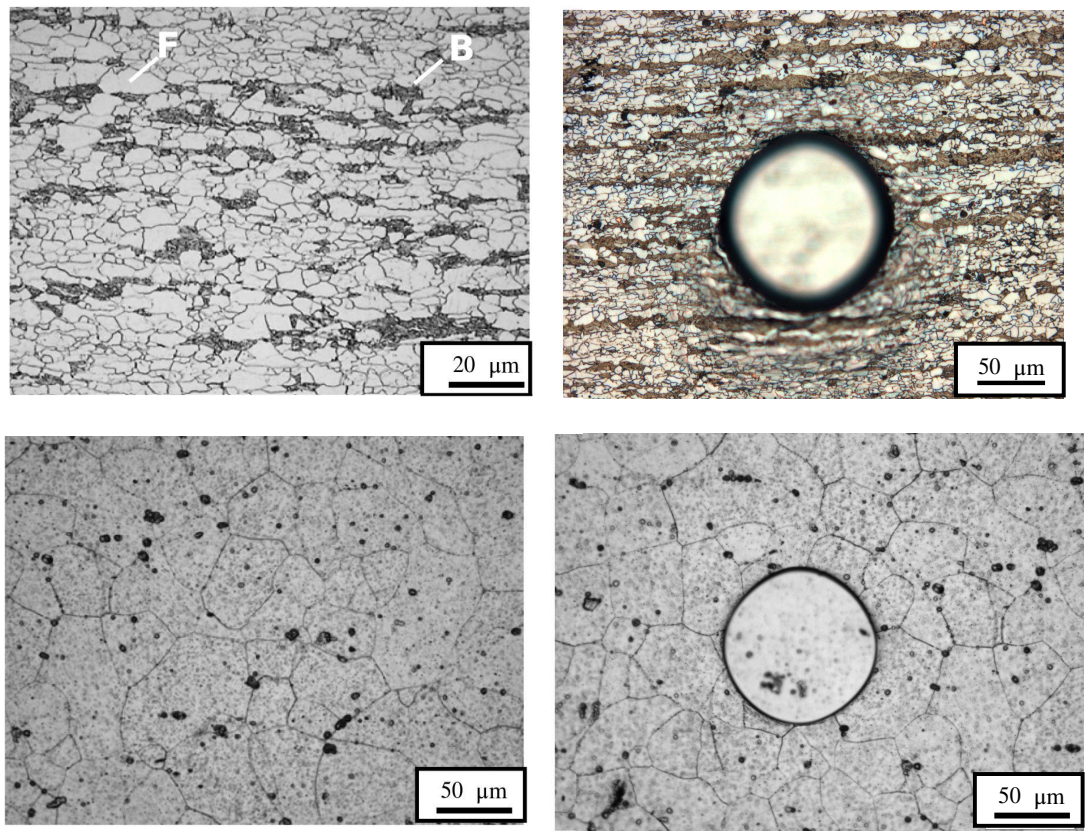

Figure 5.2: Top row: Optical micro-graph of X80 steel surface and micro-graph of 30 N indentation with 100 μm indenter in X80 steel. Note the distortion because of the severe plastic deformation around the indent. Bottom row: micro-graph of AA-6463 aluminum alloy and micro-graph after 6 N indentation with 100 μm indenter in the aluminum alloy.

The AA-6463 aluminum alloy studied here had an average grain size of 40 μm, with an equiaxed recrystallized microstructure as shown in Figure 5.2. The etching also revealed the presence of some dispersoids (which appear as dark pits), however the main strengthening precipitates (Mg_2Si) could not be resolved using optical microscopy.

Table 5.1: Indentation test parameters

Material	Load Setting	Load [N]	Rate [N/min.]
X80	High	30	60
	Low	20	40
AA-6463	High	12	24
	Low	6	12

Unloading rate is similar to the loading rate.

5.5 Results and discussion

Indentation curves for the aluminum alloy for two different peak loads are shown in Figure 5.3. In the low-load case, Figure 5.3 (a), six tests were carried out; from these mean and 90% confidence intervals were obtained. For each fixed displacement, the mean force $\bar{f}$, mean displacement $\bar{\delta}$, and standard deviation s_f were computed. Interpolation between forces was carried out if required. Likewise for each fixed force, the mean displacement $\bar{\delta}$ and standard deviation s_δ were obtained. The 90% confidence interval (CI) on the force is given by:

$$\bar{f} \pm t_{0.05,N-1} \frac{s_f}{\sqrt{N}} \ ,$$

where N is the sample size (six in this case), and $t_{0.05,N-1}$ is the Student's t-distribution for 0.05 and $N-1$ degrees of freedom. Similarly, the 90% CI on the displacements can be obtained. The mean displacements are plotted on the horizontal axis. Due to the low number of samples, the Student's t-distribution is used here; which is also supported by the text by Devore [40] which deal with the confidence interval estimation. The resulting mean indentation curve and the confidence interval bands are shown in Figure 5.3 (b).

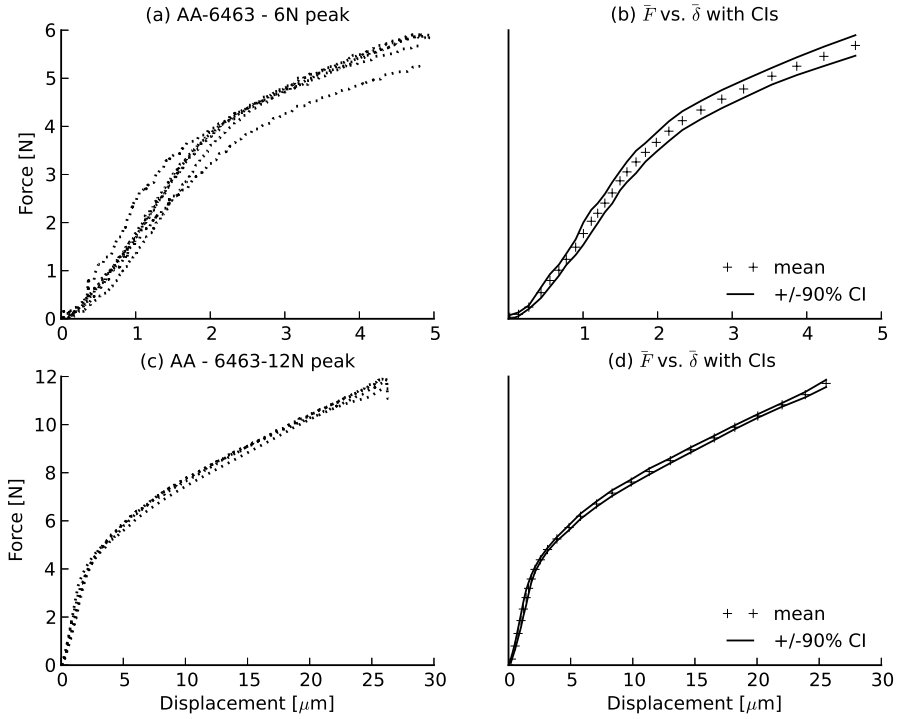

Figure 5.3: (a) Indentation tests for AA-6463 with peak load of 6N (six tests). (b) Plus marks are the mean line and solid lines depict 90% confidence intervals. (c) Indentation tests for AA-6463 with peak load of 12N (six tests). (d) Mean line and confidence intervals.

The repeatability is argued to be acceptable for engineering purposes. It is suggested that the scatter is higher for aluminum indentations, especially in the low-load case, owing to there being only two to three grains being contacted by the indenter. A similar exercise was carried out for the high-load case; the indentation curves and mean and confidence intervals are shown in Figure 5.3 (c) and Figure 5.3 (d), respectively. It can be seen that the repeatability improves. Likewise, indentation curves for the X80 steel are shown in Figure 5.4 for both the 20 N and 30 N peak loads, as well as the mean curves with associated

90% confidence intervals. Again, the repeatability is excellent.

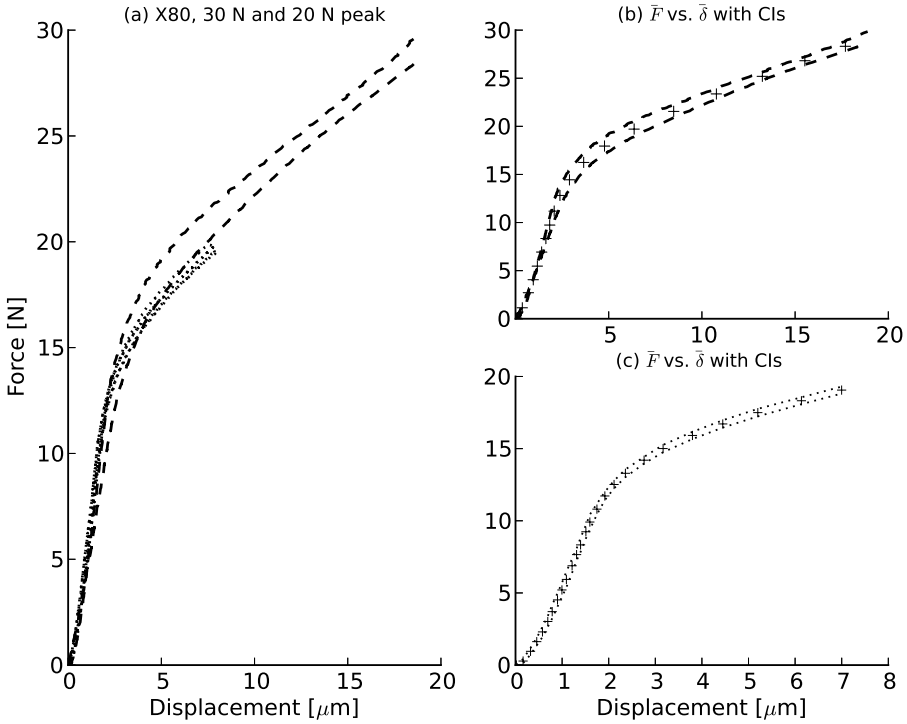

Figure 5.4: Steel indentation curves: (a) raw data for low- and high- load case. (b) Mean and CIs for the 30 N peak load. (c) Mean and CIs for the 20 N peak load.

Some of the features of the indentation curves should be highlighted. The shape of the curves are markedly different from the concave upwards curve obtained using spherical and sharp indenters. Indeed, it is common practice to represent the force-displacement during indentation using a power law of the form $F = C\delta^m$. In bold contrast, for the nearly-flat indenter, there is a steep rising portion, which is somewhat concave upwards and then followed by a change in slope and transition to a portion that is almost linear. Certainly, the curves obtained in this work are not conductive to being modeled using a power law.

5.5.1 Conventional stress-strain curve measurement

For the aluminum alloy, uni-axial tensile tests, per the ASTM-E8 standard, were carried out on sub-size sheet strips coupons. The specimens were cut and machined from aluminum sheet. The machine used for tensile testing was Tinius-Olsen HK10T tensile test frame, with a displacement rate of 1 mm/min.

To carry out the compression tests, several aluminum sheet specimens were glued together to obtain specimens of 7.6 $\pm$ 0.22 mm square cross-section having 15 $\pm$ 0.2 mm length. The samples were loaded along the long axis; that is, with the loading direction parallel to the glue lines. These were loaded in a 50 kN load frame at a rate of 0.1 mm/sec. An extensometer was used to measure the displacement. Planarity and flatness of the surfaces being compressed were found to be crucial to prevent sliding and buckling. It bears emphasis that the compression curves are not as accurate and precise as the tensile stress-strain curves; nevertheless, the tests were performed to obtain an estimate of the yield strength in compression. Consequently, the test was not carried out to large strains.

For loading below yield, both of the materials were assumed to be linear elastic, and Young's modulus for aluminum was taken to be 65 GPa and 210 GPa for steel, respectively. Figure 5.5 shows the tensile and compression stress-strain data for AA-6463. On account of the low strains in the tension test, the inability of the extensometer to resolve the elastic slope is seen in the compression response. The solid line is the fit to Ludwik's law which reads:

$$\bar{\sigma} = \sigma_y + k\epsilon_p^n, \tag{5.1}$$

where $\bar{\sigma}$ is the effective stress, σ_y is the yield strength, ϵ_p the effective plastic strain, k the

hardening coefficient, and n the hardening exponent. Note that the yield strength obtained from the compression test is within 10% of the value from the tensile test. The dashed line in the graph is the Swift hardening law which reads:

$$\bar{\sigma} = k(\epsilon_\circ + \epsilon_p)^n, \tag{5.2}$$

where $\epsilon_\circ$ is a reference strain, which may be taken to be σ_y/E, where E is the elastic modulus. Notice that the Ludwik law describes both the compression response and the tensile response reasonably well and so it was chosen to describe the hardening response of the aluminum alloy.

For the X80 steel, dog-bone specimens per the ASTM-E8 standard were machined in the longitudinal direction for tensile testing. Cubic samples (similar to dimensions used for the aluminum alloy) were machined for the compression testing. Using the special fixture, as for the aluminum alloy, compressive stress-strain curves were obtained. Both the tensile and the compressive stress-strain curves are displayed in Figure 5.6. Again, both the Swift and Ludwik hardening laws are shown. In the case of X80 steel, the Swift hardening model was chosen. While the choice of hardening model, here, is based on engineering practice, the choice is arbitrary as one could choose from several other hardening models. Further discussion of this point is reserved till the last section.

For the alloys studied in this work, there appears to be no significant difference between the yield strength in compression and tension and this tacit assumption is made in all indentation studies.

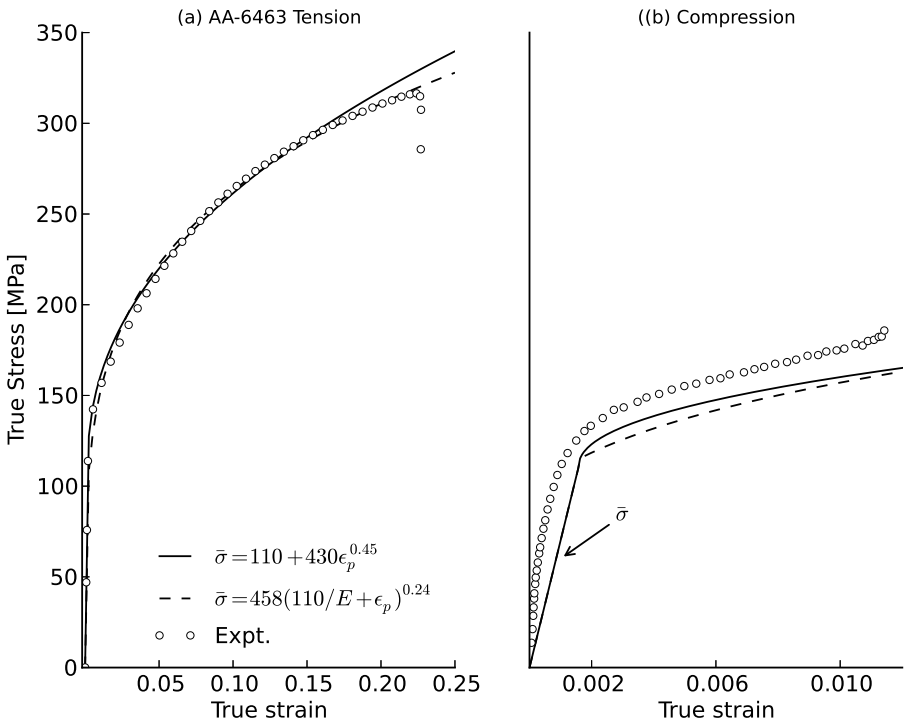

Figure 5.5: (a) Tensile stress-strain curve for AA-6463 from tensile test. Open symbols represent experimental results, solid line is the fit to the Ludwik's hardening equation, and the dashed line is the fit to the Swift equation. (b) Stress-strain curve from compression test.

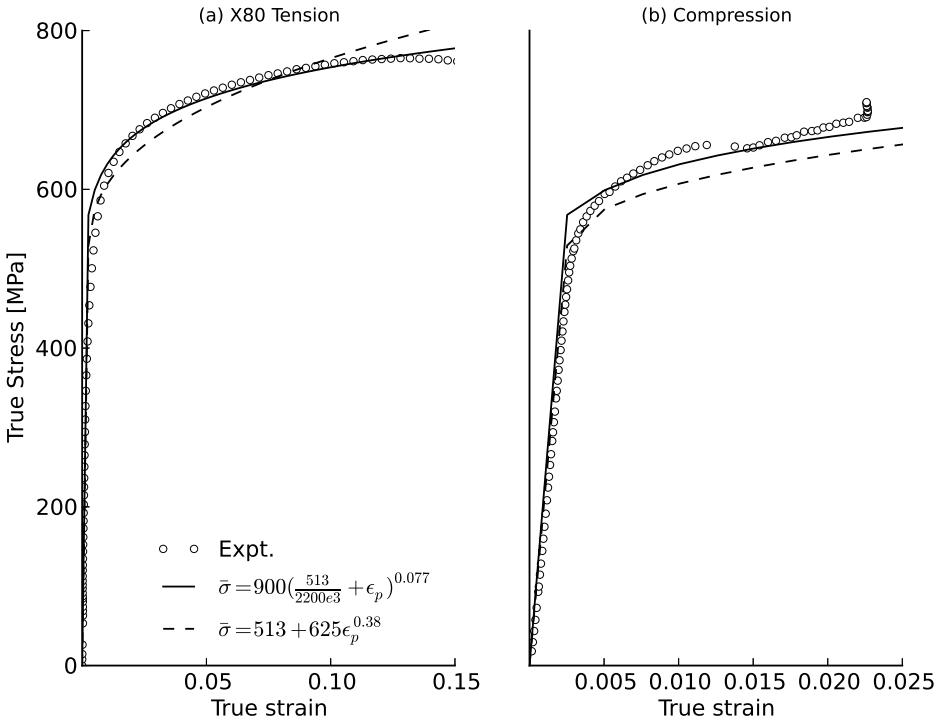

Figure 5.6: (a) stress-strain curve for X80 steel from tensile test. (b) stress-strain curve from compression test. Open symbols represent experimental results, solid line is the fit to the Swift's hardening equation, and the dashed line is a fit to the Ludwik's hardening equation.

5.5.2 Metrics for comparison of computed and measured indentation curves

Before presenting results of the forward finite element analysis of indentation, it is useful to describe metrics that can be used to compare the computed indentation curves with the experimental response. In addition, to the qualitative visual impression, these metrics will quantify the quality of the computational predictions. A body of literature regarding comparison of computational and experimental results is emerging with the increasing emphasis on validation and verification [109]. In particular, for impact and vibration simulations wherein time is a variable, metrics for comparing curves may be found in the articles by [125, 131, 149]. Since time is not a variable in the present work, point-to-point comparison metrics were taken from the preceding references and employed here.

Since the abscissa in the indentation measurement is displacement, with the loading during experimentation (and finite element computations) being displacement controlled, it may be treated as an independent variable. To compare the computed and experimental curves, equal-length vectors of forces corresponding to the same displacements are obtained; the first from the experimental curve is f_i and the second from the computed curve is F_i, with $i = 1...N$. For obtaining equal-length vectors, interpolation between forces may be required.

The first metric is the well-known R-squared term which is defined as:

$$R^2 = \left[\frac{\Sigma(f_i - \bar{f})(F_i - \bar{F})}{\sqrt{\Sigma(f_i - \bar{f})^2 \, \Sigma(F_i - \bar{F})^2}} \right]^2 , \tag{5.3}$$

where over bar denotes mean and summation over N points is implied; $0 \leq R^2 \leq 1$, and a higher value implies better agreement between the two curves. It is well known that the above parameter is sensitive to shape but not sensitive to the scaling or bias of the curve; this is borne out in the results presented later.

Secondly, the Zilliacus Error Index, described by Whang *et al.* [149], can be employed to further compare the computation results to experiment, and it reads

$$Z = \frac{\Sigma|F_i - f_i|}{\Sigma|f_i|}. \tag{5.4}$$

It is the area of the residual $F_i - f_i$ divided by the area of the measured forces and its value can exceed unity; the lower the value of Z, the better the agreement between the two curves. Finally, Whang's inequality is given by

$$W = \frac{\Sigma|F_i - f_i|}{\Sigma|F_i| + \Sigma|f_i|}. \tag{5.5}$$

This last metric is the area of the residual $F_i - f_i$ divided by the sum of the areas of the calculated and the measured; W is bounded between 0 and 1 and the lower the value the better. Whang *et al.* [149] have analyzed the last two and other metrics and they recommend the use of Z when the measurement can be favored over the computation and they recommend W when there is no justification for favoring either the measurement or the computation. In the present work, all three metrics are used and as will be shown later, both W and Z yield consistent conclusions whilst comparing experimental and computational curves.

5.5.3 Finite element computations - forward analysis

With stress-strain curves in place, two-dimensional, axi-symmetric, indentation computations were carried out using the ABAQUS finite element package. This is the forward analysis wherein tensile stress-strain curves are used to model the plastic deformation of the substrate. The computations were performed using the implicit solver with the large deformation option; that is, the loading was quasi-static. Figure 5.7 shows a typical mesh used for the computations; linear quadrilateral with reduced integration, CAX4R (see ABAQUS element technology manual), were used for the substrate. The indenter was modeled as an analytical rigid surface. Based on the SEM image the profile of the indenter tip was constructed. A reference point was coupled to the indenter profile and this point was displaced at constant rate, and the load and displacement of this reference point yielded the indentation curve. All of the bottom row of nodes of the substrate were fixed. Additional computations with an idealized flat indenter were also carried out. To implement the Swfit, and Ludwik hardening laws for steel and aluminum, respectively, the UHARD subroutine in ABAQUS was used; as will be shown in the next section, this subroutine also plays an important role in the inverse approach.

Typically, 6000 elements were used in the simulations and each of the computations completes in approximately 10 minutes when carried out on one processor. The latter point being crucial for completion of the the inverse approach in a reasonable period of time. Interaction between the indenter and substrate was through contact algorithms and the contact was friction-less. Sample surface roughness and indenter roughness features were ignored in the model. It is suggested that subtle discrepancies between experiment

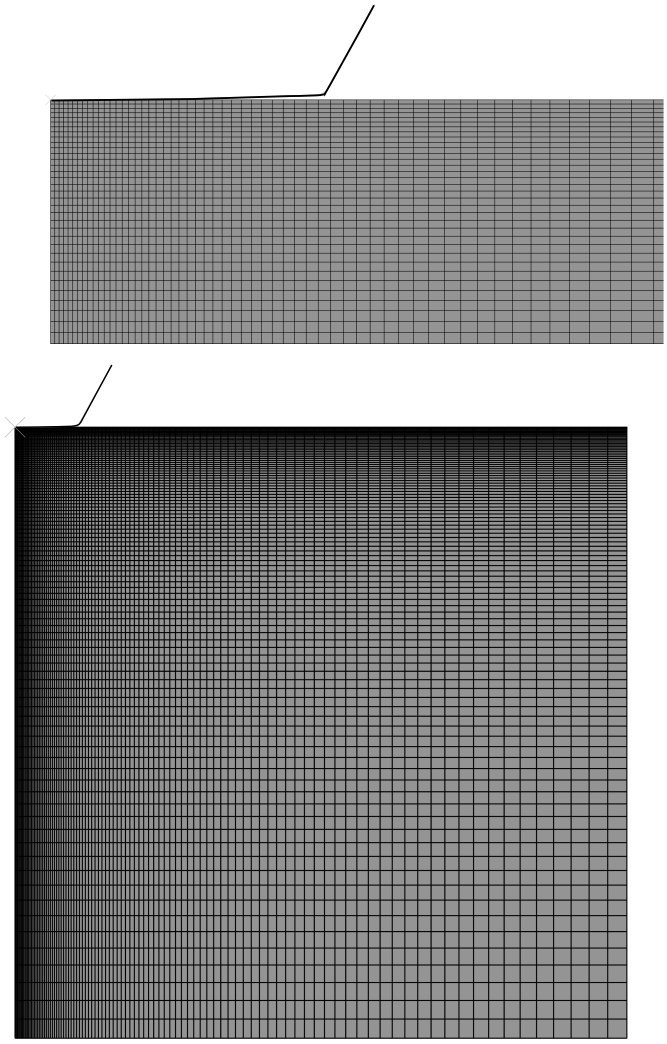

Figure 5.7: Mesh used for the indentation computations. Inset shows profile of the indenter with curved profile and mesh detail. Idealized flat indenter is not shown.

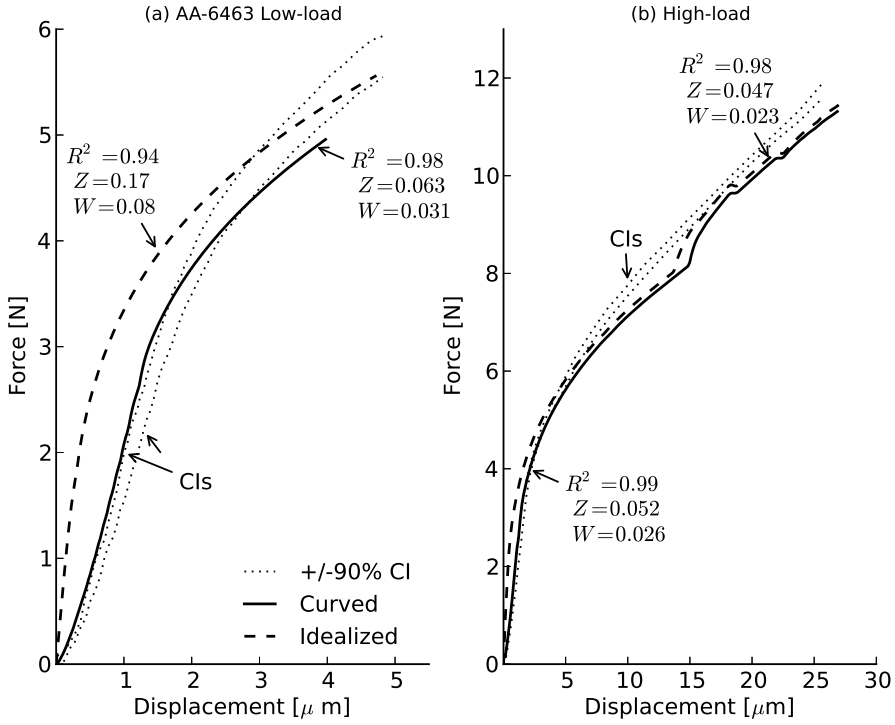

Figure 5.8: Finite element computations for indentation of aluminum, low- and high- load cases. Solid line represents result obtained using curved profile of indenter tip, and dashed line represents results obtained using idealized flat indenter. Experimental indentation curves are shown as 90% CIs. Metrics, R^2, Z,and W are computed with respect to the mean experimental curve.

and computations may be attributed to a combination of surface features of substrate and indenter.

Results of finite element computations for indentation of aluminum alloys are shown in Fig. 5.8. The low-load case had a peak load of 6 N, and the high-load case had a peak load of 12 N. In the low-load case, the idealized flat indenter obtains force-displacement curves that are significantly outside the 90% confidence interval. In contrast, the indenter

with tip curvature gives a force-displacement response not more than 10% outside the 90% confidence interval and is deemed suitable for engineering applications. Visual comparison of the curves supports the latter assertion; additionally, of the three comparison metrics, Z and W provide quantitative support for the assertion. Lower values for the curved indenter and higher values for the idealized case. In contrast, R^2 does not appear to be sensitive to the quality of agreement between the experimental and computational curves. In the high-load case, the indentation curve corresponding to the idealized indenter is well outside the CI until an indentation depth of approximately 2.5 μm. Subsequently, both of the indenter shapes yield indentation curves that are no more than 10% outside the CI.

The computation results for indentation of the X80 steel is presented in Figure 5.9. Here, the low-load corresponds to 20 N and the high-load corresponds to 30 N. For the high-load case, the computation was stopped at indentation depth of 17 μm owing to excessive deformation in the mesh; techniques such as adaptive meshing or Arbitrary Lagrange-Euler may be used to circumvent this. However, the latter two techniques lead to increased computational times, which make them unsuitable for the inverse approach. Again, the forward analysis points to the importance of the incorporating the actual shape of the indenter in the model; values of R^2 and W are lower for the computations with the curved indenter when compared with the results of the idealized model. In contrast, Z and W (especially for the low-load case) does not appear to be sensitive to the agreement between the experimental and computational curves.

There are three observations in the computational results for steel and aluminium alloys. First: In both cases, the agreement between the computational force-displacement curve and the experimental curve is poor over the initial portion (steep rise) of the loading

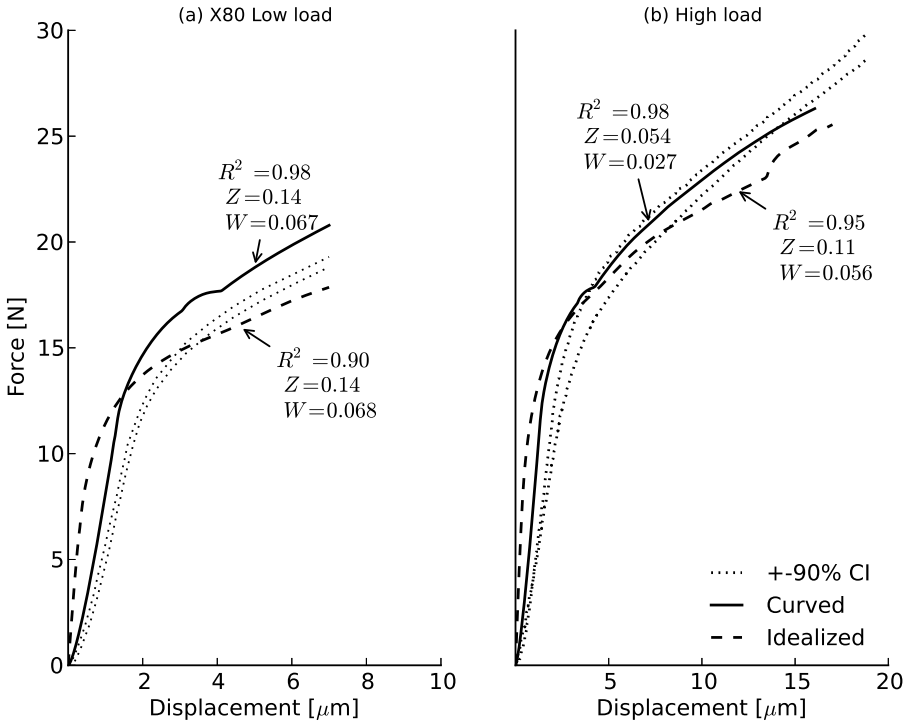

Figure 5.9: Finite element computations for indentation of steel, low- and high-load cases. Solid line represents result obtained using profile of indenter tip, and dashed line represents results obtained using idealized flat indenter. Experimental indentation curves are shown as 90% CIs. Metrics, R^2, Z,and W are computed with respect to the mean experimental curve.

when the indenter is idealized as a perfectly flat face. Second: For aluminium, over the entire indentation depth, the idealized indenter yields indentation curves that are above the curve obtained with the curved indenter tip. Third: For steel, the shallower part of the indentation curve is under predicted by the idealized indenter. These three observations and the phenomenology of the nearly-flat indentation are discussed in a subsequent section. Although, first, the impact of machine stiffness on the indentation curves should be addressed.

Indentation tester and indenter stiffness

In analyzing the instrumented indentation results, the stiffness (or compliance) of the indentation tester is often accounted for (see, for instance, the discussion by Vanlandingham *et al.* [147]). In the present work, to assess the impact of machine stiffness, a set of computations with a linear spring in series with the rigid indenter (shown in Figure 5.7) were carried out. One end of a linear spring was coupled kinematically to the indenter, and the free end was displaced. Load and displacement of the free end were recorded. Figure 5.10 compares the experimental curves with the computed indentation curves with machine stiffness incorporated. With increasing machine stiffness, the indentation load increases and appears to saturate for a machine stiffness of approximately 10^6N/mm, and with this stiffness, the computations are in good agreement with the low-load case but under-predict the indentation loads for the high-load case. Therefore, arguing that the machine stiffness will play a bigger role in the high-load case for X80; it is reasonable to assume that the machine can be assumed to be rigid.

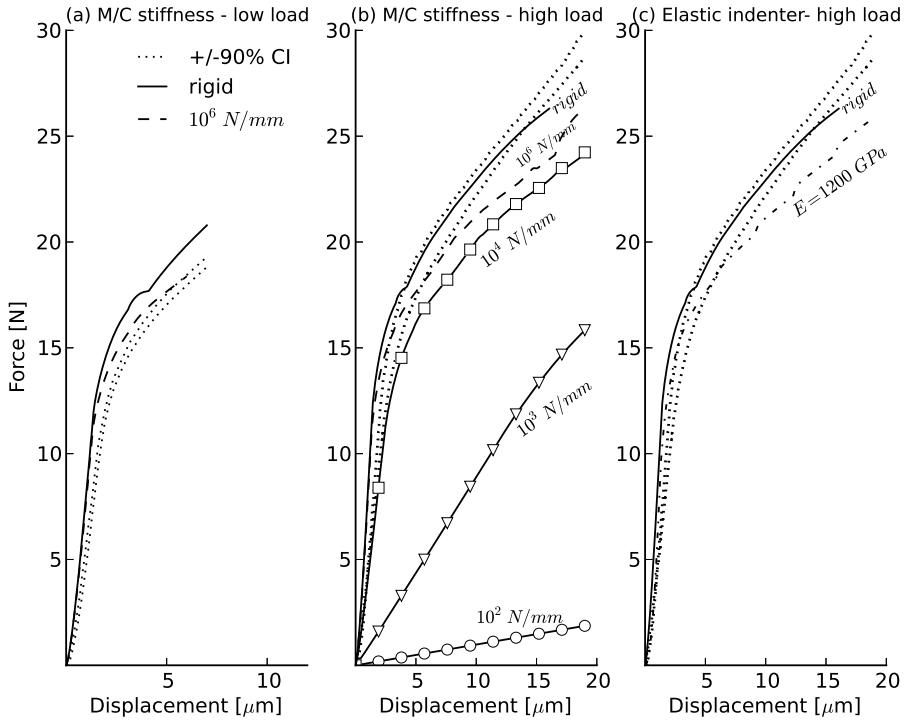

Figure 5.10: (a) and (b) Assessment of machine stiffness on finite element computations for indentation of X80 steel, low- and high- load cases. Solid line represents result obtained assuming rigid indenter. Experimental indentation curves (dotted lines) are shown as 90% CIs. (c) Assessment of indenter elasticity. Dashed-dotted line shows the response of the with elastic indenter.

The foregoing accounts for the stiffness of the machine; the stiffness of the indenter on account of its shape and material may also impact the indentation response. Arguing that prior work ignored the deformation of the indenter, Lee *et al.* in 2005 [91] assumed an elastic spherical indenter (with E= 537 GPa) and obtained empirical relations for estimating elasto-plastic properties from indentation curves. Subsequent work by Lee *et al.* in 2010 [92] also emphasized the elasticity of indenter in the finite element models that were used to obtain regressions used in the inverse approach. Collin *et al.* [32] modelled the spherical tungsten carbide indenters to study stress-strain response of two steel and two aluminium alloys using empirical as well as inverse approach. It is worth emphasizing that research efforts that accounted for the elasticity of the indenter in the finite element analysis used WC indenters whose Young's modulus is 537 GPa; in contrast, the modulus of diamond is between 1000-1200 GPa. In this regard, Cao *et al.* [26] have carried out extensive finite element simulations of spherical indentation wherein they assumed both rigid and elastic response for the indenter and called out the reduction in accuracy of stress-strain curve predictions when the indenter modulus was comparable to the substrate modulus. They found that for a ratio of moduli, $E_I/E > 6$, where subscript I denotes indenter, assuming a rigid indenter was a reasonable approximation. Likewise, Le [90] carried out computational studies of spherical indentation and found that for elastic diamond indenters the yield strength was underestimated by 2.5% for steels and 2% for aluminium.

To assess the impact of the indenter deformation, a forward computation of the high-load, X80 indentation with an elastic, axi-symmetric indenter ($E = 1200\ GPa$, and $\nu = 0.2$) was carried out and the resulting response is shown in Figure 5.10(c). It is interesting to note that the response is identical to the case with a spring constant of $10^6\ N/m$, which

suggests that the results are impacted. These results suggest that in the high-load case (for steel) combinations of machine-stiffness, indenter elasticity, and mesh deformation affect the computed indentation response. For the purpose of the inverse approach discussed in the next section, the indenter is assumed rigid.

Discussion of computational results

Making reference to the low-load indentation of the aluminum alloy, as shown in Figure 5.11, the phenomenology of the indentation is described. The initial portion of indentation curve till a depth of approximately 1.15 μm is slightly concave upwards, and this is on account of the plasticity that emerges even at a depth of 0.25 μm. The contour plot shows that strains of 0.005, below the indenter, have already been attained at this depth even though full contact of the indenter with the substrate has not occurred. When the indenter has displaced 1.15 μm, full contact with the substrate has occurred, and a region which has experienced a strain of 0.018 migrates towards the rounded indenter edge. Full contact also signifies the onset of change in slope of the indentation curve on account of extensive plasticity under the indenter tip. For further indentation to proceed, the substrate has to flow around the sides of the indenter. This is referred to as the pile up and the hardening rate effects begin to play a key role in the response. At an indentation depth of 3 μm, the high strain has localized at the edge of the indenter and is approximately 10%. The average strain is 6% under the indenter at this depth and the plastic zone has expanded as far as possible.

Finally, at an indentation depth of 5 μm, the strain is 20% at the indenter edge and the

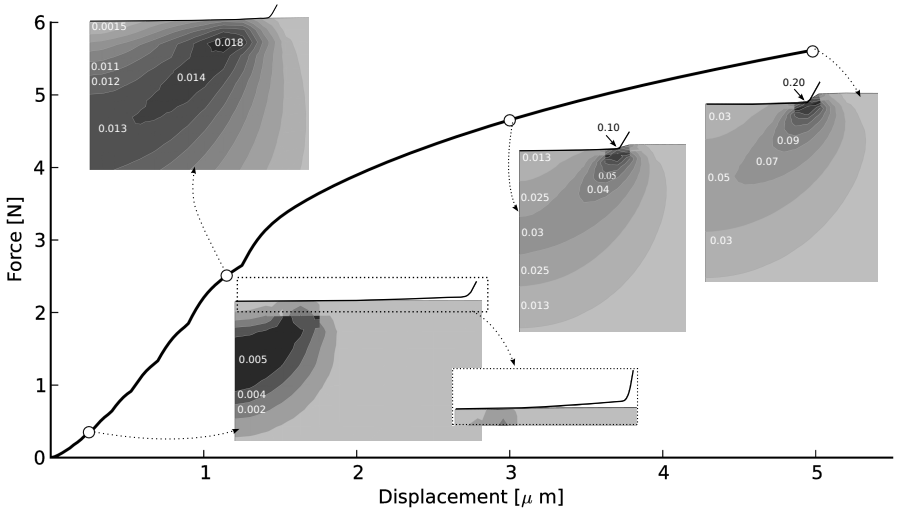

Figure 5.11: Low-load case, indentation of aluminum alloy. Open symbols correspond to depths of 0.25, 1.0, 3, and 5 μm. Contour plots of effective plastic strain corresponding to stated depths are shown. Solid line is the computational result.

average strain is 10% under the indenter. When the plastic strain contours are compared with those for depth of 3 μm, it can be noted that there has not been a significant increase in the size of the plastic zone. These contour plots show that indentation process displays two different modes. The first, prior to full contact of the indenter face, is akin to the expansion of a spherical cavity. There is an approximately sphere-shaped expanding plastic zone. The second, after full contact, wherein the indenter behaves like a rigid body indenting a half space with the high plastic strain being confined to the region near the edge of the indenter face.

To explain the three observations noted at the end of the results section contour plots of the effective strain at several key points along the indentation process are shown in Fig. 5.12. The contours in the top row (for X80) compare the effective plastic strain fields in the idealized and curved indenters. In the latter result, because full contact has not occurred

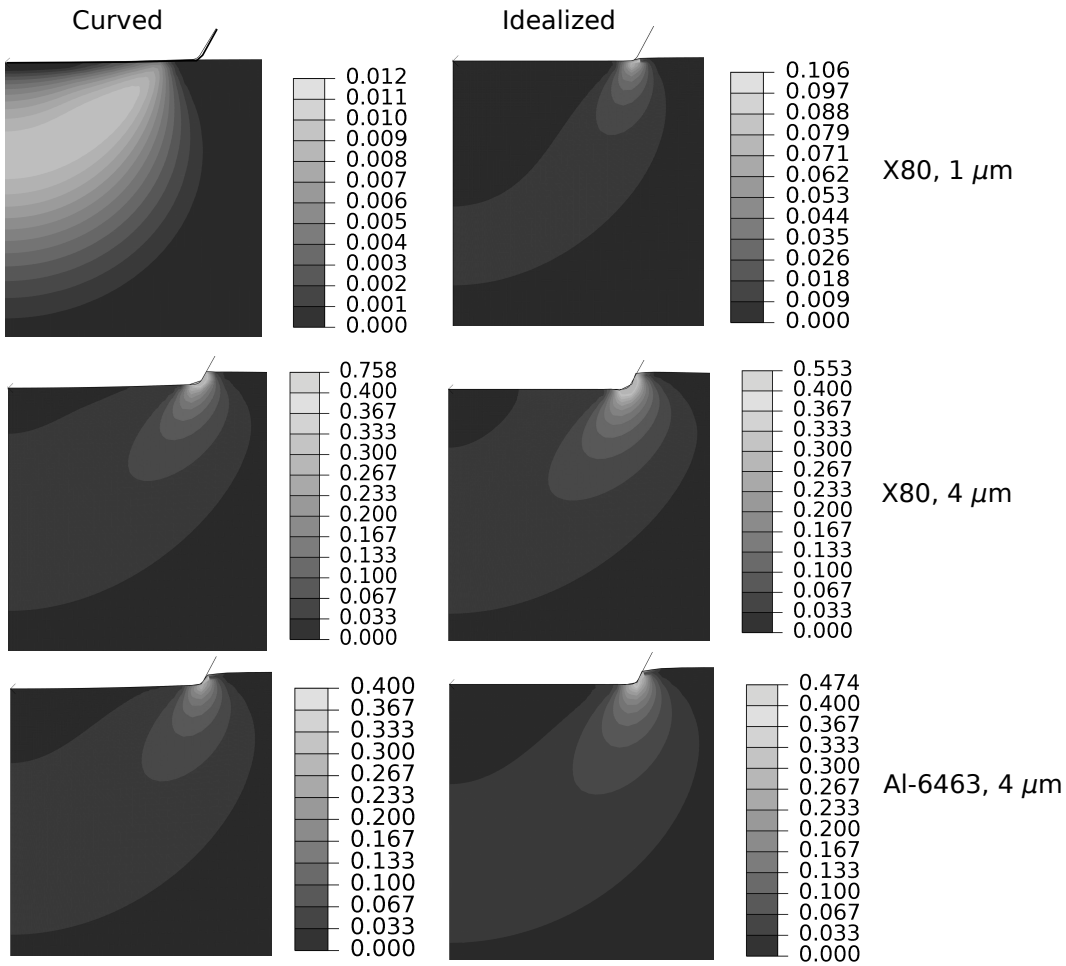

Figure 5.12: Effective plastic strain contours for flat and idealized indenters. The material and indentation depth are indicated.

at a depth of 1 μm, the strains are not as high as in the idealized cylinder wherein the high strain region has already formed at the indenter edge. Note that the highest strain levels in the idealized and curved indenter edges differ by an order of magnitude. Since the computations are displacement controlled, the contours for the aluminum alloy display the same trend. Therefore, the idealized indenter will always over-predict the steeper part of the indentation curve.

The second and third observations are a consequence of the difference in hardening rate in the two alloys; specifically, $d\bar{\sigma}/d\epsilon_p$ is greater for the aluminum alloy than for the X80 steel. Therefore, it is easier to create a pileup for the latter than the former. This is apparent in the contour plots corresponding to an indentation depth of 4 μm shown in Figure 5.12. For corresponding indenter geometries, the strain in the steel is higher than in the aluminum. Due to the interplay between the hardening rate and the indenter geometry, the strain at the indenter edges govern the indentation response. In steel, the strain at the indenter edge is higher for the curved tip, and therefore the indentation curve is higher than the curve obtained with the idealized indenter. In contrast, for the aluminum alloy, the strain at the indenter edge is higher in the idealized case leading to a higher indentation curve.

5.5.4 Inverse approach to determine strength model parameters

The basic idea of the inverse (or reverse) approach is as follows. A set of M control points in the mean experimental indentation curve is selected, $(\bar{\delta}_i, \bar{f}_i)$, where $i = 1...M$. With an initial guess of the three strength model (either the Ludwik or Swift) parameters: σ_y, k,

and n the axi-symmetric indentation computation is carried out and this in turn yields an indentation curve from which a set of forces corresponding to the chosen control points: $(\bar{\delta}_i, _i)$ may be obtained. An objective function ϕ is defined as

$$\phi = \sqrt{\sum_{i=1}^{M} \left(\frac{F_i - \bar{f}_i}{\bar{f}_i} \right)^2}. \tag{5.6}$$

The minimization problem becomes selecting a set of σ_y,k, and n that minimizes ϕ. The minimization was carried out using the Efficient Global Optimization (EGO) algorithm, developed by Jones *et al.* [79], and implemented in the open source Design Analysis Kit for Optimization and Terascale Applications (DAKOTA), see Adams *et al.* [1]. The basic EGO procedure is as follows:

- Carry out a set of functional evaluations based on random sets of (σ_y, k, n). That is, estimates several sets of F_is. Lower and upper bounds for (σ_y, k, n) are specified by the user.

- From the sets of F_i a stochastic response function, which approximates the objective function, is created.

- The response function is then probed (through functional evaluations) for a minimum and if ϕ is minimized to within some specified tolerance, the optimization is completed.

- If a minimum is not found, additional sets of F_i s are obtained (by carrying out further finite element computations) from new values of (σ_y, k, n), the stochastic

function is reconstructed, and the process is repeated till a minimum is found.

It is important to distinguish between the function evaluations of the stochastic response surface, which are computationally inexpensive, and the iteration requiring finite element computation, which is expensive. Note also that because of the random values (though within the specified bounds) of (σ_y, k, n) each run could result in a different fit for the stress curve. Indeed, this serves as a means for obtaining probabilistic distributions to the stress-curve fits and may be used in probabilistic assessments.

In order to carry out the inverse calibration of the hardening model, and yield strength, initial bounds and a limit on the number of iterations (that is the finite element computations) and a tolerance on the minimum attained by ϕ have to be specified. A value of 0.1 was used in this work for the tolerance. There is some judgment involved in this specification of the bounds and, as will be argued later, it requires further investigation. Next the results of the inverse approach are presented for the two alloys.

For AA-6463 the following bounds for the Ludwik law were specified: $100 \leq \sigma_y \leq 200$, $100 \leq k \leq 500$, and $0.01 \leq n \leq 0.9$. Note that the lower bound for σ_y and k can be taken to be equal. The total number of iterations (finite element computations) was limited to 40. Typical run times, using 4 processors for each run, were of the order of 66 min. For each of the results, at least three runs were performed, and there was no significant run-to-run difference. Figure 5.13 (a) and (b) presents fits obtained by using curved indenter, and the idealized indenter in the EGO runs. In the curved case, the fit is excellent for the low-load and the high-load cases. In contrast, the fit is not as good for the idealized case for the low-load experiment. The reason for this is apparent by inspecting the results of Fig. 5.8

(a) and (b) for the computations using the idealized profile. The EGO approach fails to find a good fit owing the inability of the idealized indenter profile to model the low-load indentation case.

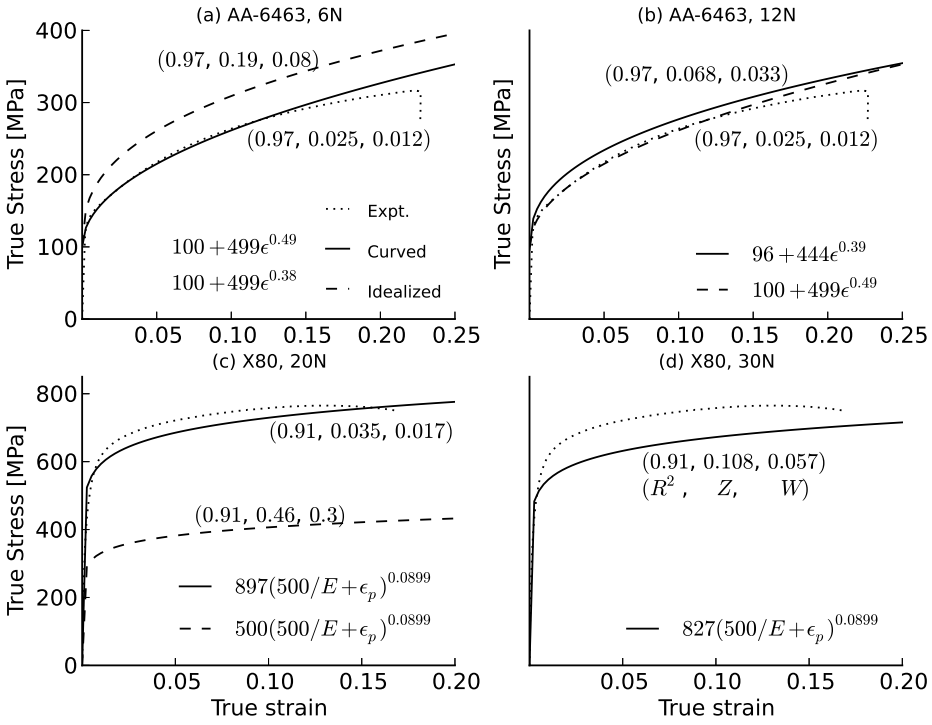

Figure 5.13: Stress-strain curves obtained through inverse approach. Dotted lines are the experimental stress-strain curves, fits obtained through EGO are depicted with solid lines for the curved indenter and dashed lines for the idealized indenter. (a) stress-strain curves for the AA-6463 alloy obtained using a curved profile for the indenter. (b) curves for AA-6463 alloy obtained using an flat profile. (c) and (d) are for the X80 steel and a curved and flat indenter tip, respectively. Triples adjacent to the curves give the values of (R^2, Z, W).

Visual assessments of goodness-of-fit are borne out by low values of W and Z. In contrast, $R^2$is not a reliable indicator of goodness-of-fit. For X80 the following bounds for

the Swift law were specified: $500 \leq \sigma_y \leq 600$, $500 \leq k \leq 1000$, and $0.01 \leq n \leq 0.09$. Notice the tacit assumption that n in the Swift law is usually less than 0.1. The total number of iterations was increased to 60 in this case and the runs were of the order of 132 min (using 4 processors as before). Graphs in Figure 5.13 (c) and (d) present fits for the low-load and the high-load cases, and again, the fits are excellent when the curved profile is used; the stress-strain curves obtained through the inverse approach agree with the curves obtained through tensile tests to with ± 5 % for the aluminum alloy and ± 7% for the steel alloy.

Even though the curvature of the indenter tip is accounted for, the fit is not as good in the high-load case, Figure 5.13 (c); this was related to the high distortion (effective plastic strains greater than unity) of the mesh. In the high-load case for steel, the finite element solver did not converge when the idealized indenter was used and the maximum number of finite element solutions was reached. Accordingly, no fit to the stress-strain curve is reported in the figure. Again, W and Z are consistent indices for comparing computational and experimental curves.

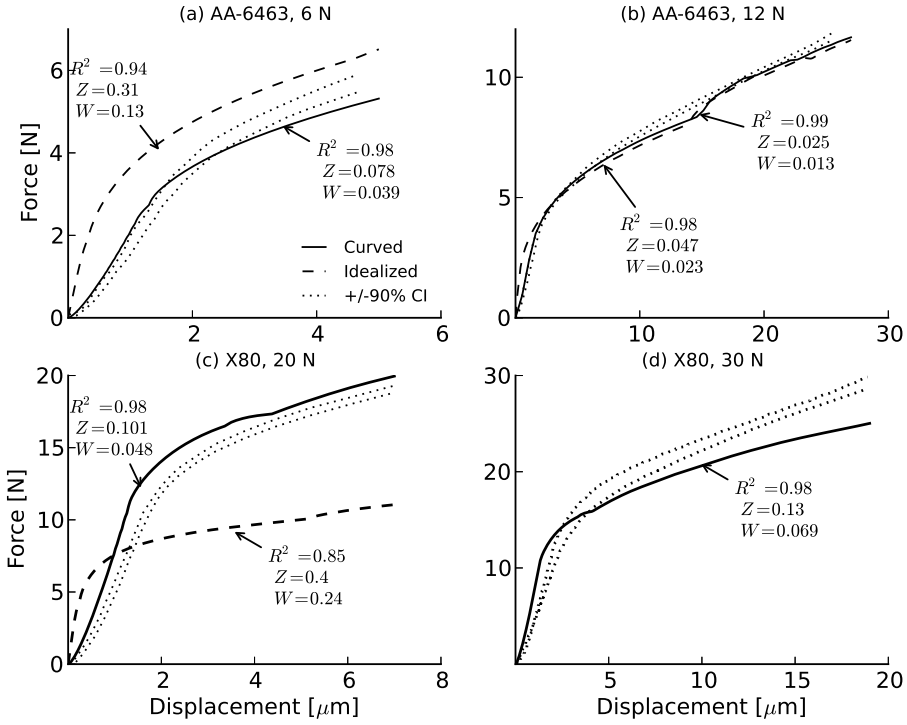

Figure 5.14: Solid lines are computed indentation curves obtained using stress-strain fits displayed in Figure 5.13 and the curved indenter. Dashed lines are computed curves with idealized indenter. Dotted lines are the experimental 90% CIs. Triples adjacent to the curves give the values of (R^2, Z, W),which are computed with respect to the mean experimental curves.

In the absence of results from the forward analysis, only the experimental indentation curves can be relied upon, and the quality of the stress-strain curves obtained using the inverse approach can be assessed through indentation computations. Figure 5.14 displays indentation curves computed using the stress-strain curves obtained using inverse approach. For the aluminum alloy, there is only a marginal change when the metrics R^2, W, and Z, for both curved and idealized indenters, are compared with those of the forward analysis

in Figure 5.8. For the X80, in the low-load case, for the stress-strain curve obtained through inverse approach leads to a computed indentation curve that is an improvement the triple values in Figure 5.9(a) change from (0.98, 0.14, 0.067) to (0.98, 0.101, 0.048) in Figure 5.14(c). Finally in Table 5.2 the hardening model parameters obtained through the inverse approach are compared with parameters obtained by fits to the tensile curves. Values in the table serve to make an important point - even though the model parameters from inverse approach may differ by as much as 16% from parameters obtained from the tensile test, the overall curve still agrees to within 10% of the tensile test.

Table 5.2: Comparison of hardening model parameters

	σ_y [MPa]			k [MPa]			n		
	TT	LL	HL	TT	LL	HL	TT	LL	HL
AA-6463	110	100 (10)	96 (12)	430	499 (16)	444 (3)	0.45	0.49 (8.8)	0.39 (13)
X80	513	500 (2.5)	500	900	897 (1)	827 (8)	0.077	0.09 (16)	0.09

[a] Values obtained using curved indenter in inverse approach are reported.
[b] Swift law is for AA-6463 and Ludwik law is for X80.
[c] TT is tensile test, LL is low load, and HL is high load.
[d] Values in parenthesis are magnitude of relative difference with respect to the values obtained from the tensile test.

5.6 Summary/Remarks

Indentation of AA-6463 aluminum alloy, and X80 steel was carried out using micron-sized, nearly flat, indenters. Forward and inverse analysis using finite element computation demonstrated the importance of using the actual profile of the indenter rather than idealizing it as perfectly flat. In the inverse approach presented in this paper, the fits to the stress-strain curves were in agreement with the curves measured using uni-axial tensile

tests to within less than ±10%. Computations including a finite-stiffness spring in series with the indenter provided support for assuming it to be rigid. With experience gained in the using the EGO method, it is our opinion that the technique is promising for the intended application of mapping stress-strain curves of welds and adjacent regions. However, the specification of bounds for the model parameters, and limit on the number of iterations requires some judgment. Indeed, if the bounds are tightened, the optimization is accomplished with less computational expense. In addition to examining the elasticity of the indenter and machine stiffness, future efforts will focus on development of techniques to rapidly identify tighter bounds with only the indentation curve and indenter geometry as guides. Furthermore, the choice of the hardening model was possible owing to the forward analysis and availability of stress-strain data. A need remains for a technique to identify *apriori* an appropriate hardening model given only the indentation curve.

Chapter 6

Novel Technique to Measure Yield Strength for Engineering Alloys[1]

6.1 Overview

In this chapter procedures to determine yield stress based on two loads from load-displacement curves obtained using nearly-flat, instrumented indenters are presented. Using measured loads during indentation, estimates of yield of steel and aluminium alloys were obtained based on cavity expansion and slip-line theory. The magnitude of the relative error in the estimated yields is bounded by 16%. Estimating the yield strength directly from the load-displacement curve will reduce the number of parameters that are used in the inverse approach and therefore reduce the iteration time.

[1]This is published Manuscript in Materials Science & Engineering A on 17 August 2016, available online:http://dx.doi.org/10.1016/j.msea.2016.08.056 A.R.H. Midawi,C.H.M. Simha, A. Gerlich, Novel techniques for estimating yield strength from loads measured using nearly-flat instrumented indenters.

6.2 Background

In this chapter, novel procedures to estimate the yield strength of metals using instrumented, micron-sized, nearly-flat indenters are introduced. Estimating the yield strength of a metal using a hardness value requires either a knowledge of the strain hardening response or statistical correlations. For instance, the relationships for yield stress presented by Tabor [140], Cahoon [23, 24] or Hawk *et al.* [61] rely on measurements of the Vickers Hardness, the strain hardening exponent (Meyer's coefficient), and an empirical, material-dependent constant. This requires a knowledge of the strain hardening exponent, and renders the preceding relationships unusable for small regions such as the heat-affected zones adjacent to welds or surface treated regions, where the material cannot be extracted and tested in isolation by tensile testing. Examples of using correlations of yield with Brinell hardness are also put forth by Radmard *et al.* [124].

Instrumenting the indenter and measuring the force and displacement during indentation reduces some of the material-specific empiricism associated with yield strength estimation. However, to obtain yield stress by cyclic indentation using a spherical indenter as proposed by Haggag [57, 59] still requires knowledge of the strain-hardening exponent; as shown by Pamnani *et al.* [116] for a recent application of this approach.

Coupling instrumented indentation with finite element computation allows estimation of the entire elasto-plastic response. In this regard, the work of Bhattacharya *et al.* [20] and Giannakopouloset *et al.* [50] using sharp indenters and Alcala *et al.* [2] using spherical indenters are noteworthy. Repeated indentation with spherical indenters and finite element computation may be found in the article by Moussa *et al.* [106].

Accordingly, there is no simple, direct, procedure to obtain the yield strength of a metal using either hardness or indentation curves. Perforce, the user has to resort to either empirical relationships or computations. This is not surprising on account of only the load being known in hardness measurements. Lack of distinguishing features in the indentation curves obtained using sharp and spherical indenters is implicated when the indenter is instrumented. The curves are concave-upwards with no distinctive feature that can be used to discriminate a yield stress being exceeded near the indenter.

In contrast to sharp and spherical indenters, nearly-flat indenters obtain S-shaped indentation curves. For instance, Hu *et al.* [71] demonstrated this behaviour and idealized such indenters as rigid cylinders to analyze aluminum and steel alloys. Moreover, the indenter system's vendor provides software that analyzes the indentation curve to obtain a yield strength based on inflection point description may be found in the article by Leroux [93]; but the physical basis for the procedure is unclear.

In the present work, procedures to exploit the S-shape and identify two loads are presented. Based on the argument that the first load corresponds to the expansion of a spherical cavity, a formula to estimate yield strength is presented. The second load is shown to represent the indentation of a half space by a rigid cylinder and a second formula for the estimation of yield strength, based on slip-line theory, is given. It bears emphasis that conventional steel and aluminium alloys were tested in this work, and the application of the cavity expansion and slip line theory is valid in so far as the material yielding can be described by the von-Mises criterion.

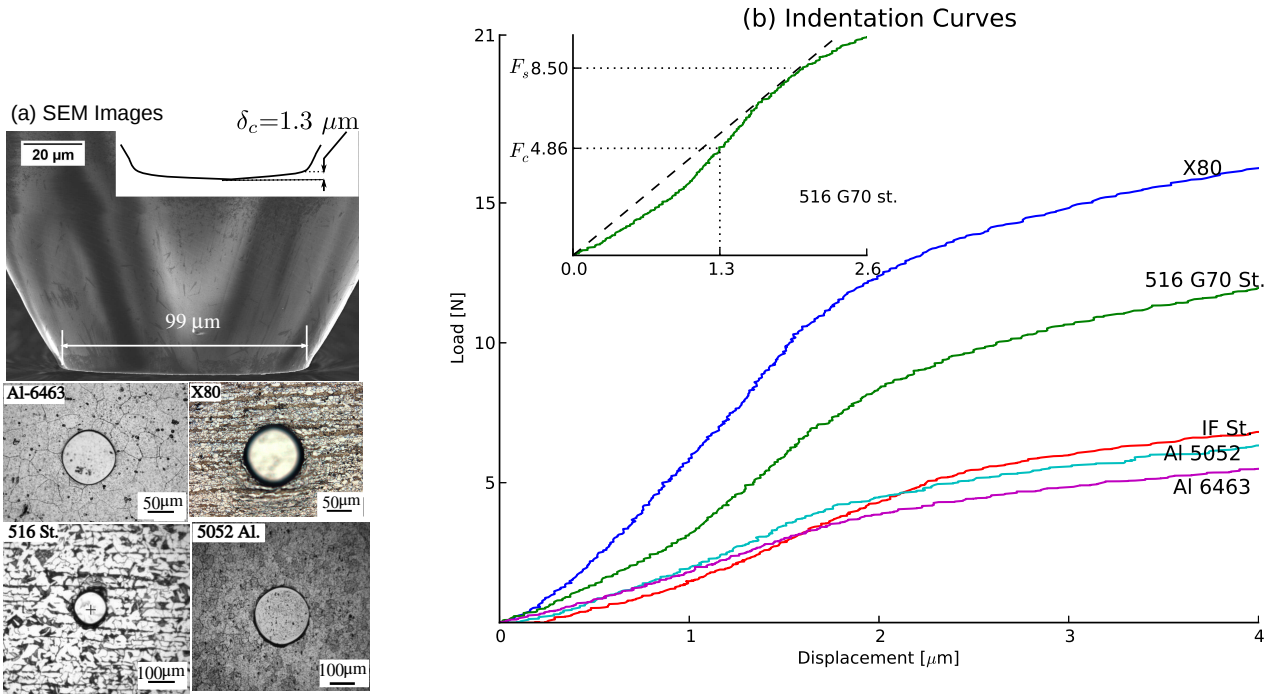

Figure 6.1: (a) SEM image of the 100 μm-diameter indenter and post-indentation micrographs. (b) Indentation curves obtained using the indenter. Inset shows the construction used to obtain F_c and F_s; F_c corresponds to the displacement δ_c, and F_s is the force corresponding to the point where the line through the origin is a tangent to the indentation curve.

6.3 Materials and indentation experiments

A Nanovea-M1 indentation tester was used for all force and displacement measurements. These indenters are axi-symmetric, with a truncated cone profile and have an approximately spherical contact tip; see the Scanning Electron Microscope (SEM) image in Fig. 6.1(a). The height of the spherical portion is designated as δ_c and it is 1.3 μm for the 100-μm diameter indenter and 3.1 μm for the 200-μm diameter indenter.

Yield strengths of five engineering alloys were estimated in this work; where the sample thicknesses and alloys are listed in Table 6.1. Samples were prepared per ASTM E3-11 standard for optical microscopy. Three samples for each material were cut and molded with hot mounting epoxy and ground using silica grit paper 320, 600, and 1200, then polished using cloth pad and alumina suspension up to 1 μm. Finally, automated diamond polishing with 0.5 μm and 0.3 μm were used to ensure high quality surface finish.

Indented surfaces were perpendicular to the rolling direction. Indentation curves are shown in Fig. 6.1. At least 10 indentation experiments were carried out using the 100 μm- and 200 μm-diameter indenters, typical indentation curves using the 100 μm nearly flat tip indenter are shown in Fig. 6.1(b). In contrast to sharp and spherical indenters, these curves are approximately S-shaped.

Two forces, F_c and F_s were obtained from each indentation curve, as described below and the mean and 90 % confidence intervals are listed in Table 6.1. Owing to a 40 N maximum loading capacity, the X80 steel was not loaded with the larger diameter indenter.

Conventional tensile tests per the ASTM-E8 standard were carried out to obtain yield strengths using the 0.2 % offset method. Tensile tests were repeated at least 3 times for

each material to assess repeatability. A displacement rate of 1 mm/min was used in all of the tests, and the loading direction was parallel to the indentation direction. The preceding choice of loading direction accounts for potential anisotropy of yield strength. Table 6.1 lists the mean and 90% confidence intervals for the 0.2% offset yields and also the grain sizes for each of the alloys.

6.4 Yield strength estimates

The first estimate is based on the assumption that when the depth of indentation is δ_c the hemispherical part of the tip has penetrated the substrate and there is full contact. The force F_c corresponding to δ_c is obtained from the indentation curve and used to compute the yield strength using

$$\sigma_y = \frac{1}{2.2}\frac{F_c}{\pi a^2} , \tag{6.1}$$

where a is the radius. The theory behind the factor of 2.2 is given in the next section.

The second estimate of yield is based on the observation that for indentation depth greater than δ_c, there is a point in the process, before the onset of pileup, when the highest plastic strain is concentrated at the edges of the indenter. Accordingly, at this point, the indenter can be treated as a rigid cylinder indenting a half space. The load corresponding to this point, F_s, can be identified by constructing a tangent to the curve as shown in the inset of Fig. 6.1(b). Shield in 1955 [133] used slip-line theory to show that the pressure required to indent a semi-infinite substrate by a rigid cylinder is 2.845 $(2\sigma_y/\sqrt{3})$, where the factor of $2/\sqrt{3}$ is on account of the assumption of a von-Mises material. Therefore σ_y,

is given by

$$\sigma_y = \frac{1}{3.28}\frac{F_s}{\pi a^2} \ . \tag{6.2}$$

The work of Ya *et al.* [156] may also be consulted for further elaboration on this relationship. The bar charts in Figure 6.2 show the yield strengths estimated from the measured forces, along with yield stress values obtained through tensile testing. Error bars are the standard deviations of the means. Charts at the bottom show the relative errors in the procedures proposed in this work. The magnitude of the relative error is bounded by 16%.

6.5 Theoretical background

To clarify the mechanics of this indenter shape, a rigid indenter model was constructed using the SEM image of the indenter and used to indent a metal substrate in axi-symmetric, finite element computations; these were performed using the ABAQUS finite element software [37]. For instance, the substrate was modelled by taking a Young's modulus (E) of 210 GPa, Poisson's ratio of 0.3 and a hardening law of $900(\sigma_y/E + \epsilon_p)^{0.077}$, where ϵ_p is the effective plastic strain, which was used to obtain the indentation response of a 100 μm-diameter indenter. The indentation curve is shown in Figure 6.3 along with contour plots of effective plastic strain. For the 100 μm indenter, when the indentation depth is $\delta_c = 1.3$ μm then the spherical section of the indenter establishes full contact with the substrate. It bears emphasis that the computation was carried out to clarify the mechanics, no finite element computations are required for the yield strength estimation method de-

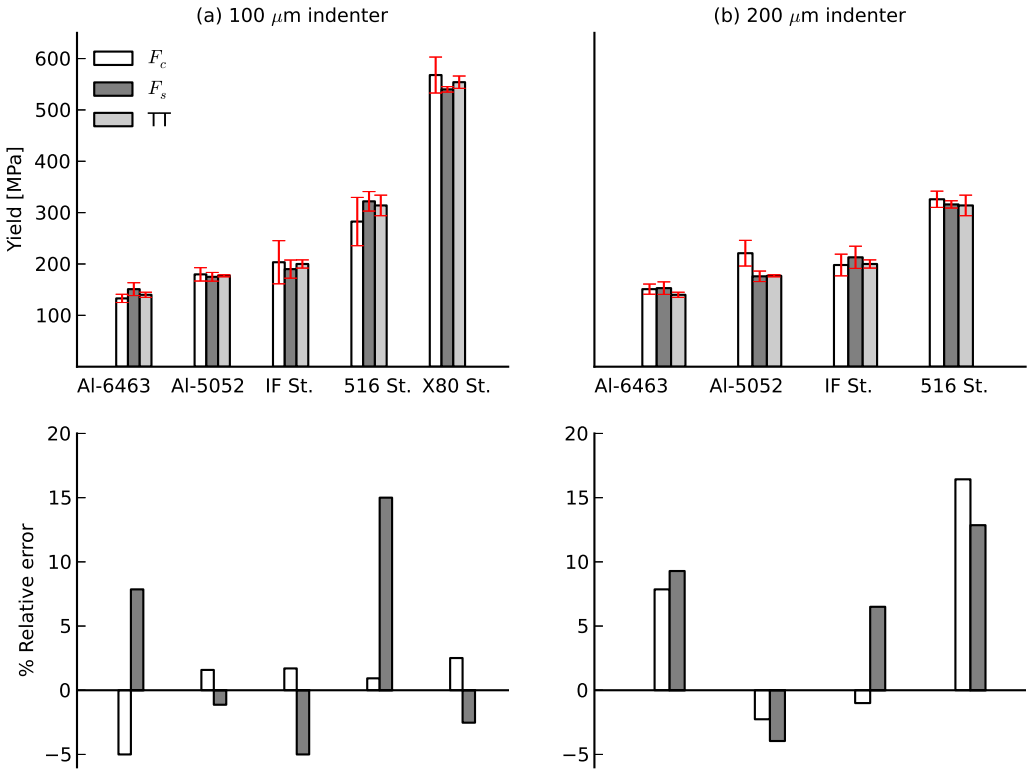

Figure 6.2: Top: Bar charts showing yield strength values obtained based on F_c and F_s points. Bottom: Correlation between the yield strength based on Cavity mode (F_c) and slip line mode (F_s) compared to the 0.2 % offset yield obtained by uni-axial tensile testing (TT).

scribed above. Making reference to Figure 6.3, when the spherical portion of the indenter is partially in contact (the first contour plot) with the substrate, a spherical plastic zone forms. When full contact occurs (the second contour plot), then the spherical plastic zone is fully developed. The elastic-plastic boundary, c/a, is approximately 2.1. This ratio is independent of substrate modulus and hardening response; and it was confirmed that the latter assertion holds for moduli and hardening typical for aluminum and steel alloys. This is attributed to the low *average* plastic strains under the indenter. Park *et al.* [154] carried out extensive finite element computations and showed that at yield, the plastic strains are sufficiently low so that the response of the spherical indenter is independent of the elastic modulus, hardening behaviour and yield strength.

Hu *et al.* in 2015 [71] have also performed finite element computations for several steel and aluminum alloys and they quote $c/a = 2.24$. See also Hernot *et al.* [64], who obtained $c/a = 2.2$ for elastic-perfectly plastic metals using finite element computations; and Zielinski *et al.* [148] who experimentally showed during indentation of Fe-3 wt.% Si single crystals that $c/a = 2.1$. In the present work, $c/a = 2.15$ was used as it was the plastic zone size measured in the simulations (see dimension in Figure 6.3). Any of the other three values of c/a from the literature will result in at most a 2% change in the final factor of 2.2 in Equation 6.1. Based on the foregoing analysis, for an indentation depth of δ_c, the indenter may considered to be driving the expansion of a spherical cavity. Cavity expansion theory (see, for instance, Hill [67]) provides the force to expand a spherical cavity as $F_c = \sigma_y \pi a^2 [\frac{2}{3} + 2 \ln \frac{c}{a}]$, where σ_y is the yield strength in the sense of the von-Mises criterion. Taking $c/a = 2.15$ gives the factor of 2.2 in Equation 6.1.

With a subsequent increase in indentation depth, the behaviour of the indenter is

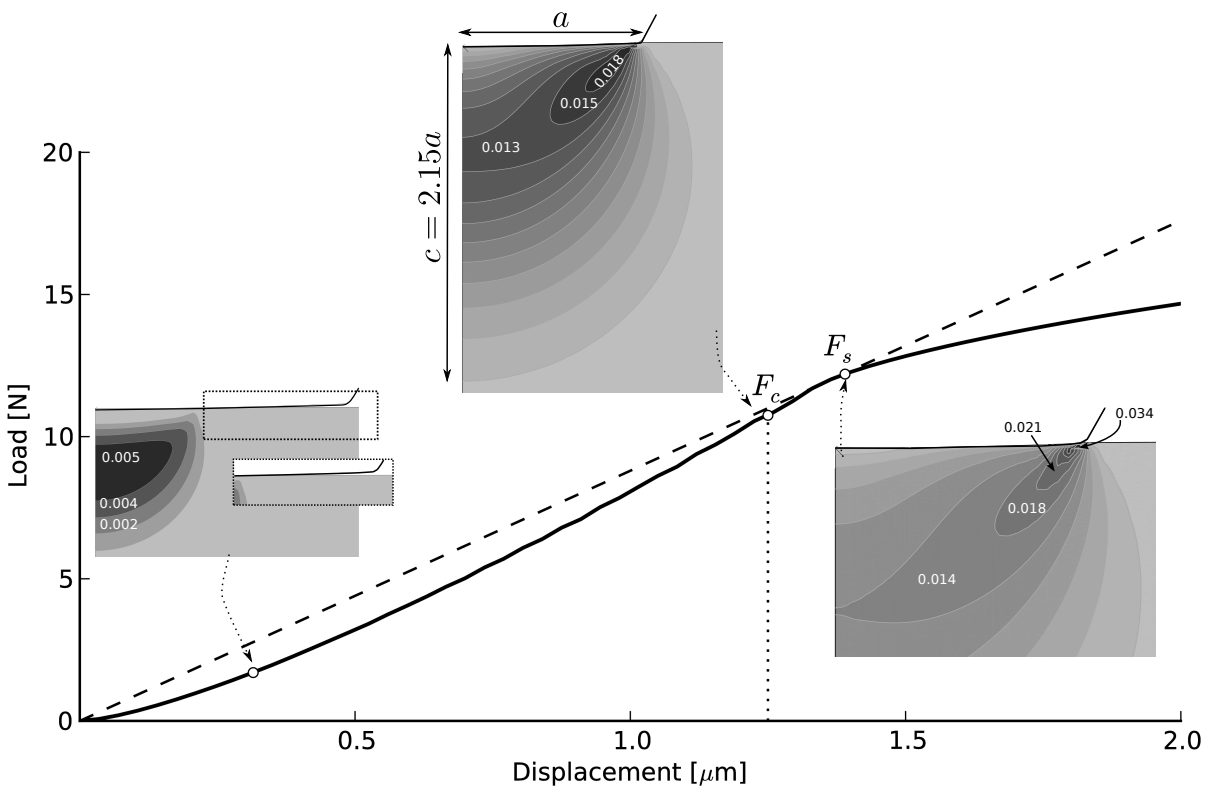

Figure 6.3: Indentation curve obtained through FE computation. Contour plots of effective plastic strain are shown for three depths. Average strains in some regions reported. Load F_c corresponds to displacement at δ_c, and load F_s is obtaining by from the tangency point of straight line through origin.

briefly similar to a rigid cylinder indenting a half space. As can be seen in the third contour in Figure 6.3, the plastic strain is concentrated at the indenter edge and no pileup has occurred. Notice that the strain is almost double when compared with the previous state, but the average strain under the indenter is still low. As shown in Figure 6.3, the load F_s can be identified using the proposed construction. Note that if the average of the yields obtained using the two models is used, the relative error is bounded by 10%.

Table 6.1: Forces from indentation curves and yield strength from tensile tests.

		Al- 6463	Al-5052	IF St.	516 St.	X80 St.
100 μm	F_C [N]	2.3±0.14	3.1±0.22	3.5±0.74	4.8±0.81	9.8±0.61
	F_S [N]	3.9±0.31	4.5±0.22	4.9±0.45	8.3±0.48	13.9±0.13
200 μm	F_C [N]	10.45±0.6	11.9±1.5	13.7±1.46	22.54±1	-
	F_S [N]	15.9±1.26	17.58±1.8	21.99±2	32.62±0.7	-
0.2% σ_y[MPa]		140±5	177 ±2	200±8	314±20	554 ±12
Thickness [mm]		1.2	3	0.83	13	15
Ave. grain size [μm]		41	26.7	25	20	6

a At least 10 tests per indentation were conducted.
b Grain sizes are based on the linear intercept method.

6.6 Summary / Remarks

It is not suggested that the proposed methods are a substitute for tensile testing, but as a new interrogation methods for comparing local yield stresses, especially in heterogeneous materials such as welds. The methods exploit the S-shaped indentation curve to identify loads such that average strain levels under the indenter are low enough that the strain hardening does not impact the yield estimates. Another tentative result is that at least approximately four grains appear to be sufficient to probe the yield strength. It is recognized that surface asperities have to be plastically deformed for full contact to occur and therefore, the yield estimate using F_c is expected to be sensitive to surface finish and normality of contact of the indenter profile with the substrate. The quality of the contact surface between the sample and the indenter was found to impact the measured forces. Repeatable measurements that led to the above bounds were achieved with surface finishes that are used for obtaining optical micrographs.

Chapter 7

Assessment of Yield Strength Mismatch using Indentation for X80 Pipeline Steel Welds

7.1 Overview

Many oil and gas pipelines recently have been designed using the strain-based design approach (SBD), which allows stress in the pipeline to exceed the yield strength. The latter is owing to displacement-controlled loads such as landslides, seismic motions, and frost heave. In such cases, the distribution of the strain over a large area (pipe) rather than local area (weld) are preferred. Therefore, strength overmatching is one of the requirements of the strain-based design (SBD) approach. In this work API-X80 pipeline steel sections

were joined together using the robotic GMAW process, while varying filler metals and shielding gases to achieve different levels of strength mismatch. Then weld metal and HAZ microstructures were investigated and correlated with microhardness map to ensure different mismatch levels were achieved. In order to study the yield strength mismatch both the indentation technique and conventional tensile testing were performed. The indentation technique employed a 100 μm diameter nearly flat indenter, used to estimate yield strengths for welds (WM and HAZ) using load-displacement response for each zone. The measured yield strengths was compared with 0.2% offset tensile yield strength obtained by conventional tensile test. The result showed good agreement between the yield strength measured by the two techniques. The results showed that the nearly flat tip indentation method can be used as a tool to estimate strength mis-match for pipeline application. Moreover, the indentation method was able to estimate the yield strength for narrow zones such as reheated weld metal versus deposited weld metal, CGHAZ, and FGHAZ, which could be used as an input for finite element modelling to simulate the welded structures more accurately.

7.2 Background

To avoid failure in the weld metal region, pipelines are designed according to strain-based design (SBD) criteria [70, 96]. Since pipelines may experience high longitudinal deformability, strength overmatching is one of the important requirement for SBD in pipelines application to avoid local strain accumulation in the girth weld when the pipeline is subjected to displacement controlled loading [104]. Overmatch can be defined as a condition

where the yield strength of the weld metal is known to be more than the yield strength of the adjacent base metal. DNV-OS-F101 standard specifies the yield strength overmatch to be 120-150 MPa higher than the SMYS of the base metal. This is due to the scatter in the pipe yield strength [122]. In addition, DNV-OS-F101 stated that overmatching can help to minimise strain concentration in the area adjacent to any possible defects in the weld [39]. The overmatching then can be calculated using equation 7.1.

$$M = \frac{\sigma_{y(Weldmetal)}}{\sigma_{y(Basemetal)}} \tag{7.1}$$

Most of the Engineering Critical Assessment (ECA) standards such as API, CSA-W59, CSA-Z662, and DNV require cross-weld tensile testing to be performed. As a general practice, if the cross weld sample failure occurs in the base metal or HAZ, the weld will be considered in the overmatch condition. However, in this case the weld metal and base metal properties were not compared directly. That could lead to a non-conservative assessment of overmatching properties.

To compute the over (or under) match, tensile tests according to ASTM E8/E8M standard, for the weld metal and base metal are required. However, the general practice is to extract all weld metal parallel to the hoop direction of the pipe and assuming the weld metal has isotropic properties. Note that machining all weld dog-bone specimens in the hoop direction is straightforward. The reason for this assumption is the difficulty of gaining the mechanical properties of the weld in the longitudinal direction of the pipe [66, 80]. Bally [15] studied the local properties of pipeline girth welds by means of hardness mapping technique. Bally reported that the yield strength that has to be used for strength mis-

match assessment is that for the weakest material. However, the overmatching properties are usually described by yield strength and not hardness. Therefore, there is a need for new technique to assess the strength mis-match accurately and rapidly for pipelines and welds.

Consequently, the aim of this chapter, is to describe the application of the novel indentation technique presented in Chapter 6 to estimate the yield strength for welds. The strength mismatch properties for different X80-pipeline welds were evaluated using the indentation technique and compared to the yield strength at 0.5% strain level obtained by conventional tensile testing. In addition, the yield strength for narrow zones through the weld such as the reheated weld metal versus as-deposited weld metal, and HAZ were estimated. Moreover, the yield strength and hardness results were correlated with the observed microstructures.

7.3 Experimental procedure

Three joints were produced using a robotic GMAW equipped with a Lincoln Power Wave 455M. Constant voltage (CV) mode was used to produce the welding joints. Curved sections of API-X80 steel pipe was prepared with dimensions of (280 x 233 x 15) mm^3, a narrow groove was machined and prepared to weld as shown in Figure 7.1 (for further information, see Chapter 3). Two different welding consumables and shielding gases were used in order to produce different microstructures in the fusion zone and consequently different mechanical properties. The samples were designated as W1, W2, and W3. The first sample W1 was welded using wire which has slightly higher hardenability and 85%Ar-15%CO_2 shield-

ing gas, while samples W2 and W3 were welded using lean wire with shielding gas mixture of 50%Ar-50%CO_2. The welding parameters were designed to achieve different levels of strength mismatch. To achieve that, W1 and W2 samples were welded using the same welding parameters except the voltage was increased by 10%. This will keep the arc length similar since that can be affected when the percentage of the %CO_2 in the shielding gas increases. The preheating-interpass temperature was kept constant at (150 °C). To achieve under-matching weld condition, the welding parameters were adjusted for the third sample W3. The travel speed was reduced approximately 10% to increase the heat input. In addition, the preheating and interpass temperature was increased to (250 °C). This change in the heat input and preheating temperature will lead to an increase in the cooling time, which will decrease the cooling rate, and as a consequence a coarse microstructure will be formed.

Figure 7.1: Welding fixture setting.

The details of the welding parameters for each condition are listed in Table 7.1. It should be noted that the preheating-interpass temperature for W3 sample was very high

and impractical for actual production applications. Also, the under-matching condition is not recommended in pipeline application. However, it was intentionally created to validate the indentation technique and compare in different weld situations. The welded samples were then cut and mounted in order to prepare coupons to compare the hardness level in the weld zone with the base metal. The samples that achieved the required hardness value were selected and sent for X-Ray testing in order to check any major defects, such as lack of fusion and porosity, which might effect the subsequent mechanical testing results.

The welded joints that achieved the required hardness level and passed X-Ray test were selected to perform mechanical and microstructural analysis. The chemical composition was performed according to the ASTM E3-11 standard. To perform chemical composition analysis all weld metal samples were cut from the middle section of the weld. Notice that W2 and W3 samples were welded using same wire; therefore, one sample was considered for chemical composition. The chemical composition and the carbon equivalent for the base metal and welded samples are listed in Table 7.2.

Table 7.1: Welding parameters for each condition.

Sample#	W1			W2			W3		
Pass	Root	Fill	Cap	Root	Fill	Cap	Root	Fill	Cap
Volatge-[V]	24.6	24.6	21.6	27.6	27.6	25.1	27.2	27.7	25.2
Current-[A]	315	288	219	287	266	195	290	265	204
T. Speed-[m/min]	12	6.9	3.0	12	6.9	3.0	10	5.8	2.52
Wire speed-[m/min]	9.50	8.50	6.0	9.50	8.50	6.0	9.50	8.50	6.0
Heat input-[kJ/cm]	3.90	6.20	9.50	3.95	6.30	9.70	4.70	7.60	12.0
Shielding gas	85%Ar-15%CO2			50%Ar-50%CO2			50%Ar-50%CO2		
Preheat-[°C]	150			150			250		

Three samples from each of the welds were prepared according to ASTM standard

E3-11 in order to characterize the microstructure, perform hardness map, and estimate yield strength using instrumented indentation technique. Optical microscope and scanning electron microscope were used to characterize the microstructure in the weld metal and HAZ regions.

Table 7.2: Chemical composition of the welds and base metal along with carbon equivalent values (Ceq*)

Sample#	C	Mn	Si	Cu	Al	Mo	V	Cr	Ti	O	N	Ceq
BM	0.051	1.73	0.18	0.12	0.03	0.21	0.01	0.03	0.01	0.0011	0.0040	0.189
W1	0.086	1.76	0.55	0.33	0.01	0.53	0.01	0.01	0.01	0.018	0.0037	0.278
W2,3	0.076	1.32	0.54	0.10	0.01	0.07	0.01	0.01	0.01	0.045	0.0040	0.196

$$*C_{eq} = \frac{Si}{25} + \frac{Mn}{16} + \frac{Cu}{16} + \frac{Ni}{40} + \frac{Cr}{10} + \frac{Mo}{15} + \frac{V}{10}$$

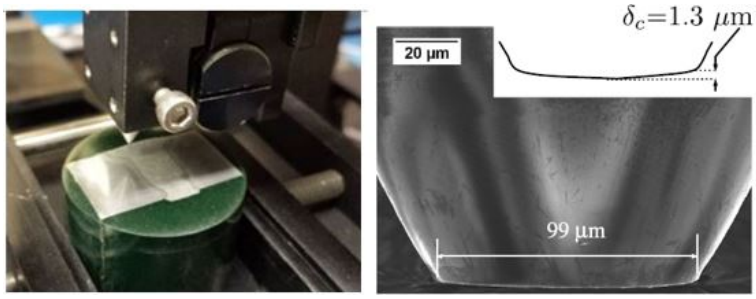

Figure 7.2: Indentation test setting.

The same loading parameters and indenter size were used for the base metal, WM and HAZ. Based on the results from Chapter 5 and 6 for X80 pipeline material the peak load was set at 20 N, the loading rate was 40 N/min, contact load was 20 μN, and the approaching speed was 3 $\mu m/min$. The indenter size is about 100 μm as shown in Figure 7.2. To measure yield strength using indentation technique, the optical microscope in the indentation system was used to select the indentation area. Specific regions in the WM or HAZ can be indented as shown in Figure 7.3.

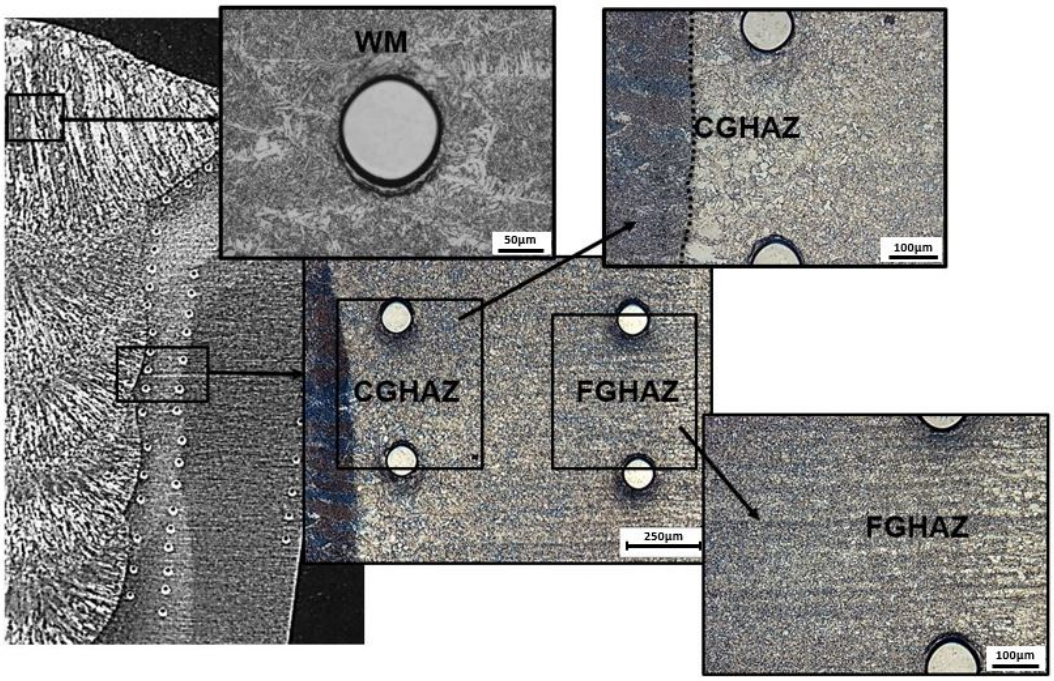

Figure 7.3: Indentation test procedure in different zones through the weld joint cross section.

The yield strength was obtained using cavity expansion formula that suggested in Chapter 6 as follows:

$$\sigma_y = \frac{1}{2.2}\frac{F_c}{\pi a^2}\ , \tag{7.2}$$

where a is the radius of the indenter and force F_c corresponding to δ_c is obtained from the experimental indentation curve.

Conventional tensile testing was performed for the welded joints in both directions all weld metal and cross the weld. Three samples for each condition were prepared. The samples were cut out using EDM technique as mentioned in the methodolgy Chapter 3. The tensile test frame used for tensile testing was Tinius-Olsen HK10T with a displacement

rate of 1 mm/min. The tensile testing was combined with the DIC system, which allows one to map strain in different zones through the joint. This can be used to construct stress-strain curves, for each of the zones, based on the iso-stress assumption as described in prior work [126, 151].

7.4 Results and discussion

7.4.1 Macrostructures and hardness maps

The macrographs of the girth welded joints are shown in Figure 7.4. The pass sequence and the HAZ size are evident. Specimens W1 and W2 have similar HAZ widths considering that the heat input was kept similar, while W3 sample has wider HAZ size since the heat input was slightly increased. As can be seen in the macrographs there is a rather different distribution of as-deposited and reheated weld metal between W1 and W2 versus W3. The dashed lines show the location of sample extraction for cross-weld tensile tests.

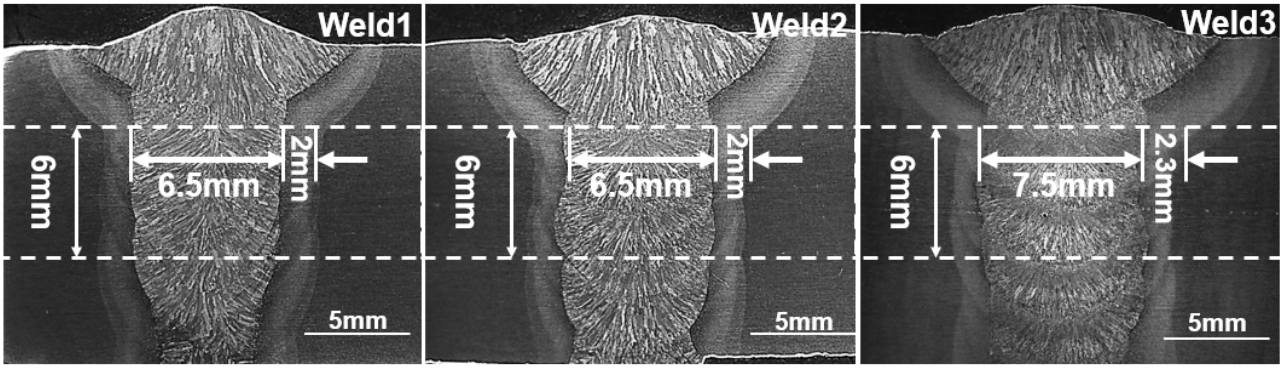

Figure 7.4: Macrostructure graphs for welds W1, W2, and W3.

The microhardness maps of the girth welded joints are shown in Figure 7.5. The pattern of the hardness distribution showed that the W1 weld metal hardness is overmatch the base metal with average 275 HV, while W2 and W3 weld metal hardness even match and undermatch the base metal hardness with average hardness 220 HV and 192 HV respectively. The hardness maps also showed that the softening behaviour occur in the HAZ. However, as mentioned above the hardness evident is not enough to assess the strength mismatch and most of the Engineering Critical Assessment (ECA) standards require yield strength overmatching based on tensile testing.

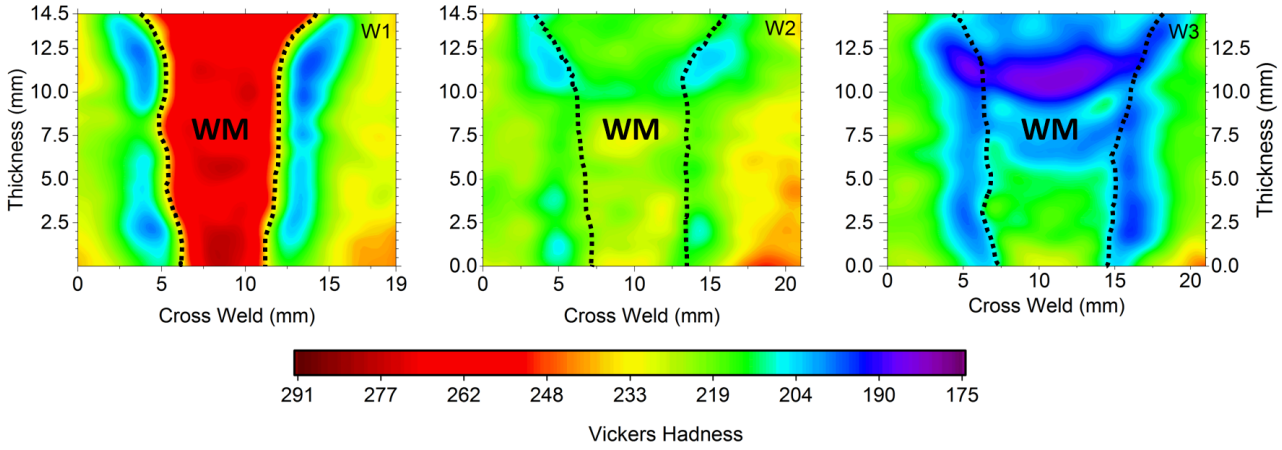

Figure 7.5: Hardness maps for the welded joints with different weld metal strength mismatching.

7.4.2 Weld metal microstructure

Due to the multi pass welding process that is utilized in pipeline joining, the weld metal microstructure through the joint is inhomogeneous and can be classified into as-deposited weld metal and reheated weld metal. The local properties depends on the phases present

in the microstructure of each zone. Figure 7.6 shows the weld metal micrographs near the cap pass for W1, W2, and W3 respectively, which are considered the as-deposited microstructure. As can be seen in the micrograph for W1, the dominant phase is acicular ferrite. The microstructure in specimen W2 is a combination of acicular ferrite and bainite and/or grain boundary ferrite. This is due to the chemical composition of the welding consumable used in this case. In specimen W3, the heat input was increased by 10%, which led to slow down the cooling rate, and as a consequence that promotes nucleation of grain boundary ferrite and polygonal ferrite at the expense of acicular ferrite.

Comparing the reheated weld metal micrographs shown in Figure 7.7 it is very difficult to distinguish between the deposited and reheated weld metals. Although, the hardness profile through thickness elucidate some variations in the hardness values as shown in Figure 7.8-b, it can be seen that as-deposited weld metal has higher hardness values compared to the reheated material. When comparing the hardness of W1 as-deposited to W1 reheated the hardness of the microstructures is measured to be 280 HV and 268 HV respectively. This is due to the minor changes in the microstructure due to the second thermal cycle applied by the subsequent passes. In addition, it was noted that as the heat input increased, the reheated weld metal fraction increased as in the case of specimen W3.

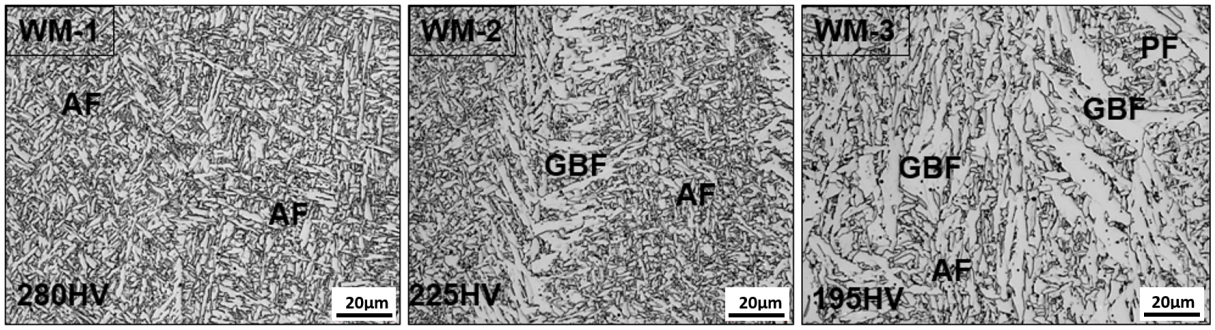

Figure 7.6: Optical micrographs shows the as-deposited weld metal microstructure near the cap pass.

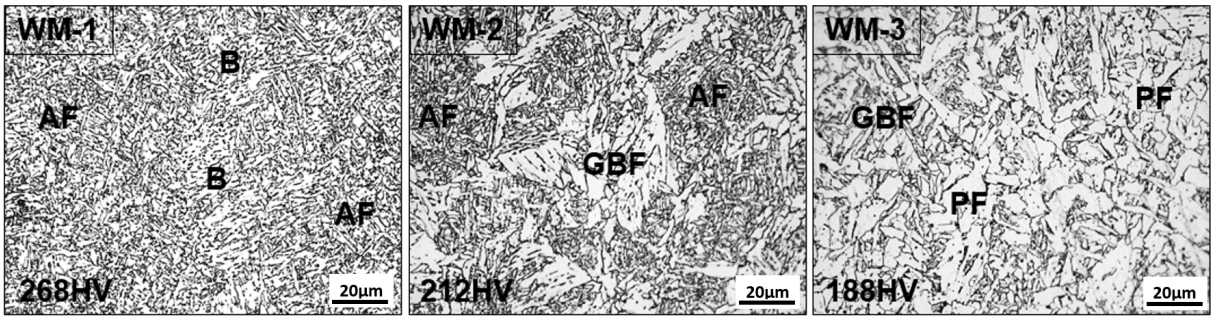

Figure 7.7: Optical micrographs shows the reheated weld metal microstructure near the bottom of the cap pass.

7.4.3 HAZ microstructure

Figure 7.9 show the CGHAZ micrographs for each weld metal. Even though, the base metal microstructure is the same for all conditions, the CGHAZ microstructures exhibit significant differences. This difference in the CGHAZ microstructure is attributed to the heat input variations. Note that W1 and W2 conditions have similar microstructure, while W3 condition exhibits a coarser structure. In addition, looking at the macrostructure

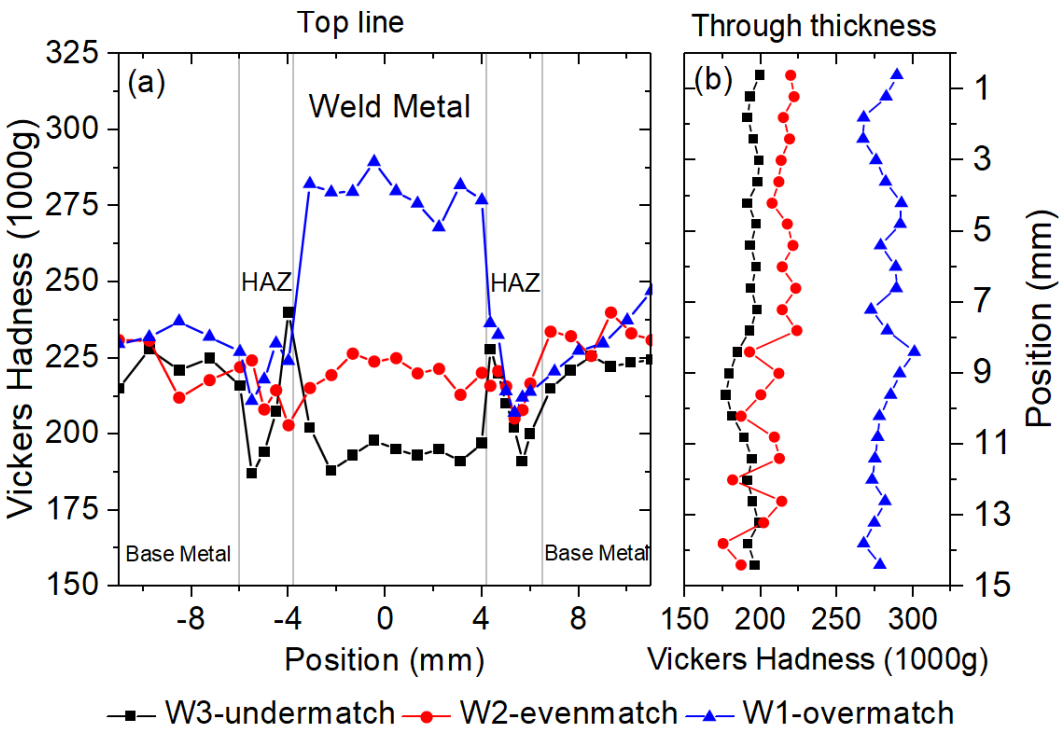

Figure 7.8: Hardness profile of W1-Overmatch, W2-Evenmatch, and W3-Undermatch a) Cross the weld, b) Through the weld.

graphs the size of the HAZ for W3 sample was wider, which is due to the higher heat input used to weld this condition. To investigate the phases in the CGHAZ in more details, the SEM was used as shown in Figure 7.10. The microstructure in the CGHAZ is a mixture of upper and lower bainite. Microconstituents such as martensite-austenite (MA) also can be seen around the prior austinite grain boundaries.

The FGHAZ shown in Figure 7.11, experiences a lower thermal cycle compared to the CGHAZ. The microstructure of the FGHAZ is a mixture of polygonal ferrite and MA microconstituents present at the grain boundary. The SEM analysis shows the details of the microstructure, indicating the dominent black phase is polygonal ferrite and the white

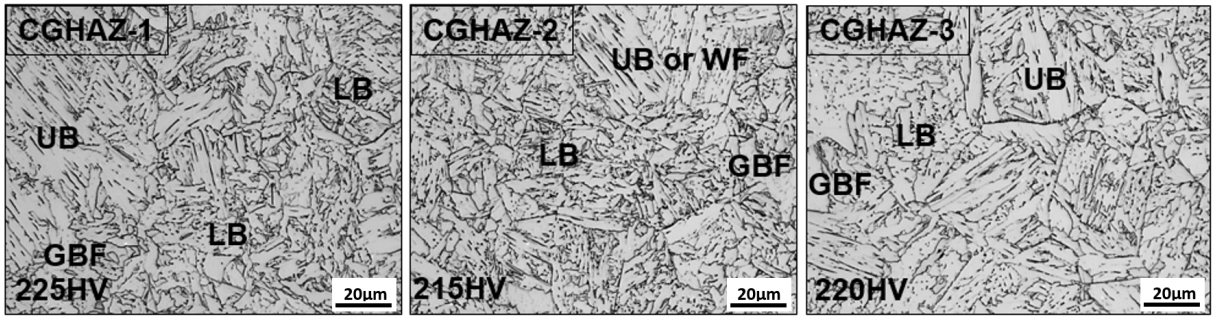

Figure 7.9: Optical micrographs shows the coarse grain heat effected zone microstructure.

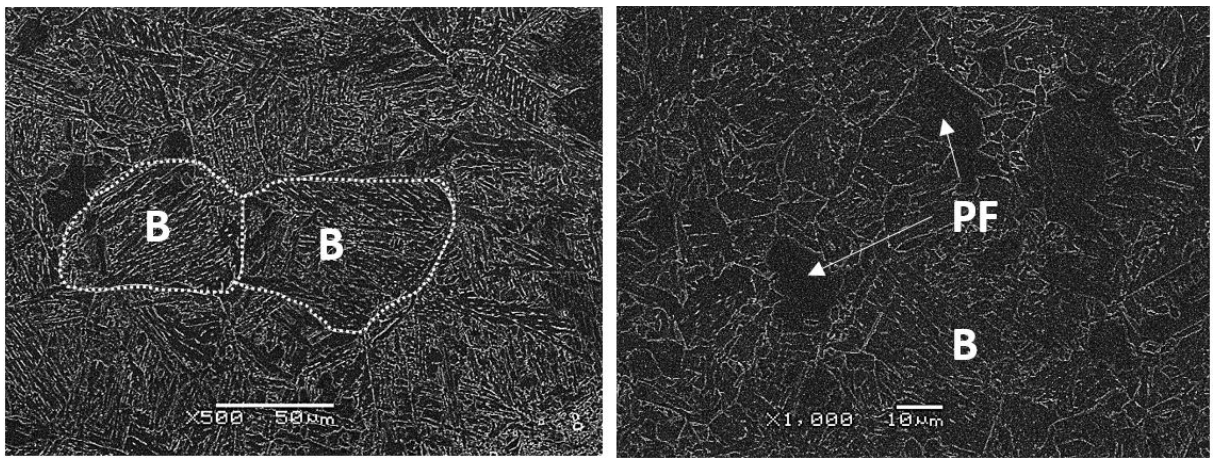

Figure 7.10: SEM micrographs shows the details of coarse grain heat effected zone microstructure for W1 at two different magnifications consist of bainitic microstructure along with polygonal ferrite microstructure.

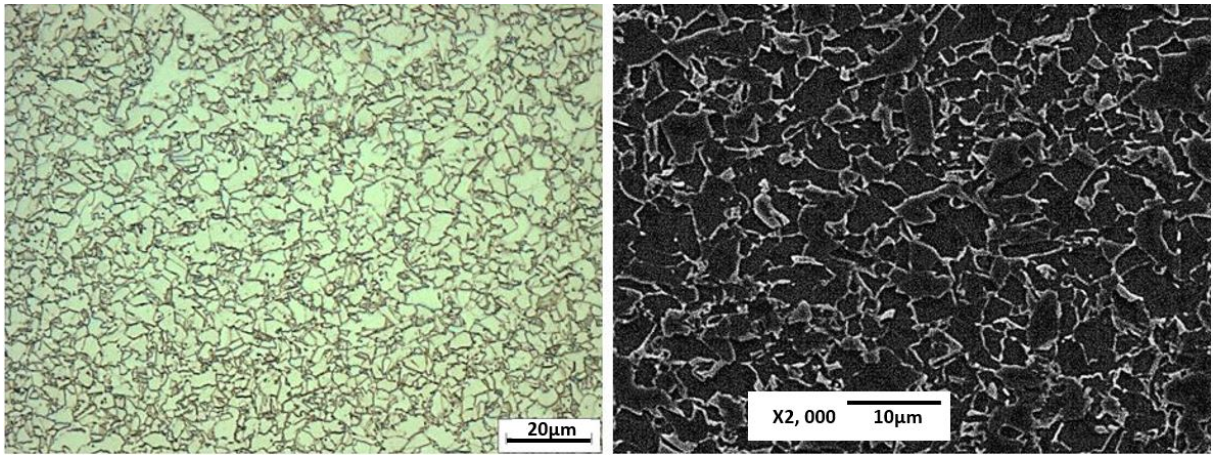

Figure 7.11: Optical and SEM micrographs show the details of FGHAZ microstructur.

micro constituents that appear at the grain boundaries are MAs. Looking at the hardness profile at the mid-thickness of the cross-weld section shown in Figure 7.8-a, softening in the FGHAZ can be observed. Liu *et al.* [96], studied the HAZ thermal cycle effect on the yield strength of different pipeline steel using a Gleeble simulator. They found that the minimum yield strength values were recorded for weld peak temperatures between (800 °C) and (1000 °C), which corresponds to the FGHAZ. Due to the strength mismatch between those two phases it is easy to form cracks in this kind of microstructure. Kang *et al.* [84] use in-situ SEM with DIC tensile testing to map strain for dual phase steel and showed that heat treatment could be performed to improve fracture properties and ductility. More information can be found in the article by Avramovic-Cingara *et al.* [9], and Kadkhodapour *et al.* [83].

7.4.4 Evaluation of strength mismatch using indentation test

An average of at least 20 instrumented indentation tests were performed in each zone for each specimen: W1, W2, and W3. The obtained average load-displacement curves for the WM, HAZ, and BM for each weld are shown in the Figure 7.12, 7.13, and 7.14 respectively. The HAZ curves exhibited the lower strength with higher deformation for all conditions. In the case of the weld metal, the average load-displacement curve for W1 sample showed higher strength when compared to the base metal, while W2 and W3 curves showed moderate and lower strength compare to the base metal curve respectively. Note that the base metal was indented in the cross section, which represents the hoop direction properties of the pipe. By using the cavity expansion model equation that was developed in Chapter 6, the yield strength for each zone in the cross section of the weld joint were estimated. To assess the strength mismatch the yield strength of the weld metal was compared with the yield strength of the base metal in both transverse (hoop) and longitudinal(long) direction of the pipe.

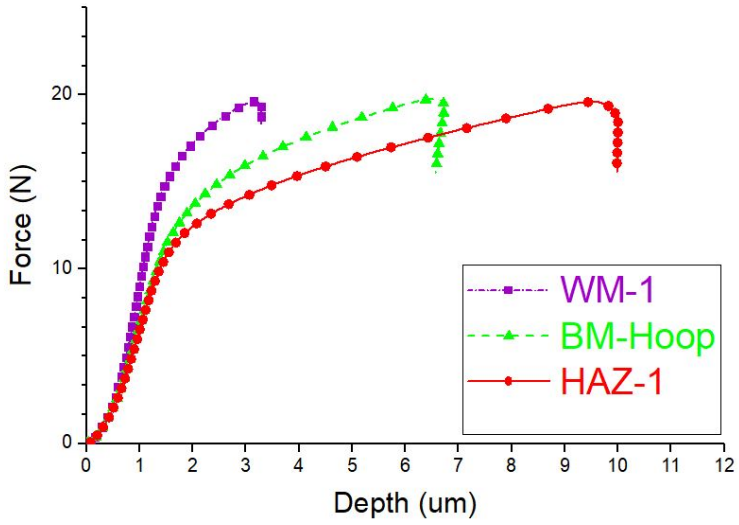

Figure 7.12: The average load-displacement curves for each zone across W1 sample.

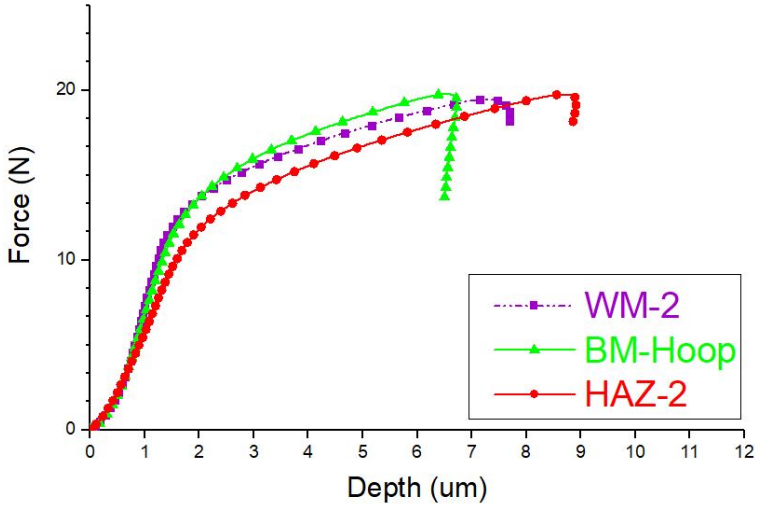

Figure 7.13: The average load-displacement curves for each zone across W2 sample.

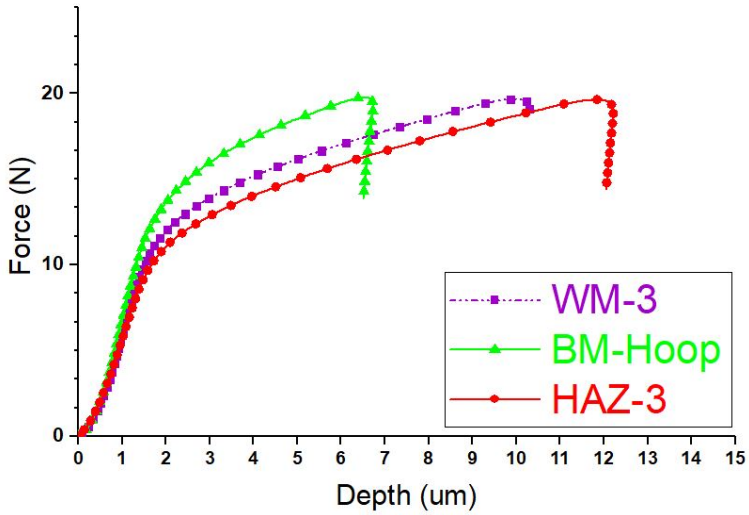

Figure 7.14: The average load-displacement curves for each zone across W3 sample.

Figure 7.15 shows the average load-displacement curves for each weld condition were compared to the average load-displacement curves of the base metal. The W1 sample exhibited the highest yield force compared to base metal in both directions; therefore, it is considered an overmatch condition. These observations are in agreement with the hardness measurements and the observed microstructure in each zone. In the case of W2, the average load-displacement curve showed a match with the base metal curve and this was considered as even match condition. On the other hand, W3 sample showed the lowest force at yield and the highest deformation compared with the base metal and was considered as under match condition. Using the equation suggested by the author of this thesis in Chapter 6, based on cavity expansion approach yield strength could be estimated. The indentation depth also correspond to the deformation in the microstructure for each weld. When comparing W1 sample has the lowest indentation depth, which is around

3 μm while W3 facilitated the highest indentation depth of around 10 μm. It should be noted that load-displacement curves for HAZ was an average of the curves in CGHAZ and FGHAZ.

The summary of the indentation yield strength for welds and base metal are presented in Table 7.3. It should be noted that the yield strength values was calculated from the average curves and at least 20 indentation tests were performed for each zone. When one considers the results of the yield strength measurements it can be seen that the minimum yield strength was recorded at the HAZ. However, the yield strength of the HAZ for W3 sample exhibited the lowest value, this could be attributed to the higher heat input used in this case, which led to severe softening in the W3-HAZ. By looking at the hardness profile and the microstructure in the W3 weld metal and HAZ, these findings could be confirmed.

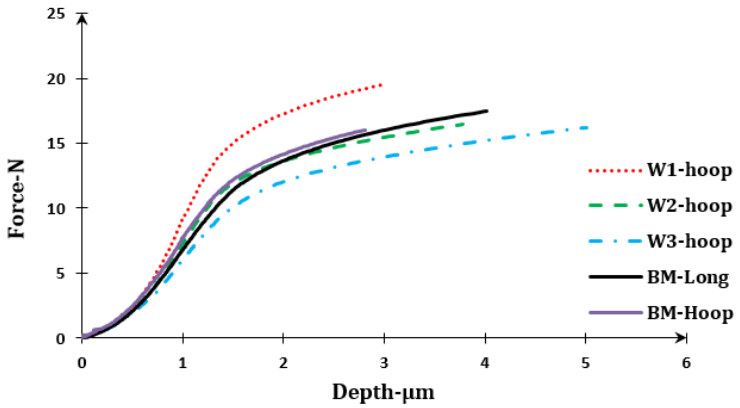

Figure 7.15: Load-displacement curves for weld metals W1, W2, W3, and X80 base metal

As mentioned above, the microstructure of the multipass weld is inhomogeneous and acicular ferrite microstructure might change to different microstructure due to the subsequent passes. It is proposed that the bulk properties of the weld metal could be measured

Table 7.3: Yield strength and strength mis-match values based on the indentation method.

Zone	W1-YS (MPa)	W2-YS (MPa)	W3-YS (MPa)
BM-Long	567±13	567±13	567±13
BM-Hoop	627±15	627±15	627±15
WM	683±28.3	590±38.2	493±17
HAZ	530±22	516±14	489±18.5
Mismatch-L%	20	4	-13
Mismatch-H%	9	-6	-21

by tensile test. However, the local weld properties could not be measured by conventional tensile test. Knowing the local properties is very useful in order to model the weld joint and study the effect of the variation of the local properties on the crack propagation in the crack tip opening displacement (CTOD) test. Therefore, the indentation technique was used to detect the differences in the local properties of the weld metal. The W1 sample was selected to measure the local properties through the weld joint. Figure 7.16 shows the load-displacement curves for as-deposited weld metal referred to as (DP) and reheated weld metal referred to as (RH) for the W1 specimen. Since the indentation system equipped with optical microscope, as-deposited and reheated zones were indented separately. As expected, the reheated weld metal exhibited lower yield strength values, which is consistent with the microhardness profile through the welds as shown in Figure 7.8-b and the observed microstructures in Figure 7.7.

7.4.5 Tensile test and DIC results

In this section, results of conventional tensile testing are presented and the yield strength for the weld metal for each weld will be discussed and compared with indentation test results.

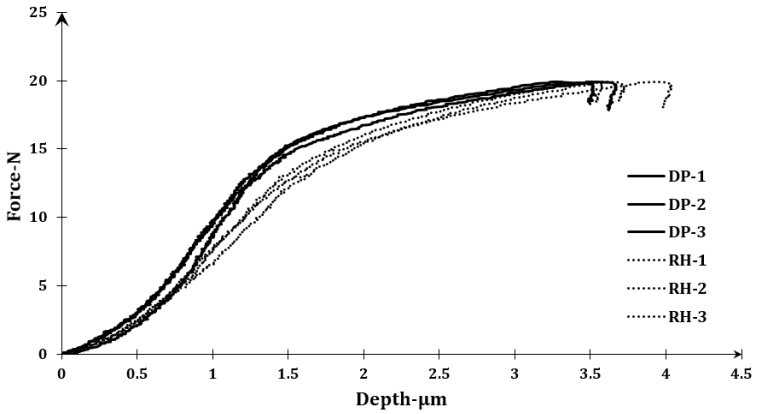

Figure 7.16: Load-displacement curves for W1 through the cross section show the different in the local properties between as deposited WM Vs. reheated WM.

The procedure of the samples extraction for all weld and cross weld was schematically explained in the methodology Chapter 3. To evaluate this further, a DIC system was used to map the strain up to the failure. In order to assess the strength mismatch properties, tensile testing was performed for the base metal in both directions transverse (or Hoop) and longitudinal (or Long). It should be noted that all yield strength values was defined as the stress at 0.5% longitudinal strain.

All weld tensile test results

Figure 7.17 shows the average engineering stress-strain curves for all weld metals compared to pipe base metal curves in the hoop and longitudinal directions. It can be seen that W1 sample exhibited the highest yield strength, which is 715 MPa and overmatchs the pipe yield strength in both directions, which exhibits a yield strength 665 MPa and 571 MPa in the hoop and the long direction respectively. In the W2 sample, the average tensile yield strength was 576 MPa, when compared to pipe yield strength values, W2 undermatch the

hoop yield strength of the pipe, but barely matches the long yield strength of the pipe. For W3 sample the average yield strength was around 485 MPa, which undermatchs the yield strength in both hoop and long directions of the pipe.

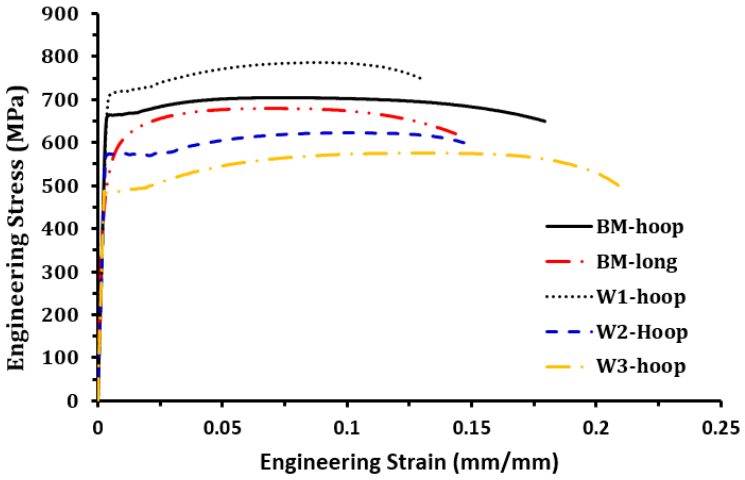

Figure 7.17: Engineering Stress-Strain curves for base metal and all weld metals.

To calculate the strength mis-match value, the DNV-OS-F101 standard recommends checking the overmatching properties for all material conditions, therefore it is requied to compare the weld metal properties with base metal properties in both direction and report the more conservative value [39]. However, the all weld metal tensile testing results represent the properties of the weld in the hoop direction. Therefore, Table 7.4 shows the yield strength and strength mismatch values for each weld compared to the pipe yield strength in both directions. When one compares the yield strength mismatch calculation using tensile testing versus indentation, it can be seen that both techniques provide similar results. However, indentation techniques provide more easily obtained local measurements compared to tensile testing. Therefore, it could be use as a quick tool to estimate yield

Table 7.4: Yield strength at 0.5% and strength mis-match calculation based on the tensile test method.

Zone	W1-YS (MPa)	W2-YS (MPa)	W3-YS (MPa)
BM-Long	550±8	550±8	550±8
BM-Hoop	657±6	657±6	657±6
WM	712±6	575±26	495±18
Mismatch-L%	29	4.5	-10
Mismatch-H%	8	-12.5	-25

strength mismatch for pipeline application. In addition, yield strength for narrow zones such as the HAZ or reheated weld metal can be determined easily, which is an advantage for the indentation technique.

Cross weld tensile test results

Tensile testing across the weld for each condition was performed. The engineering stress-strain curves are shown in Figure 7.18, where the trend in observed yield strength was as expected, in which the W1-cross sample exhibited the highest yield value with lower deformation, while in the case of W2 and W3, the deformation was almost the same, although the yield strength for W2-cross was higher than W3-cross. It should be noted that these stress-strain curves represent the global behaviour of the joint even thought the local properties are different. Therefore, the behaviour will be dominated by the weakest zone, which is the HAZ. By looking at the failure location for each condition as shown in Figure 7.19 it can be noted that as the weld strength overmatch increases, the failure is shifted towards the base metal as in the case of specimen W1. Hertele [65] conducted an FE study on the effect of strength overmatching on crack driving force and found that the

driving force of a flaw is reduced as the degree of weld strength overmatch increases. In addition, it was concluded that as the overmatching level increase, it can shield the WM and adjacent area (HAZ) from failure.

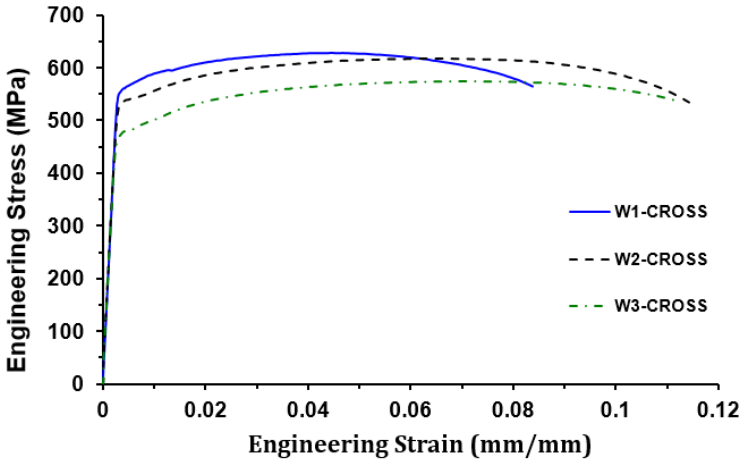

Figure 7.18: Global engineering Stress-Strain curves cross the weld metals.

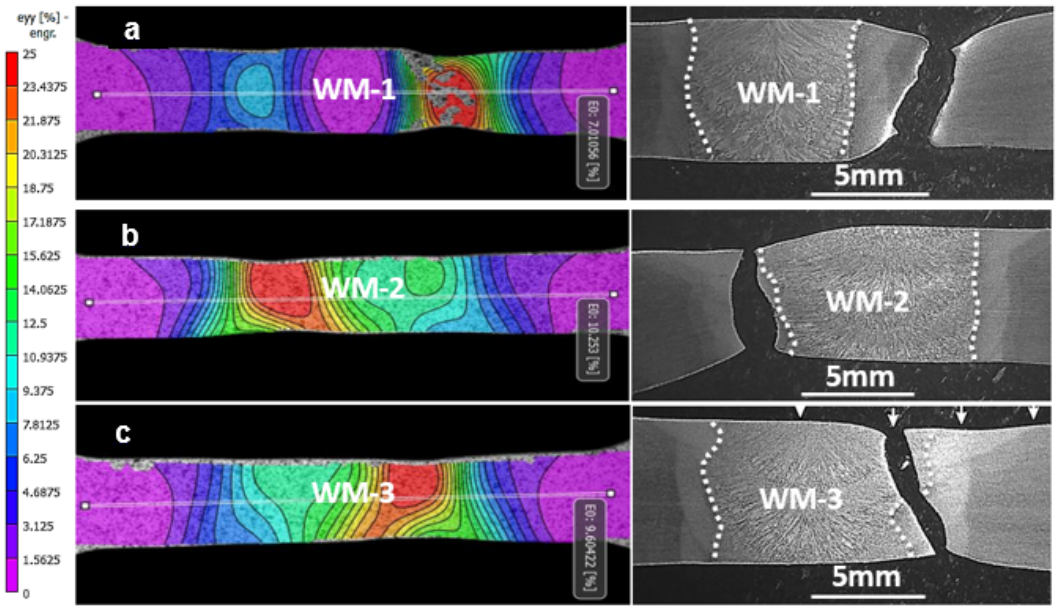

Figure 7.19: DIC strain maps with show the fracture location for cross weld samples A)- W1, B)- W2, and C)- W3.

The results from DIC strain measurements in Figure 7.20 show the strain distribution around the weld area for specimen W1. It is expected that the weld nugget would exhibit the highest yield; therefore, the minimum strain value was recorded in the WM, which was about 2% . In addition, the strain was localized between the HAZ and BM as shown in Figure 7.19-a. The strain map for specimen W2-cross shown in Figure 7.21, it can be seen from the map the strain in the weld zone increased by up to 25% and as the yield strength overmatch decreased, and the failure location shifted closer to the WM. The strain localized in the weld zone and failure location could be confirmed by comparing results in Figure 7.19-b. Finally, the strain distribution for the W3-cross is shown in the Figure 7.22. The strain values in this case was very similar to specimen W2. However, the failure initiated from the HAZ and propagates through the weld metal as shown in Figure 7.19-c.

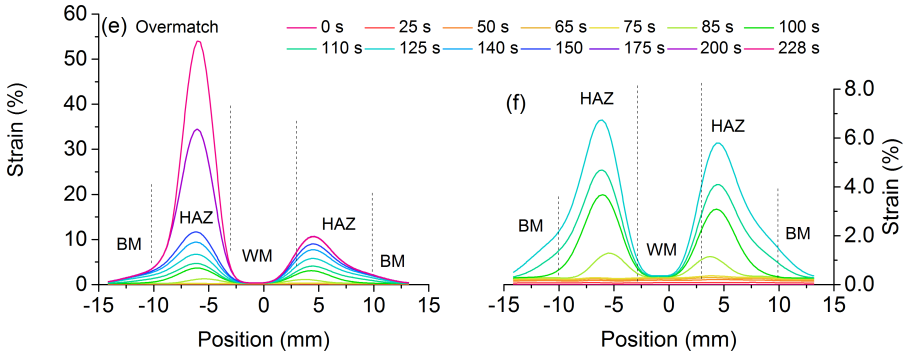

Figure 7.20: Strain distribution across specimen W1.

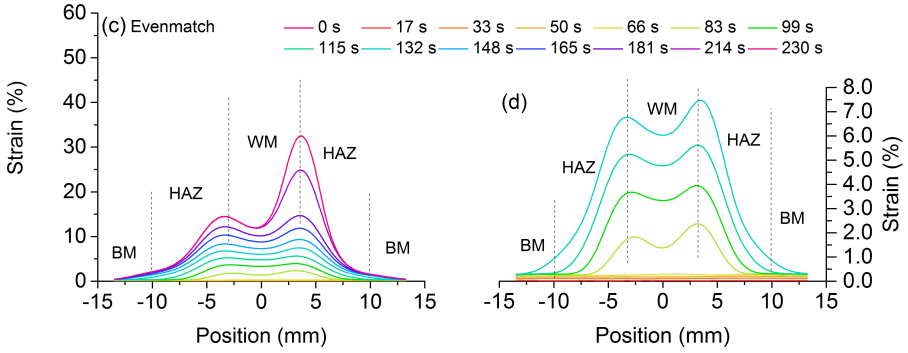

Figure 7.21: Strain distribution across specimen W2.

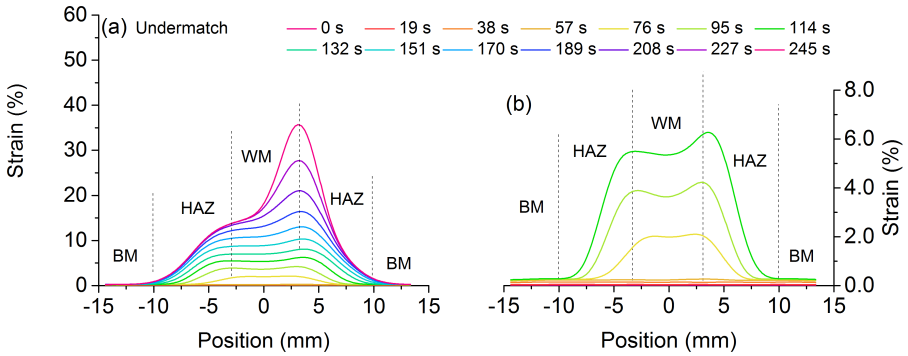

Figure 7.22: Strain distribution across specimen W3.

7.5 Summary / Remarks

In summary, this chapter showed that the nearly flat instrumented indentation can be used to assess the yield strength mismatch in pipeline welds. The results were correlated well with the observed microstructure and micro-hardness measurements. Local properties of different microstructural regions in the weld metal such as reheated versus as-deposited weld metals were also investigated using the indentation approach. The results indicated that the reheated weld metal exhibited lower yield strength and this could be attributed to the effect of subsequent tempering of the weld passes at high temperature, which leads to changes in the microstructure and consequently affects the mechanical properties. The strength mismatch was calculated using both indentation test and tensile test. It should be noted that the yield strength mismatch was calculated using the all-weld-metal properties, which represents the properties of the weld in the hoop direction of the pipe. Cross-weld tensile testing were performed, and the results support the indentation findings. In addition, the strain distribution give further details about local properties and effect of strength mismatch on the failure location. However, due to the difficulty of performing the tensile testing for the weld metal parallel to the pipe axis, it is recommended to develop a procedure to investigate the properties of the weld metal in different directions and consider the most conservative approach to describe strength mismatch. This will be particularly important for the strain based design approach that is usually used in the pipeline application, which takes into account the high axial strains that is imposed during the pipe installation or during service. Therefore, the future effort will focus on developing a methodology to investigate the weld properties in different directions.

Chapter 8

Characterization of Anisotropic Properties of API-X80 Line Pipe Welds by Means of Instrumented Indentation Techniques

8.1 Overview

Isotropic behaviour is usually assumed in line pipe specification especially when the design is based on strain criteria. However, during a pipe manufacturing processes, such as UOE (Steel plates are formed into a U shape and subsequently into an O shape then seam weld), this may not be the case. In addition, most of the welding processes such as GMAW create

residual stresses attributed to the thermal expansion and contractions, which may lead to anisotropic behaviour in the weld metal. In this work, instrumented indentation technique with a nearly flat-tip indenter was used to measure the yield strength for API-X80 line pipe welds. Using this technique the yield strength can be measured directly from the load-displacement curves as demonstrated in the previous chapters. Given the convenience of the indentation technique the yield strength of the weld metal was measured in two directions, namely the transverse and longitudinal directions, and the results indicated that the weld metal has anisotropic properties, which could lead to a non-conservative estimate of strength mismatch. The indentation results were compared with conventional tensile test results for all-weld metal and cross-weld specimens.

8.2 Background

There are many challenges for line pipe steels including homogeneity of the microstructure, mechanical properties, and weldability [80]. The TMCP manufacturing process along with the pipe making procedure, such as UOE process usually creates anisotropy in the linepipe steels. The longitudinal direction of the pipe in most cases has a lower yield strength compared to the transverse direction of the pipe. Due to induced strains during the manufacturing process [80, 129]. Characterizing heterogeneous microstructures like pipeline welds using conventional methods such as tensile testing becomes more difficult when a narrow groove design is used. It is impractical to machine full samples from narrow zones for instance HAZ or reheated zones in the weld to perform tensile test. In addition, most of the strength mismatch calculations rely on an assumption of isotropy in the weld

due to the difficulty in determining the properties of the weld in the other directions [66, 81], though the properties of the weld in both direction does not necessary have to be isotropic. Zhang *et al.* [161] developed a notched cross weld tensile testing method to determine the true stressstrain curve for each material across the weld zone. The procedure is based on notch dimensions, which are calibrated in order to identify the weld metal parallel to the pipe axis. Bowker *et al.* [81] developed the methodology further by using FE modelling in order to obtain the tensile properties across the weld for X70 and X100 line pipe steels. However, the proposed procedure requires the use of FE computation in order to calibrate the sample dimensions and infer the results, which is a considerable drawback of this method. Therefore, alternative techniques should be developed to estimate weld metal local properties in different directions, which can improve the computational approaches by giving accurate data without any assumption or finite element use. In addition, it is vital to verify the properties of the weld in different directions to determine the validity of the isotropic assumption.

Another approach, involves the application of DIC to map strain across the weld. By assuming an iso-stress condition the strain maps could be used to construct indvidual stress-strain curves for different zones across the weld. For instance, Lockwood *et al.* [98] utilized DIC measurements along with an iso-stress condition to characterize the mechanical response for different zones of an aluminium friction stir weld, and developed an FE model to verify the experimental results. In 2006 Yan *et al.* [151] use same technique to characterize the heterogeneous microstructures in a X100 pipeline steel weld, in order to identify the mechanical behaviour of the local zones around the weld metal. Saranath *et al.* [130] also conducted study aimed at characterizing the local properties of different HAZ

regions in a bead on plate weld on a mild steel sheet. The results were correlated with the microhardness measurements in order to optimize the welding parameters.

In the present work the nearly flat tip instrumented indentation technique were utilized for X80 pipeline welds to assess the weld metal yield strength in different directions. The estimated yield strengths were compared with the local yield strength values at a 0.5% strain level that was obtained by tensile testing in both directions of the weld. The DIC strain maps were used to extrapolate local stress-strain curves for weld metal in both directions. The aim of this chapter is to highlight the importance of using such a technique to characterize the weld metal properties, and determine a method for obtaining yield stress values that provide engineers with more accurate safety margins when strength mismatch is considered. The overmatching condition W1 from the previous chapter was selected since it is usually the case in pipeline weld. In addition, the weld metal was characterized in both the longitudinal and transverse direction (hoop) using SEM and microhardness mapping technique to correlate the microstructure morphology with the yield strength measurements obtained by indentation using a nearly flat indenter and DIC local stress-strain curves.

8.3 Experimental procedure

To investigate the anisotropic properties of the weld the instrumented indentation technique was used to indent the weld microstructure in both directions. Figure 8.1 shows schematically the procedure that was used to prepare the samples to investigate the mechanical properties of the weld metal in both directions, in which the W1 specimen was

selected for this purpose. For more details regarding the welding parameters and procedure see Chapter 7. Figure 8.2 shows the 3D macrostructure for W1. The weld metal was indented parallel to the welding direction, which represents the strength and hardness in the hoop direction and perpendicular to the welding direction, which represents the strength and hardness in the long direction.

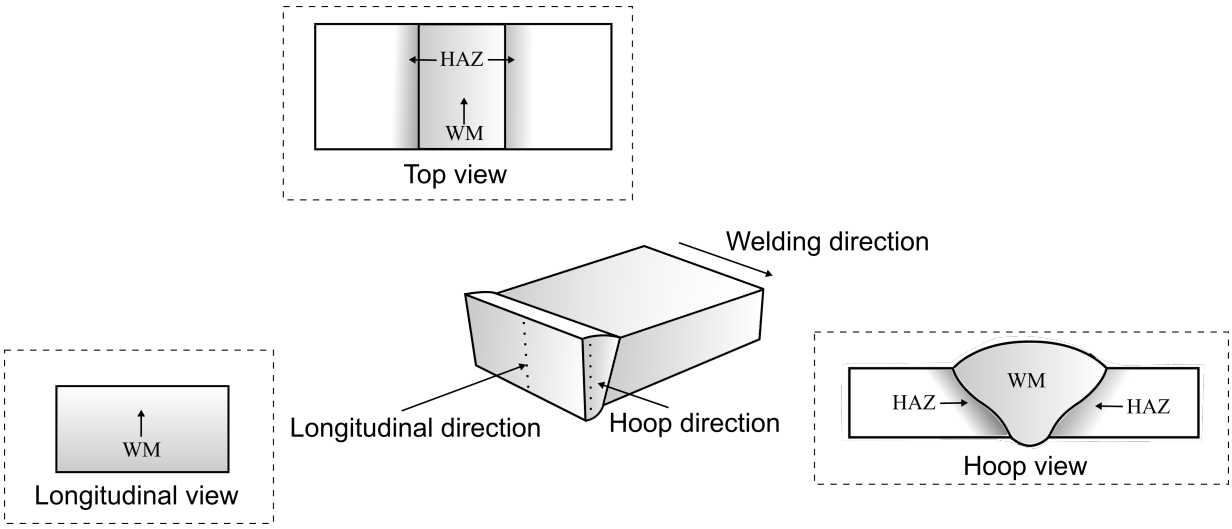

Figure 8.1: Schematic diagram shows the indentation sequence to investigate the properties of the weld in different directions.

In order to map strain across the weld, a DIC system was used, which allows one to examinethe behviour of different zones across the weld when the same loading is applied. The DIC system was combined with a tensile test frame and the deformation in the sample was recorded at the same rate of data acquisition as the frame load and displacement. This allowed one to construct individual stress-strain curves for indvidual zones across the weld based on the iso-stress assumption as described in prior work [98, 126, 151]. Figure 8.3, visualizes the iso-stress assumption in more detail.

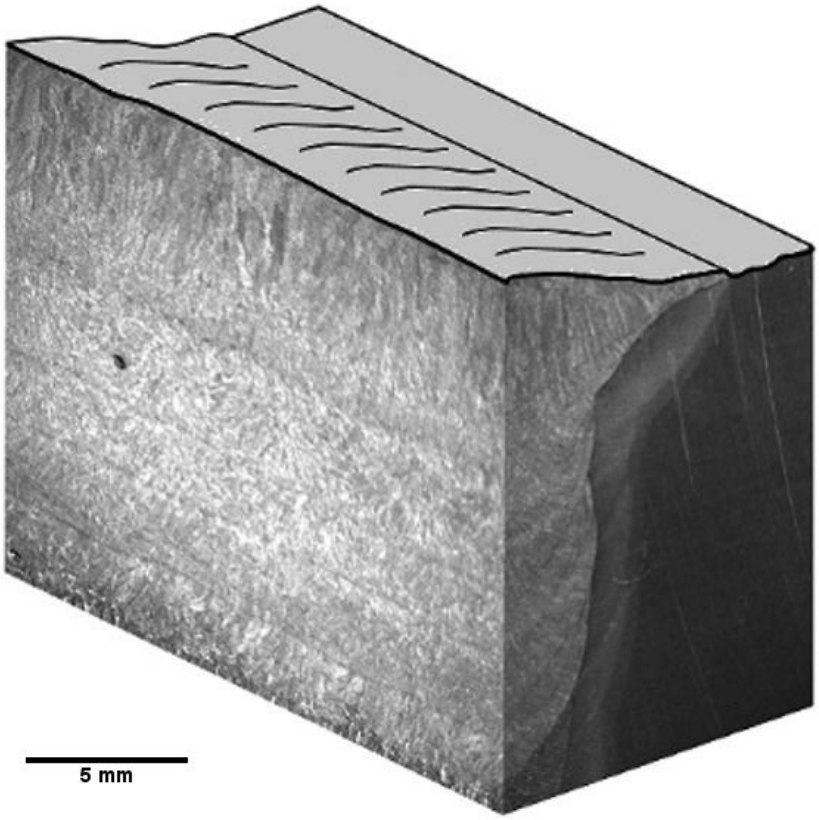

Figure 8.2: 3D macrograph shows the weld metal structure for W1 from both direction to investigate the microstructure and the properties of the weld in different directions.

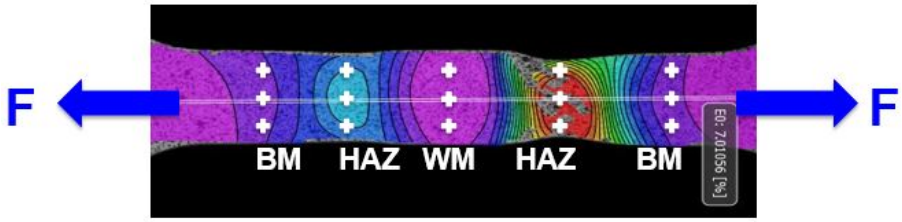

Figure 8.3: Cross weld Strain map shows the iso-stress assumption and the strain localization for each zone across the weld, the plus signs represent the points were selected to average the strain in each zone.

8.4 Results and discussion

8.4.1 Nearly flat tip indentation results

At least 15 indents were performed in each weld direction, the load-displacement curves of the weld metal in both directions were compared as shown in Figure 8.4. The weld metal in the hoop direction exhibited higher yield strength, which is about 683±28.3 MPa compared to the longitudinal direction of the weld, which record a yield strength 631±22 MPa. When one look at the final indentation depth hoop direction of the weld exhibited lower depth compared to the longitudinal direction of the weld, which is consistent with the yield strength values obtained by the indentation technique. However, the indenter shape is not a standard shape to determine hardness value such as Vickers indenter or Brinell indenter; therefore, this behaviour will be discussed later in the hardness section.

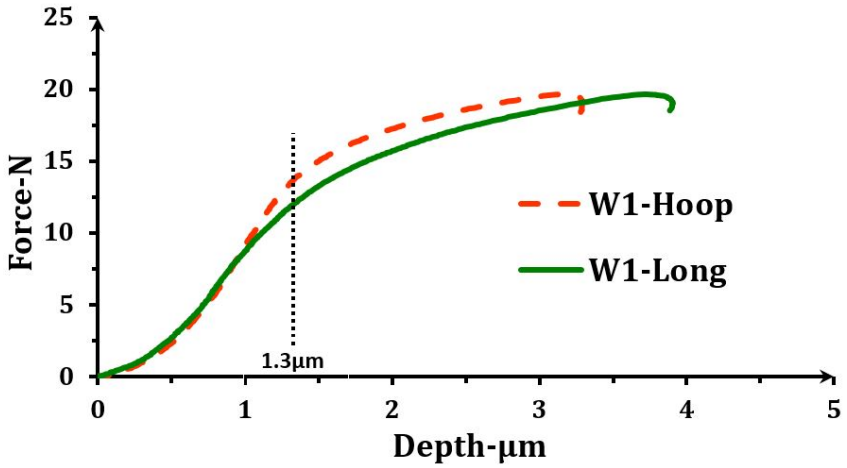

Figure 8.4: Load-displacement curves for the weld metal in both directions.

8.4.2 Tensile test

To compare the indentation results to conventional tensile test results, all weld metal and cross-weld tensile samples were prepared as explained in the methodology Chapter 3. The DIC system was used to map the strain and construct the individual stress-strain curves for each zone across the weld sample. Figure 8.5 shows the average engineering stress-strain curves for the all weld metals compared to base metal in both hoop and longitudinal directions, which is usually used in order to evaluate the strength mismatch properties for pipeline welded structures. It can be seen that the weld metal has the highest yield strength, which is around 715 MPa and overmatches the base metal in both directions, which has yield strength of 665 MPa in the hoop direction and 575 MPa in the longitudinal direction. However, the all weld metal tensile testing represents the properties of the weld in hoop direction of the pipe or along the welding direction.

Therefore, to identify the properties of the weld metal in the longitudinal direction of the pipe, an iso-stress condition was assumed in this work to determine the properties of the weld metal in the longitudinal direction of the pipe, as described in the experimental procedure above. Figure 8.6 shows the stress-strain curves for different zones across the weld, which are WM and HAZ. The results indicate that the weld metal yield strength is around 600 MPa with low total strain values, while the heat effected zone exhibited the lowest yield strength of around 564 MPa. This softening in the HAZ leads to strain localization in the HAZ, which reached 12%. Note the weld metal yield strength in this case represents the yield strength of the the weld metal in the longitudinal direction (or long direction). Figure 8.7, shows the comparison between indentation curves (a) and local

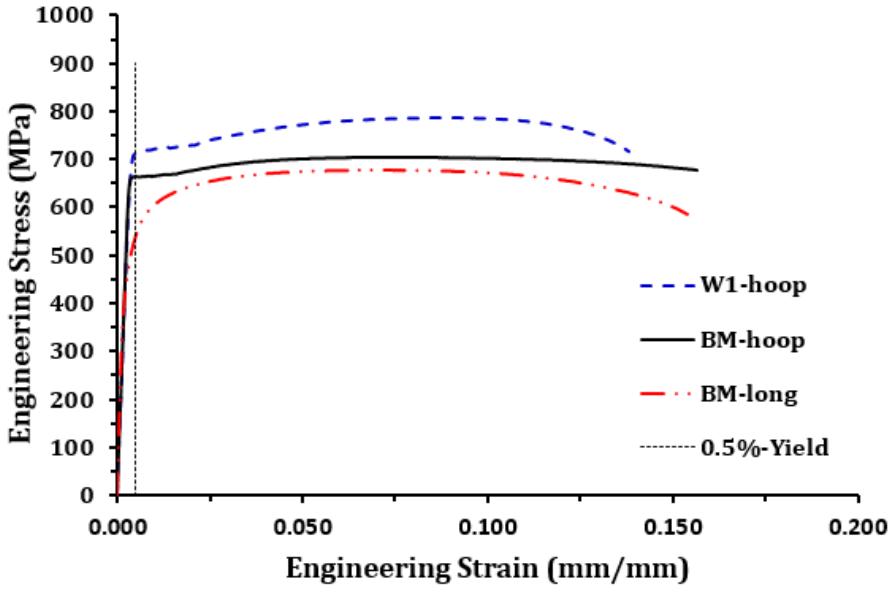

Figure 8.5: Engineering stress - strain curves for base metal and all weld metals.

stress-strain curves (b) in both directions for the weld metal. Note that 90% confidence intervals were calculated for each data set and the bounds were very tight; and therefore, not shown in the graphs. When comparing the indentation results with the tensile test results qualitatively in both directions, the difference in the yield strength can be seen clearly. This anisotropic behaviour in the yield strength could lead to a non-conservative estimate when strength mismatch is considered. The summary of the yield strengths based on the nearly flat indentation technique and tensile test are presented in the Table 8.1. The maximum relative difference between the indentation and tensile test results was 4.1% for the welds and 4.6% for the base metal.

The overmatch in specimen W1 can now be computed using the longitudinal tensile test data giving (600/550) or 9%. Likewise, the overmatch measured using the indentation

data in the longitudinal direction gives (631/567) or 11%. The latter values are almost half the values of the overmatch computed using conventional practices as shown in Table 7.4 for tensile test data and Table 7.3 for indentation data in Chapter 7. The latter is the most important result of this thesis conventional practice for estimating the strength mismatch in welds may lead to a non-conservative estimate.

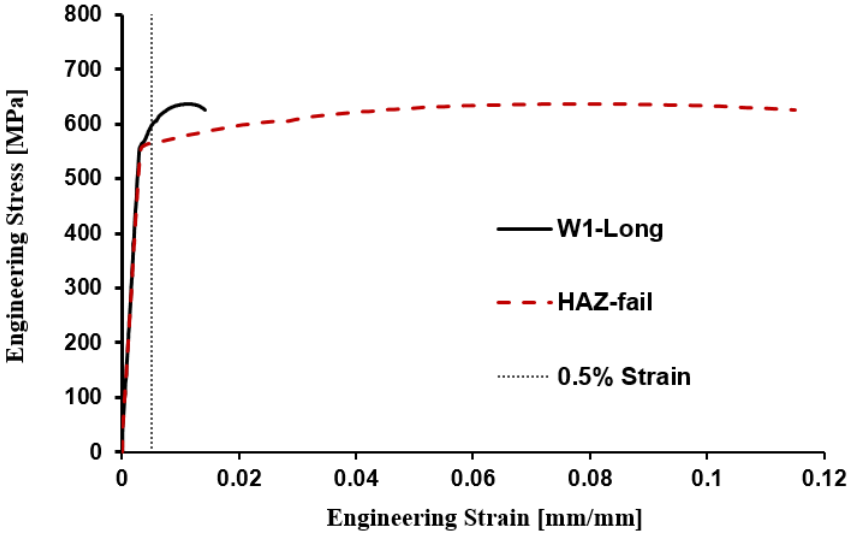

Figure 8.6: Local engineering stress-strain curves for the weld metal, base metal, and heat effected zone across W1.

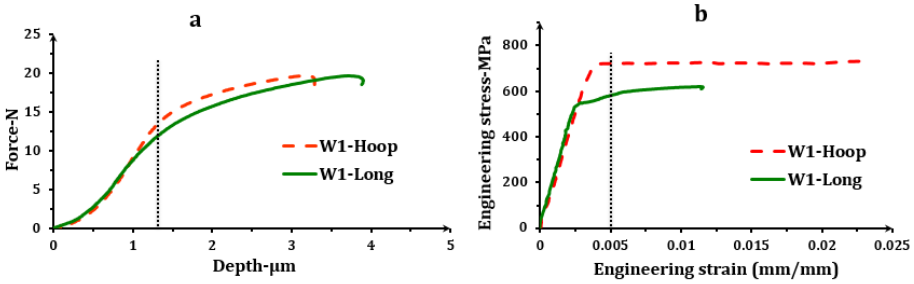

Figure 8.7: Comparison between properties of the weld metal in two different directions. a- Nearly flat indentation load-displacement curves, b- Tensile tests.

Table 8.1: The measurements of the yield strength for the weld metal and base metal in both directions using indentation test and tensile test along with strength mismatch calculation.

Zone	Hoop direction			Long direction		
	Ind.(MPa)	TT (MPa)	R.diff (%)	Ind. MPa)	TT MPa)	R.diff (%)
Weld-1	683±28.3	712±6	4.1	631±22	600±14	2.8
BM	627±15	657±6	4.6	567±13	550±8	3.1

[a] Ind. refers to the instrumented indentation test
[b] TT refers to the tensile test, note that tensile test for BM was reported from the previous Chapter.

8.4.3 Microstructure

To investigate the contribution of microstructure morphology to the anisotropic behaviour in the weld metal, detailed SEM imaging were performed as shown in Figures 8.8 and 8.9. The SEM micrographs were taken at similar locations and high magnification, in order to evaluate any grain size difference between both directions of the weld metal. Since the grain size can contribute up to 70% to the yield strength of these steels as reported in the literature [101, 103], this may have a major influence on the apparent strengths measured. Based on the qualitative appearance of the SEM micrographs, the hoop direction microstructure exhibited a finer structure compared to the longitudinal direction. However, it is very hard to estimate grain size by naked eye. Therefore, the ASTM-EE112-13 standard was used based on Jeffries procedure to determine the average grain size of the acicular ferrite microstructure [8], by treating individual needles of acicular structure as separate grains. The idea here is to calculate the average number of laths or grains per area, since this will correlate well with strength due to the Hall-Petch effect. Doing so, allows one to calculate the contribution of grain size on the yield strength based on the Hall-Petch relationship. To calculate the number of grains in specific area, based

on the Jeffries method, one applies the following formula:

$$N_a = \frac{1}{A} + [N_{inside} + \frac{N_{edges}}{2}] \tag{8.1}$$

where N_a is the total number of grains in specific area, A is the area of the image, N_{inside} is the number of the grains that completely inside the image area, and N_{edges} is the number of the grains that lay on the image edges, which count as half a grain.

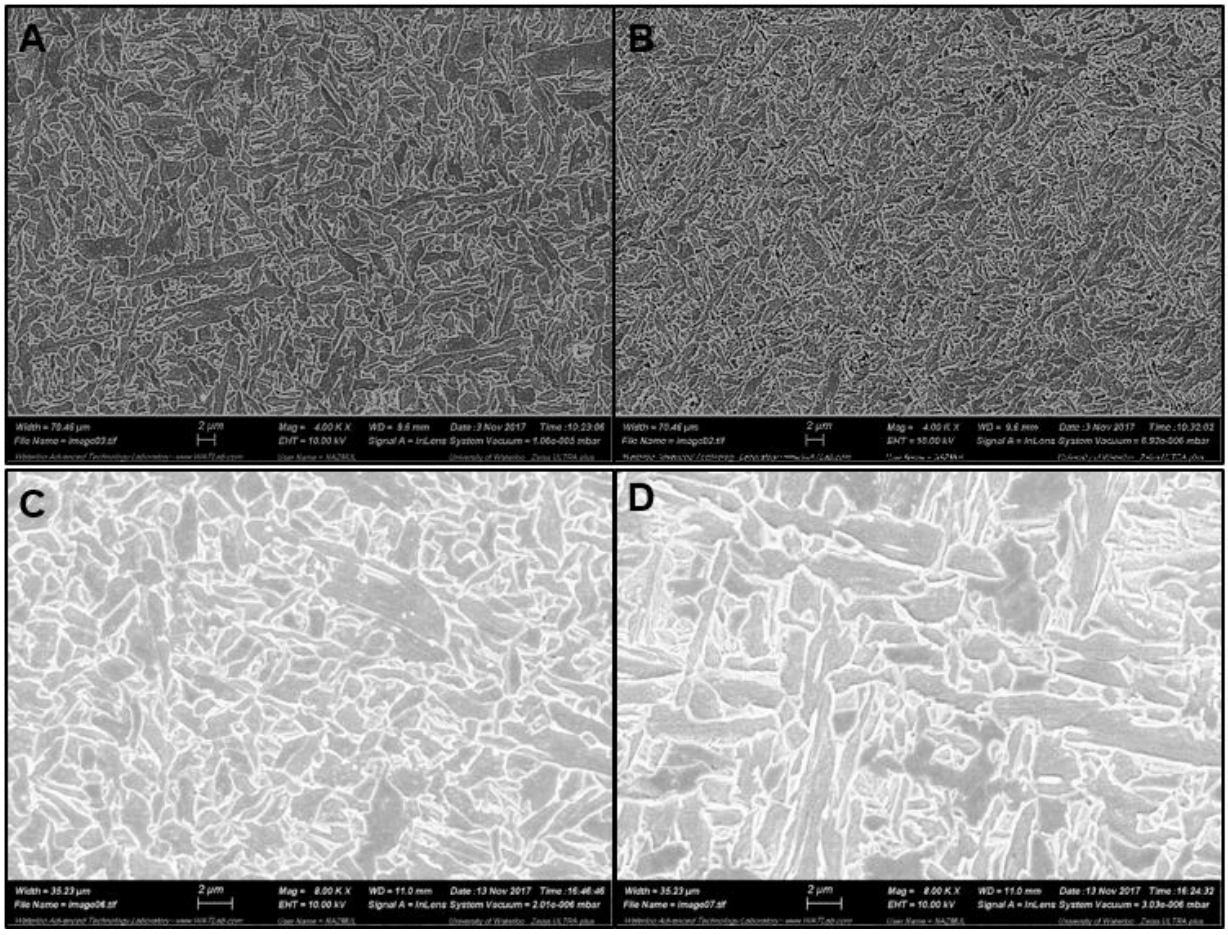

Figure 8.8: SEM micrographs shows as-deposited microstructure of W1 weld metal in the hoop direction.

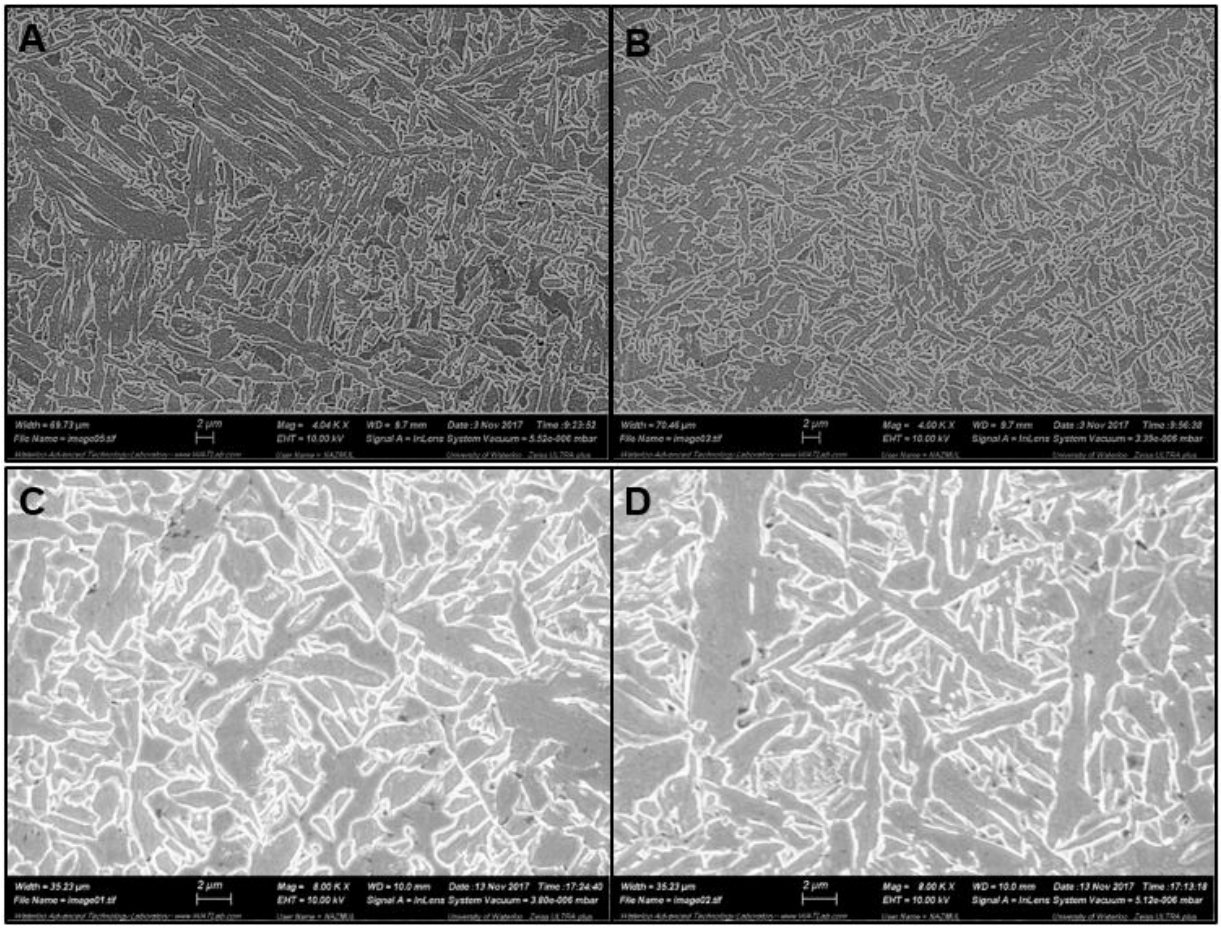

Figure 8.9: SEM micrographs shows as-deposited microstructure of W1 weld metal in the long direction.

Therefore, at least eight SEM images were taken and analyzed in order to determine a representative estimation of the average grain size. The bar charts in Figure 8.10 show the number of grains in each SEM micrograph, which indicate that the hoop direction contains more grains than long direction of the weld. To calculate the average effective grain size

d_{avg} the following formula should be used:

$$d_{avg} = \frac{1}{\sqrt{N_a}} \tag{8.2}$$

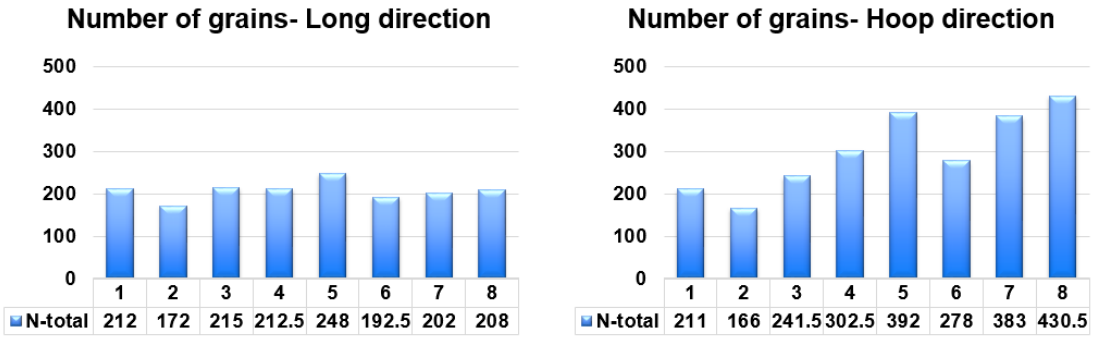

Figure 8.10: Bar charts show the grains measurements for weld metal in both directions based on the SEM images. Note that SEM images were all captured at 8000 times magnification, correlating to an area of 840 μm^2 for each micrograph.

Table 8.2: The grain size measurements and corresponding contribution to the yield strength for the weld metal in both directions.

Direction	Long direction	Hoop direction
N_{total}-[Grains]	1662±22	2404±91
N_a-[Grains/μm^2]	0.2466±0.023	0.3615±0.11
d_{avg}-[μm]	2.019±0.095	1.726±0.28
σ_y-[MPa]	476-523	515-566

[a] σ_y is the yield strength based on the grain size contribution. Note that σ_y was calculated using Hall-Petch relationship $\sigma_y = K_y \times {d_{avg}}^{-0.5}$.
[b] K_y is the strengthening coefficient for grain size 21.4-23.5 MPa.mm^2 [100, 101].

As shown in Table 8.2 the small change in grain size will have an effect on the yield strength, and the maximum difference between both directions is about 39-42 MPa. How-

ever, based on the indentation and tensile test results the difference between the hoop and longitudinal direction yield strength reached 100 MPa. Therefore, other factors such as the presence of residual stress could contribute to that difference.

8.4.4 Microhardness

The cross section and the longitudinal section of the weld were prepared in order to map the hardness and determine its variation within the weld metal zone and between the two directions of the weld. The hardness maps in both directions are shown in Figure 8.11, the cross section of the weld (hoop direction), which includes WM, HAZ, and BM showed higher hardness values in the weld zone compared to the longitudinal direction of the weld. This difference in the hardness could be attributed to the microstructure variation and the grain size difference.

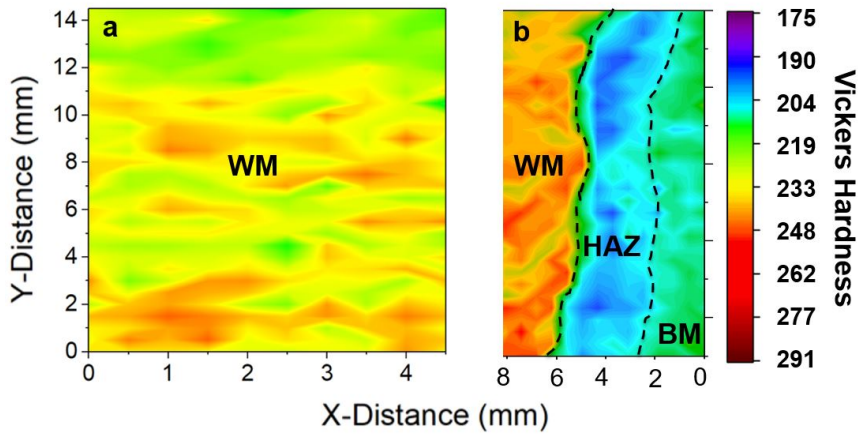

Figure 8.11: Hardness map for W1, a)- Longitudinal direction (long), b)- Transverse direction (hoop).

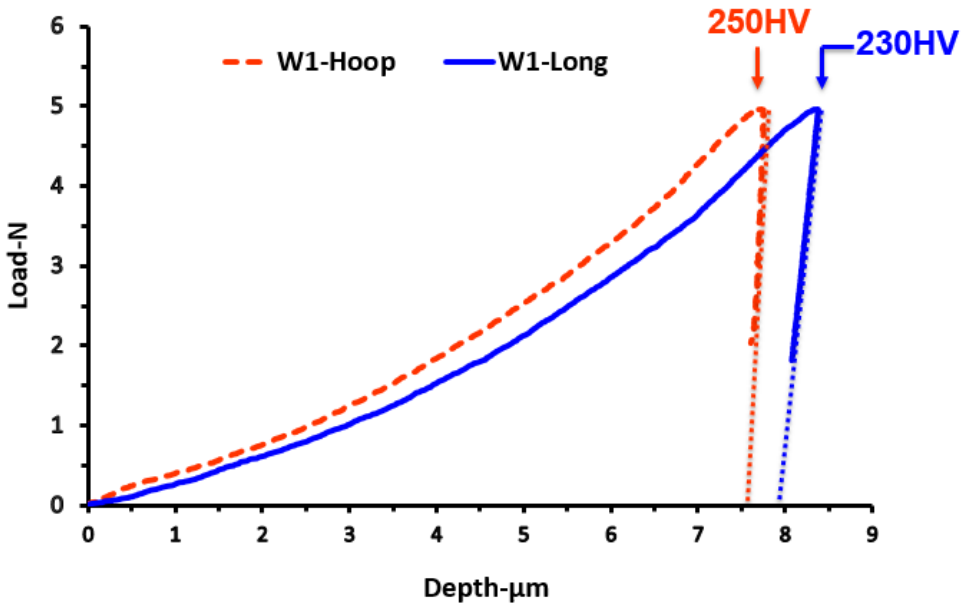

Figure 8.12: Average instrumented indentation hardness test for W1 in both directions.

To see the difference in the microhardness an average load-displacement curves were extracted as shown in Figure 8.12. The increase in the slope and the maximum penetration depth indicates that the hardness of the weld metal in the longitudinal direction decreased. The average hardness measurements revealed a 20 HV difference between the hoop and longitudinal direction. The microhardness maps and microstructure analysis showed good agreement with the measurements of yield strength in both directions. One may also argue that other factors could contribute to this difference in hardness.

8.5 Summary / Remarks

In summary, the yield strength anisotropic properties were characterized by means of a nearly flat instrumented indentation technique. Local tensile test also was performed utilizing DIC technique. The yield strength measured by indentation were also compared with the tensile testing results and the agreement between indentation yield strength and 0.5% tensile yield strength was excellent, the magnitude of the relative error in the estimated yields is bounded by $4.6 \pm \%$. Based on these results, assuming isotropic properties for weld metal can lead to use a non-conservative value of the strength mismatch. The microstructure analysis showed that the grain size contribute to this difference in the yield strength. The microhardness profiles also support this findings. The contemporary practices to estimate strength mismatch of the welds may lead to non-conservative estimates. This work highlighted the importance of developing new techniques to characterize the local properties of the welded structure. In the future, it is worth investigating the residual stresses state in both directions of the weld metal, which may contribute to this behaviour.

Chapter 9

Comprehensive conclusion

In conclusion, this work presents a novel technique to estimate yield strength for engineering alloys. The technique was developed and validated using FEM. Validation focused on X80 pipeline steel welds in order to evaluate the strength mismatch properties. Also, by evaluating the local properties within the weld region such as-deposited and reheated zones, it could be used as an input for FE modelling to provide more accurate predictions from the simulations. The unique shape of the indenter allows estimation of the yield strength value directly from the experimental load-displacement curve without any assumptions or empirical fits. The cavity expansion theory and slipline theory were used to estimate the yield strength based on the indenter geometry and the experimental load-displacement curve. Since the indentation test is a compression test by nature; the assumption of yield strength isotropy was confirmed by performing tensile and compression tests for two different engineering materials: which are X80 line pipe steel and AA-6463 aluminum alloy. The results showed that the assumption is valid.

The inverse approach was proposed as a method to estimate the stress-strain curve based on fitting approach called Efficient Global Optimization (EGO). The experimental load-displacement curves were used as a reference curve and resultant stress-strain curves were validated using conventional stress-strain data. Prior knowledge about the hardening model, hardening parameters bounds, and initial values was required to run the inverse approach. In addition, assumption of the machine stiffness and the indenter rigidity assumption were investigated to check the effect of these assumption on the load-displacement curve. The results showed that up to a load of 20 N, the machine and indenter could be assumed as a rigid body and it is elastic deformation could be neglected.

In order to validate the new developed technique and use it for real welding situations, different X80 pipeline welds were produced using a GMAW robotic welding. The welding parameters were designed to produce different microstructures and as a consequence different mechanical properties, which allow one to check the sensitivity of the indentation technique and evaluate the method accuracy to measure the mechanical properties. The microstructure and microhardness were also investigated. The results showed a strong relationship between the formed microstructure and measured microhardness maps. For example, the overmatched weld condition, which has higher carbon equivalent composed of more acicular ferrite; therefore, the hardness increased and the strength of the weld also increased. Meanwhile, in the undermatched condition, lean wire was used and the heat input was increased to slow down the cooling rate and reduce the formation of acicular ferrite, which reduced the hardness and yield strength in the weld versus the base metal. Doing so allows evaluation of the indentation technique in different weld metal strength ratios to validate the method for strength mismatch assessment. The yield strength mea-

sured by the indentation technique for different pipeline welds were also compared with the tensile testing results and the agreement between indentation yield strength and 0.5% tensile yield strength was excellent, the magnitude of the relative error in the estimated yields is bounded by 4.6%.

Furthermore, the indentation technique allows one to estimate the strength in different directions of the weld to assess the isotopic behaviour. The results indicate the weld metal exhibits anisotropic behaviour. These findings were supported by local stress-strain curves for the weld metal obtained by DIC. These observations demonstrate the importance of developing such a technique to estimate the properties of the weld in different directions to assess the mismatch properties more accurately, and avoid any unconservative estimates of the strength mismatch.

Recommendations and opportunities for future research

Through this work the instrumented indentation technique was used to characterize the mechanical properties for different engineering alloys. The main focus was on representative X80 pipeline steel. A new approach using a nearly flat tip indenter was developed in order to estimate the yield strength value for engineering alloys based on cavity expansion theory and slip line approach. However, due to time limitations the author could not investigate materials that show discontinues yielding behaviour (upper and lower yield point). Also, in the literature the behaviour of such material was not investigated under compression testing. Therefore, it is recommended in future studies to investigate this point and study the effect of Luder's bands on the yield strength obtained by the indentation method that was developed in this study.

In this study the inverse approach along with FE modelling was also developed and validated for line pipe steel and aluminium alloys in order to get the full stress-strain response. During this study Efficient Global Optimization (EGO) technique was used.

In the future it is recommended to use different optimization approaches such as genetic algorithms, unconstrained nonlinear minimization, and nonlinear curve fitting algorithms in order to evaluate them in terms of running time and result accuracy. In addition, the choice of the hardening model was possible owing to the forward analysis and availability of stress - strain data. However, a need remains for a technique to identify an appropriate hardening model given only by the indentation curve. Therefore, it is worthwhile to find a way to identify the hardening behaviour when the stress strain data are not available. Moreover, apply the suggested inverse approach for welded structure to obtain stress-strain curve for narrow zones, such as CGHAZ, FGHAZ, and reheated WM.

The relationship between grain size and yield strength (Hall-Petch relationship) is well known as a main strengthening mechanism. The size of the indenter that was used in this study was 100 μm. This is due to the limitation of the load capacity in the indentation system that was used in this study. However, in some cases the grain size of the materials could be larger than 100 μm, which may limit the number of grains in contact with the semi-flat indenter and affect the obtained yield strength values. Even so, this is not the case for line pipe steels or its welds since those line pipe steels have a fine grain size. However, it is recommended to study the effect of indenter size and grain size on the yield strength obtained by using this method especially when large grain size material present.

The nearly flat tip indentation system showed repeatable and accurate results. However, the system has only been demonstrated in the lab. In the future it is recommended to build a portable system that can apply different loads and measure yield strength for pipeline applications in the field. This will improve the integrity and increase the reliability of the measurements during the welding process or during repair events.

Finally, during the assessment of strength mismatch properties for pipeline welds, anisotropic behaviour was discovered. Whereas the focus of this study was not to investigate weld anisotropy, it is recommended to do so in the future studies to evaluate the effect of anisotropy on the joint behaviour when strain based design criteria is considered. In addition, it is recommended that a future study explore possible reasons that lead to the anisotropic behaviour such as residual stresses and material texture.

List of Publications

1- A. R. H. Midawi, C. H. M. Simha , A. P. Gerlich Yield Strength Mis-match Assessment using Indentation Technique for X80 Pipeline Steel Welds . Submitted manuscript to Science and Technology of Welding and Joining April 2018.

2- A. R. H. Midawi, C. H. M. Simha , N. Huda , A. P. Gerlich Characterization of Anisotropic Properties of API-X80 Line Pipe Welds by means of Instrumented Indentation Techniques . Submitted manuscript to Journal of Materials Science & Engineering A August (2018).

3- A. R. H. Midawi, C. H. M. Simha , M. A. Gesing , A. P. Gerlich, Elastic-plastic Property Evaluation Using A Nearly Flat Instrumented Indenter, published at International Journal of Solids and Structures (IJSS), 2016.http://dx.doi.org/10.1016/j.ijsolstr.2016.09.036.

4- A.R.H. Midawi, C.H.M. Simha and A.P. Gerlich, Novel techniques for estimating yield strength from loads measured using nearly-flat instrumented indenters, Materials Science & Engineering A (2016), http://dx.doi.org/10.1016/j.msea.2016.08.056.

5- Abdelbaset Midawi, Y. Kisaka, E.B.F. Santos, A.P. Gerlich, Characterization of Local Mechanical Properties of X80 Pipeline Girth Welds Using Advanced Techniques ,

IPC2016-64238, September 26-30th, Calgary, AB, Canada. http://dx.doi.org/10.1115/IPC2016-64238.

6- Abdelbaset Midawi, C. H. M. Simha, A. P. Gerlich, and N. Huda, Simulation of Instrumented Indentation Process Using Nearly Flat and Spherical Indenters, Canadian Materials Science Conference, CMSC-2016, June 7-10th, McMaster University, Hamilton, ON, Canada, (Conference Presentation).

References

[1] B. M. Adams, L. E. Bauman, W. J. Bohnhoff, K. R. Dalbey, J. P. Eddy, M. S. Ebeida, M. S. Eldred, P. D. Hough, K. T. Hu, J. D. Jakeman, L. P. Swiler, J. A. Stephens, D. M. Vigil, and T. M. Wildey. *Dakota , A Multilevel Parallel Object-Oriented Framework for Design Optimization , Parameter Estimation , Uncertainty Quantification , and Sensitivity Analysis : Version 6 . 0 User ' s Manual*. Number May. 2014.

[2] J. Alcalá, .E. Giannakopoulos, and S. Suresh. Continuous measurements of load-penetration curves with spherical microindenters and the estimation of mechanical properties. *Journal of Materials Research*, 13(05):1390–1400, 1998.

[3] R. Marcinkowski M. J. Szirmae A. and Fisher. Effect of 500 C Aging on Deformation Behavior of Iron -Charomium Alloy. In *Transactions of the Metallurgical Society of AIME*, pages 230(4), 676. TMS, 1964.

[4] R. V. and Prakash and S. S. Chow. An evaluation of stress-strain property prediction by Automated Ball Indentation (ABI) testing. *Journal of Testing and Evaluation*, 35(3):221–232, 2007.

[5] J. Antunes, J. Fernandes, L. Menezes, and B. Chaparro. A new approach for reverse analyses in depth-sensing indentation using numerical simulation. *Acta Materialia*, 55(1):69–81, 2007.

[6] Canadian Standards Association. *National standard of Canada CAN/CSA-Z662-15 Oil and gas pipeline systems*, volume 15. CSA-group, 2015.

[7] ASTM. E3-11 Standard Guide for Preparation of Metallographic Specimens 1. *ASTM Copyright.*, i:1–12, 2011.

[8] ASTM. ASTM E112-13: Standard test methods for determining average grain size. *ASTM International*, pages 1–28, 2013.

[9] G. Avramovic-Cingara, C. A R Saleh, M. K. Jain, and D. S. Wilkinson. Void nucleation and growth in dual-phase steel 600 during uniaxial tensile testing. *Metallurgical and Materials Transactions A: Physical Metallurgy and Materials Science*, 40(13):3117–3127, 2009.

[10] J. Dorricott B. Dengqi, M. Ambrose Cooke, J. Asante. Process for making high strength micro-alloy steel, 2004.

[11] S. S. Babu. The mechanism of acicular ferrite in weld deposits. *Current Opinion in Solid State and Materials Science*, 8(3-4):267–278, 2004.

[12] S. S. Babu and H Bhadeshia. Transition from bainite to acicular ferrite in reheated Fe-CrC weld deposits. *Materials Science and Technology*, 6(October):1005–1020, 1990.

[13] T.N. Baker. Microalloyed Steels. *Ironmaking and Steelmaking*, 43(4):264–307, 2016.

[14] A. Bakkalolu. Effect of processing parameters on the microstructure and properties of an Nb microalloyed steel. *Materials Letters*, 56(3):200–209, 2002.

[15] J. Bally. *Determination of local strength properties of heterogeneous welds*. PhD thesis, University of Gent, 2015.

[16] M. Beghini. Evaluation of the stress strain curve of metallic materials by spherical indentation. *International Journal of Solids and Structures*, 43:2441–2459, 2006.

[17] B. Beidokhti, A. H. Kokabi, and A. Dolati. A comprehensive study on the microstructure of high strength low alloy pipeline welds. *Journal of Alloys and Compounds*, 597:142–147, 2014.

[18] B. Beidokhti, A.H. Koukabi, and A. Dolati. Influences of titanium and manganese on high strength low alloy SAW weld metal properties. *Materials Characterization*, 60(3):225–233, 2009.

[19] H. K .D .H. Bhadeshia and L. E. Svensson. Modelling the Evolution of Microstructure in Steel Weld Metal. *Mathematical Modelling of Weld Phenomena*, 1:109–182, 1993.

[20] A. K. Bhattacharya and W. D. Nix. Finite element simulation of indentation experiments. *International Journal of Solids and Structures*, 24(9):881–891, 1988.

[21] P. Brammer, X. Hernot, G. Mauvoisin, O. Bartier, and S. S. Sablin. A method to take account of the geometrical imperfections of quasi-spherical indenters. *Materials and Design*, 49:406–413, 2013.

[22] R. L. Brockenbrough and F. S. Merritt. *Structural Steel Designer's Handbook*. McGraw-Hill, fourth edi edition, 2006.

[23] J. A. Cahoon. An Improved Equation Relating Hardness to Ultimate Strength. *Metallurgical Transactions*, 3(November 1972):3040, 1972.

[24] J. R. Cahoon, W. H. Broughton, and A. R. Kutzak. The determination of yield strength from hardness measurements. *Metallurgical Transactions*, 2(7):1979–1983, 1971.

[25] Canadian Association of Petroleum Producers. Maps for excited and proposed pipeline in Canada and US., 2015.

[26] Y. Cao, X. Qian, and N. Huber. Spherical indentation into elastoplastic materials: Indentation-response based definitions of the representative strain. *Materials Science and Engineering A*, 454-455:1–13, 2007.

[27] X. Chen, N. Ogasawara, M. Zhao, and N. Chiba. On the uniqueness of measuring elastoplastic properties from indentation: The indistinguishable mystical materials. *Journal of the Mechanics and Physics of Solids*, 55(8):1618–1660, 2007.

[28] C. M. Cheng, Y. T. and Cheng. Can stressstrain relationships be obtained from indentation curves using conical and pyramidal indenters? *Journal of Materials Research*, 14(9):3493–3496, 1999.

[29] N. Chollacoop, M. Dao, and S. Suresh. Depth-sensing instrumented indentation with dual sharp indenters. *Acta Materialia*, 51(13):3713–3729, 2003.

[30] K. H. Chung, W. Lee, J. H. Kim, C. Kim, S. Park, D. Kwon, and K. Chung. Characterization of mechanical properties by indentation tests and FE analysis - validation by application to a weld zone of DP590 steel. *International Journal of Solids and Structures*, 46(2):344–363, 2009.

[31] J. D. Clayton. Spherical Indentation in Elastoplastic Materials : Modeling and Simulation. Technical Report May, US. Army Research Labortory, 2005.

[32] J. Collin, G. Mauvoisin, and P. Pilvin. Materials characterization by instrumented indentation using two different approaches. *Materials & Design*, 31(1):636–640, 2010.

[33] European Commission, J. Crahay, J. Edmundson, and A. Giannetti. Effect of alloying elements on HAZ microstructure and toughness. Technical Report 7210, European Commission, Lexembourg, 1996.

[34] Committee of Welding Metallurgy of Japan Welding Society. Classification of microstructure in low carbon-low alloy steel weld metal amd terminology. *IIW Doc.*, IX(83):1–22, 1983.

[35] Correlated Solutions. Vic-3D 2010 Reference Manual. page 107. 2010.

[36] M. Dao, N. Chollacoop, K. J. Van Vliet, T . Venkatesh, and S. Suresh. Computational modeling of the forward and reverse problems. *in instrumented sharp indentation, Acta Mater.*, 49:3899–3918, 2001.

[37] Dassault Systèmes Simulia. *Abaqus 6.14 Theory Guide*. Dassault Systemes Simulia, 6.14 edition, 2014.

[38] J. R. Davis. Alloying: Understand the basics (High Strength Low Alloy Steels). In J. R. Davis, editor, *ASM International*, volume 1, chapter 1, pages 195–202. ASM International, 1 edition, 2001.

[39] Det Norske Veritas. *Submarine Pipeline Systems*. Number F101. DNV, 2010.

[40] J. Devore. *Probability and Statistics for Engineering and the Sciences*. Cengagae Learning, 8th editio edition, 2012.

[41] C.F. Duren. Prediction of the hardness in the HAZ of HSLA Steels by Means of the Carbon Equivalent. In *Hardenibility of Steels-Select Conference*, pages 51–62, 1990.

[42] K. E. Easterling. *Introduction to the Physical Metallurgy of Welding*. Butterworth-Heinemann, London, 2nd editio edition, 1992.

[43] E. El-Kashif and T. Koseki. Effect of niobium on HAZ toughness of HSLA steels. *Journal of Engineering and Applied Science*, 56(6):679–699, 2009.

[44] D. P. Fairchild, N. V. Bangaru, J. Y. Koo, P. L. Harrison, and A. Ozekcin. A Study Concerning Intercritical HAZ Microstructure and Toughness in HSLA Steels. *Welding Journal*, 70(12):321s–330s, 1991.

[45] M. Fattahi, N. Nabhani, M. Hosseini, N. Arabian, and E. Rahimi. Effect of Ti-containing inclusions on the nucleation of acicular ferrite and mechanical properties of multipass weld metals. *Micron*, 45:107–114, 2013.

[46] L. Fletcher, Z. Zhu, M. Marimuthu, L. Zheng, M. Bai, H. Li, and F. Barbaro. Effect of Ti and N concentrations on microstructure and mechanical properties of microal-

loyed high strength line pipe steel welds. In *Welding of high strength pipeline Steels, International Seminar.*, pages 1–13. University of Wollongong Research Online, 2011.

[47] R. S. Funderburk. A look at heat input. *Welding Innovation*, XVI(1), 1999.

[48] R. S. Funderburk. Selecting Filler Metals : Matching Strength Criteria. *Welding Innovation*, XVI(2):2–4, 1999.

[49] G. R. Speich and H. Warlimont. No Title. *J. Iron Steel Inst.*, 206(pp. 385-92.), 1968.

[50] A. E. Giannakopoulos and S. Suresh. Determination of elastoplastic properties by instrumented sharp indentation. *Scripta Materialia*, 40(10):1191–1198, 1999.

[51] T. Gladman. *The Physical Metallurgy of Microalloyed Steels*. The Institute of Materials, second edi edition, 1997.

[52] A. G. Glover, D. J. Horsley, and D. V. Dorling. *High-strength steel becomes standard on alberta gas system*, volume 97. Petroleum Pub. Co, 1910.

[53] G. R. Goodall. *Welding High Strength Modern Line Pipe Steel by*. PhD thesis, McGill University, 2011.

[54] M. K. Graf, H. Hillenbrand, and K. A. Niederhoff. High-strength large - diameter pipe for long-distance high pressure gas pipelines. In *ISOPE*, page 9, 2003.

[55] F. M. Haggag. Haggag-1989 Pataent US4852397.

[56] F. M. Haggag. In-Situ Measurements of Mechanical-Properties Using Novel Automated Ball Indentation System. *Small Specimen Test Techniques Applied to Nuclear*

Receptor Vessel Thermal Annealing and Plant Life Extension, 1204(Jan 1993):27–44, 1993.

[57] F. M. Haggag. In-Situ Measurements of Mechanical-Properties Using Novel Automated Ball Indentation System1. *Small Specimen Test Techniques Applied to Nuclear Receptor Vessel Thermal Annealing and Plant Life Extension*, 1204:27–44, 1993.

[58] F. M. Haggag. In-Situ ABI Testing to Determine Yield Strength, Pipe Grade, and Fracture Toughness of In-Service Oil and Gas Pipelines. *Russian Oil and Gas Technology Magazine*, (2011):22–29, 2015.

[59] F. Y M Haggag and Glenn E. Lucas. Determination of luders strains and flow properties in steels from hardness/microhardness tests. *Metallurgical Transactions A*, 14(August):1607–1613, 1983.

[60] P. L. Harrison and R. A. Farrar. Influence of oxygen-rich inclusions on the $\gamma\alpha$ phase transformation in high-strength low-alloy (HSLA) steel weld metals. *Journal of Materials Science*, 16(8):2218–2226, 1981.

[61] J. A. Hawk, R. E. Franck, and H. G. F. Wilsdorf. Yield Stress as Determined from Hardness Measurements for Mechanically Alloyed Aluminum Base Alloys. *Metallurgical Transactions A*, 19A(September):2363–2366, 1988.

[62] K. He and D. V. Edmonds. Formation of acicular ferrite and influence of vanadium alloying. *Materials Science and Technology*, 18(3):289–296, 2002.

[63] E. G. Herbert, G. M. Pharr, W. C. Oliver, B. N. Lucas, and J. L. Hay. On the mea-

surement of stress-strain curves by spherical indentation. *Thin Solid Films*, 398:331–335, 2001.

[64] X. Hernot and O. Bartier. An expanding cavity model incorporating pile-up and sink-in effects. *Journal of Materials Research*, 27(1):132–140, 2011.

[65] S. Hertelé. *Coupled Experimental-Numerical Framework for the Assessment of Strain Capacity of Flawed Girth Welds in Pipelines*. PhD thesis, University of Gent, 2012.

[66] O. Hilgert and S. Höhler. Anisotropic hfi welded steel pipes for strain based design. pages 1–9, 2016.

[67] R. Hill. *The mathematical theory of plasticity*, volume 11. Oxford university press, 1998.

[68] H. G. Hillenbrand, M. Graf, and C. Kalwa. Development and production of high strength pipeline steels. *International Symposium Niobium 2001*, 2001.

[69] H. G. Hillenbrand, C. J. Heckmann, and K. A. Niederhoff. X80 line pipe for large-diameter high strength pipelines. *APIA 2002 Annual Conference X80 Pipeline Workshop*, 100:1–15, 2002.

[70] S. Hohler, H. Karbasian, A. Gering, C. Kalwa, and B. Ouaissa. Strain capacity of large diameter pipes: Full scale investigation with influence of girth weld, strip end weld and ageing effects. *Proceedings of the Biennial International Pipeline Conference, IPC*, 2:Pipeline Division –, 2016.

[71] Z. Hu, K. Lynne, and F. Delfanian. Characterization of materials' elasticity and yield strength through micro-/nano-indentation testing with a cylindrical flat-tip indenter. *Journal of Materials Research*, 30(04):578–591, 2015.

[72] F. Huang, J. Liu, Z. J. Deng, J. H. Cheng, Z. H. Lu, and X. G. Li. Effect of microstructure and inclusions on hydrogen induced cracking susceptibility and hydrogen trapping efficiency of X120 pipeline steel. *Materials Science and Engineering A*, 527(26):6997–7001, 2010.

[73] I. N. Katsina. *Effect of welding thermal cycles on the heat effected zone microstreucture and toughness of multi-pass welded pipeline steel.* PhD thesis, 2012.

[74] American Petroleum Institute. API 1104. standard for welding pipelings and related facilities. In *Api*, volume 552, page 79. 2005.

[75] M. Ito, J. and Nakanishi. Study on Charpy impact properties of weld metal with submerged-arc welding. *Sumitomo Search*, 15:42–62, 1976.

[76] K. Ito, Y. and Bessyo. Weldability Formula of High Strength Steels: Related to Heat-affected Zone Cracking. In *IIW - (Arc Welding)*. IIW, 1968.

[77] J. Jang, Y. Choi, J. S. Lee, Y. H. Lee, D. Kwon, Mi. Gao, and R. Kania. Application of instrumented indentation technique for enhanced fitness-for-service assessment of pipeline crack. *International Journal of Fracture*, 131(1):15–33, 2005.

[78] C.L. Jenney and A. O'Brien. *Welding handbook*, volume 1. AWS, 1991.

[79] D. R. Jones, M. Schonlau, and J. William. Efficient Global Optimization of Expensive Black-Box Functions. *Journal of Global Optimization*, 13:455–492, 1998.

[80] M. S. Joo, D.W. Suh, and H. K. D. H. Bhadeshia. Mechanical Anisotropy in Steels for Pipelines. *ISIJ International*, 53(8):1305–1314, 2013.

[81] W. Tyson J.T.Bowker, J.A. Gianetto, G. Shen and D. Horsley. Ipc2006-10400 Strain-Based Designed Pipelines. In *IPC*, volume 6, pages 1–12, Calgary, 2006. ASME.

[82] K. Junhua, Z. Lin, G. Bin, L. Pinghe, W. Aihua, and X. Changsheng. Influence of Mo content on microstructure and mechanical properties of high strength pipeline steel. *Materials & Design*, 25(8):723–728, 2004.

[83] J. Kadkhodapour, A. Butz, and S. Ziaei Rad. Mechanisms of void formation during tensile testing in a commercial, dual-phase steel. *Acta Materialia*, 59(7):2575–2588, 2011.

[84] J. Kang, Y. Ososkov, J. D. Embury, and D. S. Wilkinson. Digital image correlation studies for microscopic strain distribution and damage in dual phase steels. *Scripta Materialia*, 56(11):999–1002, 2007.

[85] M. Kashfuddoja, R. G. R. Prasath, and M. Ramji. Study on experimental characterization of carbon fiber reinforced polymer panel using digital image correlation: A sensitivity analysis. *Optics and Lasers in Engineering*, 62:17–30, 2014.

[86] S. H. Kim, M. K. Baik, and D. Kwon. Determination of Precise Indentation Flow Properties of Metallic Materials Through Analyzing Contact Characteristics Beneath Indenter. *Journal of Engineering Materials and Technology*, 127(3):265, 2005.

[87] T. Koseki and G. Thewlis. Overview Inclusion assisted microstructure control in CMn and low alloy steel welds. *Materials Science and Technology*, 21(8):867–879, 2005.

[88] S. Lambot, E. C. Slob, I. D. Van Bosch, B. Stockbroeckx, and M. Vanclooster. *Modeling of ground-penetrating radar for accurate characterization of subsurface electric properties*. Thesis, Cranfield University, 2004.

[89] L. Y. Lan, C. L. Qiu, D. W. Zhao, X. H. Gao, and L. X. Du. Effect of single pass welding heat input on microstructure and hardness of submerged arc welded high strength low carbon bainitic steel. *Science and Technology of Welding and Joining*, 17(7):564–570, 2012.

[90] M. Q. Le. Material characterization by instrumented spherical indentation. *Mechanics of Materials*, 46:42–56, 2012.

[91] H. Lee, J. Haeng Lee, and G. M. Pharr. A numerical approach to spherical indentation techniques for material property evaluation. *Journal of the Mechanics and Physics of Solids*, 53(9):2037–2069, 2005.

[92] J. H. Lee, T. Kim, and H. Lee. A study on robust indentation techniques to evaluate elastic-plastic properties of metals. *International Journal of Solids and Structures*, 47(5):647–664, 2010.

[93] P. Leroux. An Indentation Test That Measures Yield Strength. *Advanced Materials and Processes*, 169-10(October):34–35, 2011.

[94] J. Li, F. Li, X. Ma, Q. Wang, J. Dong, and Z. Yuan. A strain-dependent ductile damage model and its application in the derivation of fracture toughness by micro-indentation. *Materials and Design*, 67:623–630, 2015.

[95] C. Liu and S. D. Bhole. Challenges and developments in pipeline weldability and mechanical properties. *Science and Technology of Welding and Joining*, 18(2):169–181, 2013.

[96] Y. Liu, Y. Li, S. Li, Z. You, and Z. Yin. Microstructure and Mechanical Properties of Girth Weld HAZ in X80 With High Deformability For Strain Based Design Applications. In *Procedding of the 2016 11th International Pipeline Conference-IPC2016*, pages 1–10, Calgary, 2016. ASME.

[97] S. Liu, J.E. and Indacochea. Properties and Selection Irons , Steels , and High Performance Alloys :Fabrication Characteristics of Carbon and Low-Alloy Steels. In *ASM handbook*, volume 1, pages 924–936. ASM, 10th editi edition, 2005.

[98] W. D. Lockwood, B. Tomaz, and A. P. Reynolds. Mechanical response of friction stir welded AA2024 : experiment and modeling. 323:348–353, 2002.

[99] J. L. Loubet, J. M. Georges, O. Marchesini, and G. Meille. Vickers indentation curves of magnesium oxide (MgO). *Journal of tribology*, 106(1):43–48, dec 1984.

[100] J. Lu. *Quantitative Microstructural Characterization of Microalloyed Steels*. Phd thesis, University of Alberta, 2009.

[101] J. Lu, O. Omotoso, J. B. Wiskel, D. G. Ivey, and H. Henein. Strengthening Mecha-

nisms and Their Relative Contributions to the Yield Strength of Microalloyed Steels. *Metallurgical and Materials Transactions A*, 43(9):3043–3061, 2012.

[102] Y. C. Lu, Siva N .V. R. K. Kurapati, and F. Yang. Finite element analysis of cylindrical indentation for determining plastic properties of materials in small volumes. *Journal of Physics D: Applied Physics*, 41(11):115415, dec 2008.

[103] A. R. H. Midawi, E. B. F. Santos, N. Huda, A. K. Sinha, R. Lazor, and A. P. Gerlich. Microstructures and mechanical properties in two X80 weld metals produced using similar heat input. *Journal of Materials Processing Tech.*, 226:272–279, 2015.

[104] W. Mohr. Strain-based design of pipelines. Technical Report 45892, EWI, 2003.

[105] H. Mohrbacher. Principal effects of Mo in HSLA steels and cross effects with microalloying elements. *International Seminar in Applications of Mo in Steels*, pages 1–18, 2010.

[106] C. Moussa, X. Hernot, O. Bartier, G. Delattre, and G. Mauvoisin. Evaluation of the tensile properties of a material through spherical indentation: Definition of an average representative strain and a confidence domain. *Journal of Materials Science*, 49(2):592–603, 2014.

[107] A. Nayebi, R. El Abdi, O. Bartier, and G. Mauvoisin. New procedure to determine steel mechanical parameters from the spherical indentation technique. *Mechanics of Materials*, 34(4):243–254, 2002.

[108] J. Ni, Z. Li, J. Huang, and Y. Wu. Strengthening behavior analysis of weld metal of

laser hybrid welding for microalloyed steel. *Materials and Design*, 31(10):4876–4880, 2010.

[109] W. L. Oberkampf and M. F. Barone. Measures of agreement between computation and experiment: Validation metrics. *Journal of Computational Physics*, 217(1):5–36, 2006.

[110] M. Okatsu, K. Oi, K. Ihara, and T. Hoshino. Proceedings of OMAE04 23rd International Conference on Offshore Mechanics and Arctic Engineering. In *International Conference on Offshore Mechanics and Arctic Engineering*, pages 1–6, Vancouver, British Columbia, Canada, 2004.

[111] M. Okatsu, N. Shikanai, and J. Kondo. Development of a High-Deformability Linepipe with Resistance to Strain-aged Hardening by HOP (Heat-treatment On-line Process). Technical Report 12, JFE, 2008.

[112] M. C. Oliveira, J. L. Alves, B. M. Chaparro, and L. F. Menezes. Study on the influence of the work hardening models constitutive parameters identification in the springback prediction. *AIP Conference Proceedings*, 778 A:253–258, 2005.

[113] W. C. Oliver and G. M. . Pharr. An improved technique for determining hardness and elastic modulus using load and displacement sensing indentation experiments. *Journal of Materials Research*, 7(6):1564–1583, 1992.

[114] W. C. Oliver and G. M. Pharr. Measurement of hardness and elastic modulus by instrumented indentation Advances in understanding and refinements to methodology. *Materials Research Society*, 19(1):3–20, 2004.

[115] K. P. Anaraki. *Microstructure and Property Examination o f the Weld HAZ in Grade 100 Microalloyed Steel*. PhD thesis, University of Alberta, 2005.

[116] R. Pamnani, V. Karthik, T. Jayakumar, M. Vasudevan, and T. Sakthivel. Evaluation of mechanical properties across micro alloyed HSLA steel weld joints using Automated Ball Indentation. *Materials Science and Engineering A*, 651:214–223, 2016.

[117] J. T. Pepin. *Effects of Submerged Arc Weld (SAW) Parameters on Bead Geometry and Notch-Toughness for X70 and X80 Linepipe Steels*. Master of science thesis, University of Alberta, 1977.

[118] J. K. Phadikar, T. A. Bogetti, and A. M. Karlsson. On the uniqueness and sensitivity of indentation testing of isotropic materials. *International Journal of Solids and Structures*, 50(20-21):3242–3253, 2013.

[119] J. Billingham J.V. Sharp J. Superrier P.J.Kilgallon. Review of the performance of high Strength Steels used offsore. Technical report, Cranfield University and Health and Safety Executive, 2003.

[120] N.N. Potapov. Oxygen effect on low alloy steel weld metal properties. *Welding Research Supplement*, 13:367–370, 1993.

[121] J. C. Price. Welding needs specified for X-80 offshore line pipe. *Oil and Gas Journal*, 91(51), 1993.

[122] M. A. Quintana. Development of Optimized Welding Solutions for X100 Line Pipe

Steel Summary Report 278-S-01. Technical Report L5, Pipeline Research Council International Catalog (PRCI), Houston-Taxes, 2011.

[123] S. Kumar. J. Rachit Khanna. High Strength Low Alloy Steels - Indian Scenario.

[124] S. Radmard, , and M. Berg. Determining the Yield Strength of In-Service Pipe Using Hardness Testing. In *8th International Pipeline Conference*, pages 271–280. American Society of Mechanical Engineers, 2010.

[125] M. H. Ray and M. Mongiardini. Quantitative Methods for Assessing Similarity between Computational Results and Full-Scale Crash Tests. In *91th Annual Meeting of the Transportation Research Board*, number 12, page 18, 2012.

[126] P. Reynolds and F. Duvall. Digital image correlation for determination of weld and base metal constitutive behavior. *October*, 78(10):355–360, 1999.

[127] B. Riccardi and R. Montanari. Indentation of metals by a flat-ended cylindrical punch. *Materials Science and Engineering A*, 381(1-2):281–291, 2004.

[128] D .B. Rosado, W. De. Waele, and S. Vanderschueren, D., Hertele. Latest developments in mechanical properties and metallurgycal of high strenght line pipes. *Sustainable Construction and Design*, 4(1):1–10, 2013.

[129] A. M. Sage. Physical metallurgy of high strength, low alloy line pipe and pipe fitting steels. *Metals Technology*, 10(1):224–233, 1983.

[130] K. M. Saranath, A. Sharma, and M. Ramji. Zone wise local characterization of

welds using digital image correlation technique. *Optics and Lasers in Engineering*, 63:30–42, 2014.

[131] H. Sarin, M. Kokkolaras, G. Hulbert, P. Papalambros, S. Barbat, and R. J. Yang. Comparing time histories for validation of simulation models: Error measures and metrics. *Journal of Dynamic Systems, Measurement, and Control*, 132(6):61401, 2010.

[132] K. P. Shah. The Hand Book on Mechanical Maintenance.

[133] R. Shield. On the plastic flow of metals under conditions of axial symmetry. In *Proceedings of the Royal Society of London A: Mathematical, Physical and Engineering Sciences*, volume 233, pages 267–287. The Royal Society, 1955.

[134] K. Sindo. *Welding Metallurgy*, volume 1. John Wiley & Sons Inc., New York, second edi edition, 2003.

[135] Transportation Officials Standard, An American, and National Standard. *Standard Test Methods for Tension Testing of Metallic Materials E8.* Number 04. ASTM International, 2008.

[136] T. Stocks, T. and London. Validation and Standardisation of Novel Local Mechanical Characterisation Techniques for Metals Validation and Standardisation of Novel Local Mechanical Characterisation Techniques for Metals. Technical Report 0, TWI, 2014.

[137] H. K. Sung, S. S. Sohn, S. Y. Shin, K.S. Oh, and S. Lee. Effects of Oxides on Tensile and Charpy Impact Properties and Fracture Toughness in Heat Affected Zones of

Oxide-Containing API X80 Linepipe Steels. *Metallurgical and Materials Transactions A*, 45(7):3036–3050, 2014.

[138] E. Surian, J. Trotti, A. Cassanelli, and L. De Vedia. Influence of chromium on the mechanical properties and microstructure of weld metal from a high strength SMA electrode. *Welding Journal*, 73(3):45–s–53–s, 1994.

[139] M. Sutton, J. Orteu, and H. Schreier. *Image correlation for shape, motion and deformation measurements*. Springer US, 2009.

[140] D. Tabor. *The Hardness of Metals*. OUP Oxford, 2000.

[141] S. Talas. The assessment of carbon equivalent formulas in predicting the properties of steel weld metals. *Materials & Design*, 31(5):2649–2653, 2010.

[142] B. Taljat, T. Zachari, and F. Kosel. New analytical procedure to determine stress strain curve from spherical indentation data. International Journal of Solids and Structures. *Int. J. Solids Structures*, 35(33):4411–4426, 1998.

[143] Y. Terada, A. Kiyose, N. Doi, H. Morimoto, A. Kojima, T. Nakashima, T. Hara, and M. Sugiyama. High-strength Linepipes with Excellent HAZ Toughness. Technical Report 90, 2004.

[144] S. Terashima and H. K. D. H. Bhadeshia. Changes in toughness at low oxygen concentrations in steel weld metals. *Science and Technology of Welding and Joining*, 11(5):509–516, 2006.

[145] G. Thewlis. Classification and quantification of microstructures in steels. *Materials Science and Technology*, 20(2):143–160, 2004.

[146] U.S. Energy Information Administration. *International Energy Outlook 2016*, volume 484. Energy Information Administration, 2016.

[147] M. R. Vanlandingham. Review of Instrumented Indentation. *Journal Of Research Of The National Institute Of Standards And Technology*, 108(4):249–265, 2003.

[148] W. Zielinski, H. Huang, and W.W. Gerberich. Microscopy and microindentation mechanics of single crystal Fe3 wt. % Si: Part I. Atomic force microscopy of a small indentation. *Journal of Materials Research*, 8(6):1300–1310, 1993.

[149] B. Whang, W. E. Gilbert, and S. Zilliacus. Two visually meaningful correlation measures for comparing calculated and measured response histories. *Shock and Vibration*, 1(4):303–316, 1994.

[150] P. E. Wierenga and A. J. J. Franken. Ultra-microindentation apparatus for the mechanical characterization of thin films. *Journal of Applied Physics*, 55(12):4244, dec 1984.

[151] J. Yan, M. A. Sutton, A. P. Reynolds, S. Adeeb, and D. Horsley. Characterization of Heterogeneous Response of Pipeline Steel Weld using Digital Image Correlation. (October 2015), 2006.

[152] Z. Yao. *Development of an Indentation Method for Material Surface Mechanical Properties Measurement*. PhD thesis, West Virginia, 2005.

[153] D. Yapp and S. A. Blackman. Recent developments in high productivity pipeline welding. *Journal of the Brazilian Society of Mechanical Sciences and Engineering*, 26(1):89–97, 2004.

[154] G.M. Pharr Y.J. Parka,. Nanoindentation with spherical indenters: finite element studies of deformation in the elasticplastic transition regime. *Thin Solid Films*, 446(1):246–250, 2004.

[155] A. Yonezu, H. Akimoto, S. Fujisawa, and Xi Chen. Spherical indentation method for measuring local mechanical properties of welded stainless steel at high temperature. *Materials and Design*, 52:812–820, 2013.

[156] W. Yu and J. P. Blanchard. An elastic-plastic indentation model and its solutions. *Journal of Materials Research*, 11(09):2358–2367, 1996.

[157] N. Yurioka. Carbon equivalents for hardenability and cold cracking susceptibility of steels. Technical report, The Welding Institute, 1990.

[158] S. M. Zakaria. *Study on the Microstructure and Mechanical Properties of Submerged Arc Welded X80 Steel*. PhD thesis, University of Alberta, 2012.

[159] Y. Q. ZHANG, H. Q. ZHANG, Ji. f. LI, and W. M. LIU. Effect of Heat Input on Microstructure and Toughness of Coarse Grain Heat Affected Zone in Nb Microalloyed HSLA Steels. *Journal of Iron and Steel Research International*, 16(5):73–80, 2009.

[160] Z. Zhang and R. A. Farrar. Influence of Mn and Ni on the microstructure and toughness of C-Mn-Ni weld metals. *Weld. J.*, 76(5):183–196, 1997.

[161] Z. L. Zhang, M. Hauge, C. Thaulow, and J. Odegard. A notched cross weld tensile testing method for determining true stress-strain curves for weldments. *Engineering Fracture Mechanics*, 69(3):353–366, 2002.